

# Investigation of Primary Process Parameters for Laser Powder Bed Fusion of High Temperature Alloys through Physical and Virtual Experimentation.

---

A

Thesis

Presented to

the faculty of the School of Engineering and Applied Science

University of Virginia

---

in partial fulfillment

of the requirements for the degree

Master of Science

by

Adrian Baisas Dalagan

August 2022

# APPROVAL SHEET

This  
Thesis  
is submitted in partial fulfillment of the requirements  
for the degree of  
Master of Science

Author: Adrian Baisas Dalagan

This Thesis has been read and approved by the examining committee:

Advisor: Dr. Richard Martukanitz

Advisor: Dr. Prasanna Balachandran

Committee Member: Dr. Tao Sun

Committee Member:

Committee Member:

Committee Member:

Committee Member:

Committee Member:

Accepted for the School of Engineering and Applied Science:



Jennifer L. West, School of Engineering and Applied Science

August 2022

# Abstract

Recent innovations in the aerospace and energy industries require materials capable of maintaining sufficient mechanical strength at high operating temperatures. A category of materials that possesses these capabilities are refractory metals. However, due to several factors, such as their very high strength at room temperature, they are difficult to shape through conventional metal removal manufacturing practices. Because of this, additive manufacturing methods, such as laser powder bed fusion are being explored for cost-effective fabrication of complex net-shape geometries from high temperature materials. In response to this demand, the impact of primary processing parameters for laser powder bed fusion for these materials were investigated using laboratory experiments, as well as physics-based modeling. These two approaches were believed to provide complimentary information and data that would enable the establishment and exploration of complex relationships not readily apparent through only physical experimentation. The two alloys examined in this study were a nickel-based alloy, IN718, and a niobium-based alloy, C103.

Physical experimentation was confined to the IN718 alloy due to unavailability of the refractory metal. The results of the laboratory experiments were examined utilizing statistical methods, such as analysis of variance and linear regression, to determine the influence of primary process parameters, such as laser power, scan speed, and powder size distribution, on critical melt pool geometries of melt pool width and depth. Virtual simulations were conducted with both materials using ANSYS Fluent to capture thermal and flow behaviors of the melt pool. The results from the physical experiments showed that the melt pool depth was more sensitive to the primary parameters comprising the energy density function, laser power and velocity, as well as mean powder size, compared to bead width. Virtual simulations also reflected this sensitivity with melt pool measurements. However, underlying phenomena like vaporization of material, recoil pressure, and creation of a free surface must be accounted for to accurately simulate bead width.

# Acknowledgement

I would like to give my deepest gratitude towards my advisor, Dr. Richard Martukanitz, for being an approachable and patient mentor who always believed in my abilities. I also extend my thanks towards the members of the committee; Dr. Prasanna Balachandran for volunteering to be my co-advisor as well as igniting my enthusiasm towards data informatics and Dr. Tao Sun for sparking my interest towards characterization of materials. Another faculty member of the University of Virginia that I wanted to acknowledge would be Dr. Bicheng Zhou and his post-doc Dr. Kang Wang for providing Thermo-Calc results for the thermophysical properties of C103.

My appreciation towards Kyle Snyder for being a great supervisor and giving me opportunities for hands-on experiences with additive manufacturing such as the operating a laser powder bed fusion machine.

I also want to thank the Commonwealth Center for Advanced Manufacturing (CCAM) for providing the samples and equipment used in this study as well as providing me an environment where I can mature as a professional.

For providing the size-distributed powder, I would like to give credit to Praxair Corporation.

I want to acknowledge my best friends; Annie and Lydia for being my confidants while all three of us go through our grueling post-bachelor studies and Roberto for being a great classmate and making my time in the University of Virginia a great one.

Finally, I dedicate this thesis to my parents, Marcelo, and Maria Teresa for their hard work and sacrifice to ensure that me and my sisters, Amanda, and Andrea, are able to access opportunities to live out our greatest potential.

# Table of Contents

<i>Abstract</i>	<b>1</b>
<i>Acknowledgement</i>	<b>2</b>
<i>Table of Contents</i>	<b>3</b>
<i>List of Figures</i>	<b>5</b>
<i>List of Tables</i>	<b>7</b>
<b>Chapter 1: Introduction to High Temperature Alloys and Additive Manufacturing</b>	<b>8</b>
<b>1.1 High Temperature (HT) Alloys</b>	<b>8</b>
1.1.1 General Properties and Application of HT Alloys	8
1.1.2 Challenges of Refractory Materials	9
<b>1.2 Additive Manufacturing</b>	<b>10</b>
1.2.1 Additive Manufacturing of High Temperature Alloys	11
1.2.2 Challenges in the Additive Manufacturing (AM) Process	15
<b>Chapter 2: Rationale and Objective of Current Study</b>	<b>17</b>
<b>2.1 Objectives of This Research</b>	<b>19</b>
<b>Chapter 3: Experiment Description and Methodology</b>	<b>20</b>
<b>3.1 Physical Experiments and Characterization</b>	<b>20</b>
3.1.1 Experimental Layout	20
3.1.2 Characterization	22
3.1.3 Data Processing	23
<b>3.2 Model Development</b>	<b>26</b>
3.2.1 Geometry and Mesh Construction	28
3.2.2 Model Configurations	31
Heat Source Shape and Positioning	31
Boundary Conditions	32
3.2.3 Representation of Material Behavior	35
Density	36
Specific Heat Capacity	37
Thermal Conductivity	38
3.2.4 Simulation Settings and Summary	41
<b>3.3 Database Creation of Properties for Niobium Alloy C103</b>	<b>43</b>
<b>Chapter 4: Results and Discussion</b>	<b>44</b>
<b>4.1 Data Processing of Experimental Data</b>	<b>44</b>
4.1.1 Initial Analyses	44
4.1.2 Correlation Analysis	47
4.1.3 Boxplots, Dot plots and Histograms	48
4.1.4 Regression Analyses	52
4.1.5 Discussion of the Data Analyses	57
<b>4.2 Simulation Results and Comparison with Experimental Data</b>	<b>61</b>
4.2.1 Temperature and Velocity Profiles	61
4.2.2 Melt Pool Geometry Measurements	65

4.2.3 Discussion on the Physics-based Model	67
<b>4.3 High Temperature Alloy Simulation</b>	<b>72</b>
4.3.1 Database Compilation Results	72
4.3.2 Simulation of C103 Based on Projected Thermophysical Data	78
4.3.3 Discussion on the Database and C103 Melt Pool Geometry	80
<b>Chapter 5: Conclusions</b>	<b>85</b>
<b>Bibliography</b>	<b>87</b>

# List of Figures

Figure 1: Yield Stress vs Temperature of IN718[5], Ti64 [3], Nb-based Alloys [7].-----9

Figure 2: Parts created from Nb or Nb-based alloys through additive manufacturing: a propulsion part (left) [10] and a superconductive component (right) [9].-----9

Figure 3: Schematic of a laser-based (left) and an electron beam-based (right) powder bed fusion (PBF) processes [2].-----10

Figure 4: A 3D model of a heat exchanger with gyroid geometries that can be made possible by AM [12].-----11

Figure 5: C103 Microstructures from Laser-PBF process in both the transverse (left) and longitudinal (right) orientations[4].-----14

Figure 6: C103 Microstructures from EB-PBF process in both the transverse (left) and longitudinal (right) orientations [4].--14

Figure 7 In-situ x-ray observation of a keyhole porosity formation [17].-----16

Figure 8 Delamination defect of an AM-printed part [18].-----16

Figure 9: Single-Track Weld(left) and Characterization of the Single-Track Cross-Section (right) [20].-----18

Figure 10: Physical phenomena in the AM process [21].-----18

Figure 11: Process maps of predicting: relative density (left) [8] and melt pool depth(right)[22].-----19

Figure 12:Arrangement of the melt pool tracks, and their line numbers as listed in Table 2.-----22

Figure 13: Characterization of the Melt Pool.-----23

Figure 14: Boxplot and its Components [23].-----24

Figure 15:A boxplot(left) and its corresponding dot plot(right) [25, 26].-----24

Figure 16: Example of a correlogram [28].-----25

Figure 17: Image of the total geometry (left) and the cross-sectional layout featuring the two layers and the designated refined region (right).-----29

Figure 18: Cross-sectional view of the mesh, with the size increasing in size with distance from the refined region.-----30

Figure 19: Volumetric energy distribution with the heat source model used (units are in  $W/m^3$ ).-----31

Figure 20: Application of boundary conditions with respect to the geometry.-----32

Figure 21: Pressure vs temperature model with pressure smoothing equation used by Cao and Yuan[33].-----34

Figure 22: Marangoni effect with negative and positive surface tension gradients [36].-----35

Figure 23: Compilation of density values in literature and linear regression lines listed in Table 5 [33, 37–40].-----36

Figure 24: Compilation of specific heat capacity literature values with the regression equations [38,39,41,43,44,46-48].----38

Figure 25: Flowchart for path-dependency of thermal conductivity-----40

Figure 26: Compilation of thermal conductivity literature and regression lines [37,39,46,47,50-52].-----40

Figure 27: Comparison of temperature profiles between adjusted (3500K) and default (5000K) temperature limits -----41

Figure 28: Verification of quasi-steady state condition for melt pool depth-----41

Figure 29: Verification of quasi-steady state condition for bead width-----43

Figure 30: Initial boxplot of melt pool depth and bead width showing the outliers.-----45

Figure 31: Initial histogram of melt pool depth and bead width responses.-----45

Figure 32: Correlation matrices between independent and dependent variables.-----47

Figure 33: Boxplot of melt pool depth across different powder size distribution.-----48

Figure 34: Dot plot of melt pool depth across different powder size distribution with outliers omitted.-----49

Figure 35: Boxplot arranged by energy density with corresponding line number designation.-----50

Figure 36: Boxplots of bead width arranged in terms of energy density including outliers.-----50

Figure 37: Dot plot of bead width arranged in terms of energy density including outliers-----51

Figure 38: Histograms of melt pool depth (left) and bead width (right) with outliers omitted.-----52

Figure 39: Adjusted R2 across powder size subsets.-----56

Figure 40: Bar graph for melt pool depth standard deviation for each line number.-----56

Figure 41: Bar graph for bead width standard deviation for each line number.-----57

Figure 42: Scattering of laser as it goes through the powder layer[29]-----58

Figure 43: Effect of Powder $D_{50}$ on melt pool depth, bead width and bead width standard deviation according to Spurek et al [56]	60
Figure 44: Distribution of powder particle size with recoater distance [57].	60
Figure 45: Initial thermal conductivity distribution between powder and substrate (longitudinal view).	61
Figure 46: Powder conductivity at 500 $\mu$ s with melt pool present.	61
Figure 47: Thermal conductivity at 9000 $\mu$ s after cooling to near room temperature.	61
Figure 48 Longitudinal temperature profile for parameters 285W and 960mm/s at 300 $\mu$ s (in Kelvin).	62
Figure 49: Cross section temperature profile for parameters 285W and 960mm/s at 300 $\mu$ s (in Kelvin).	63
Figure 50: Longitudinal view of velocity vectors at 1300 $\mu$ s (in m/s).	64
Figure 51: Cross-section view of velocity vectors at 1300 $\mu$ s (in m/s).	64
Figure 52: Melt pool depth vs surface energy density.	67
Figure 53: Bead width vs surface energy density.	67
Figure 54: Vapor pressure illustration [45].	68
Figure 55: Cross-sectional melt pool from Cao and Yuan [33] (left) and from Le et al[58](right).	69
Figure 56: Velocity profile of Cao and Yuan [33].	70
Figure 57: Effects of featuring vaporization mass loss: (a) shows an isometric view of the melt pool temperature and velocity profiles with and without vaporization; (b) shows the cross-section melt pool profile and (c) shows maximum temperature and melt pool volume over time [34].	71
Figure 58: Cross section of the velocity (left) and temperature profiles of the vapor cavity due to evaporation and recoil pressure [34].	71
Figure 59: Density vs temperature for IN718, C103, Nb, Hf and Ti.	76
Figure 60: Specific heat vs temperature for IN718, C103, Nb, Hf and Ti.	77
Figure 61: Thermal conductivity vs temperature for IN718, C103, Nb, Hf and Ti.	77
Figure 62: Graph of thermal diffusivity functions and values for IN718, C103, Nb, Hf and Ti.	78
Figure 63: Longitudinal view of simulation results for C103 and IN718 at 450 $\mu$ s.	79
Figure 64: Cross-sectional view of simulation results for C103 and IN718 at 450 $\mu$ s.	79
Figure 65: Comparison between melt pool depth measurements for IN718 and C103.	80
Figure 66: Isotherm distribution between Ti-6Al-4V and niobium plates [72].	82
Figure 67: Melt pools on niobium(left) and Ti-6Al-4V (right) plates after application of laser pulses [74]	82
Figure 68: Thermal diffusivity plots of common additive manufacturing alloys and niobium and its alloys	84
Figure 69: Melt pool geometry for Nb-37Ti-13Cr-2Al-1Si from Guo et al [78].	84
Figure 70: Plot of melt pool depths between different alloys	85

# List of Tables

Table 1: Room Temperature ultimate tensile stress (UTS), yield strength (YS) and Elongation of as-built AM-printed parts of HT alloys. -----	15
Table 2: List of parameter combinations -----	21
Table 3: Summary of geometric dimensions and mesh settings. -----	30
Table 4: Temperature-dependent density equations. -----	36
Table 5: Thermal conductivity equations. -----	39
Table 6: Summary of settings for the IN718 Model. -----	42
Table 7: Properties of interest to be compiled formatted as: property, column name, [units] -----	43
Table 8: Initial analysis of variance results and linear regression for melt pool depth. -----	46
Table 9: Initial analysis of variance and linear regression results for bead width. -----	46
Table 10: Pearson correlation coefficient values between independent and dependent variables. -----	47
Table 11: Melt pool depth linear regression and ANOVA results for the complete dataset -----	54
Table 12: Melt pool depth linear regression and ANOVA results for each powder size distribution subsets -----	54
Table 13: Melt pool depth standard deviation between line numbers with each powder size distribution [ $\mu\text{m}$ ] -----	54
Table 14: Bead width linear regression and ANOVA results for the complete dataset -----	55
Table 15: Bead width linear regression and ANOVA results for each powder size distribution subsets: -----	55
Table 16: Bead width standard deviation between line numbers within each powder size distribution [ $\mu\text{m}$ ] -----	55
Table 17: Comparison between simulated vs experimental melt pool depth. -----	66
Table 18: Comparison between simulated vs experimental bead width. -----	66
Table 19: Niobium properties -----	74
Table 20: Hafnium properties -----	75
Table 21: Titanium properties -----	75
Table 22: Zirconium properties -----	76
Table 23: Projected properties of C103 used for the simulation -----	76
Table 24: C103 simulation results, sorted by surface energy density. -----	80
Table 25: Ti-6Al-4V properties -----	83

# Chapter 1: Introduction to High Temperature Alloys and Additive Manufacturing

## 1.1 High Temperature (HT) Alloys

### 1.1.1 General Properties and Application of HT Alloys

Nickel-based superalloys, such as Inconel 718 (IN718), and titanium alloys, such as Ti-6Al-4V (Ti64), possess mechanical behaviors that allow them to operate in challenging environments, such as high elevated temperatures. For this reason, the materials discussed in this study would be classified as high temperature (HT) alloys. Additionally, IN718 possesses other desirable mechanical properties, such as good creep resistance and fatigue life [Hosseini and Popovich]. Also, Ti64 benefits from high fracture toughness, corrosion resistance, biocompatibility, and high strength while having low density [1]. These properties enable these alloys to be utilized in a wide variety of fields. One of the foremost applications are aerospace components. The corrosion resistance of both materials also makes them suitable for chemical plants, and for Ti64, its biocompatibility is of interest for orthopedic implants.

However, despite their high operating temperatures, there is increasing demand for materials that can handle even more extreme environments. An example of this would be hypersonic flight where aerospace component could be exposed to temperatures above 1027 °C (1300K). Alloy IN718 has an operating temperature of up to 973K [2], and the mechanical properties of Ti64 are drastically reduced above this temperature. It also possesses only less than half of its tensile stress at room temperature [3]. Figure 1 shows the reduction of yield stresses of different materials at high temperatures.

The search for materials that can withstand such temperatures while maintaining acceptable mechanical properties have renewed interest in refractory materials, such as niobium (Nb) and tungsten (W). In the case of niobium, it exhibits one of the lowest densities of all the refractory metals. Research and alloy development based on these elements were active in the 1950s during the space race, and these materials were also investigated for use as possible turbine engine components before being considered for space propulsion and nuclear reactors. However, research on refractory materials slowed considerably as interest in nuclear energy for propulsion waned with the cancellation of NERVA (Nuclear Engine for Rocket Vehicle) [4].

Besides aerospace flight and propulsion, the potential applicable fields for refractory materials are the medical and chemical industries, as shown in Figure 2. Refractory alloys such as niobium have applications in electronics as capacitors and even superconductive materials due to their superconducting transition temperature [8]. The superconductive properties of these materials can be used in fabricated parts of linear accelerators for the study of elemental physics, which is being employed at Argonne National Laboratory (ARL) and the European Organization for Nuclear Research (CERN) [9].

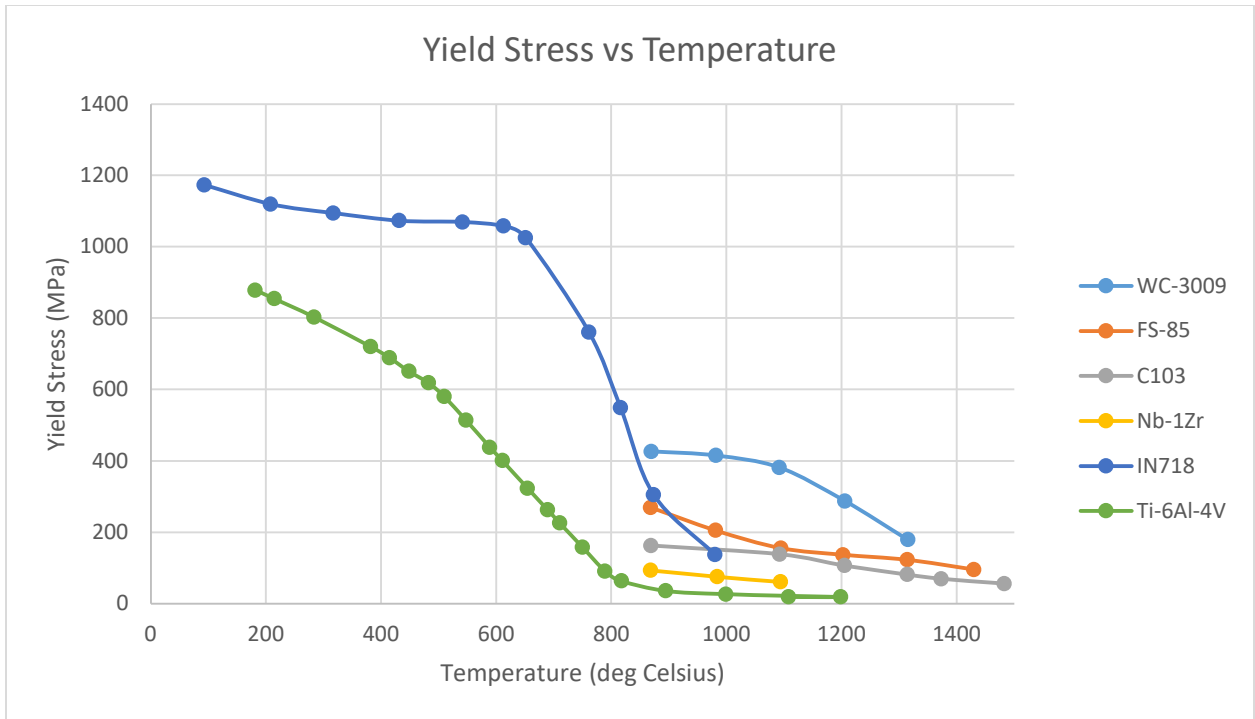


Figure 1: Yield Stress vs Temperature of IN718[5], Ti64 [3], Nb-based Alloys [7].



Figure 2: Parts created from Nb or Nb-based alloys through additive manufacturing: a propulsion part (left) [10] and a superconductive component (right) [9].

### 1.1.2 Challenges of Refractory Materials

The materials that will be discussed in this research exhibit very promising properties, but these properties also make them challenging to manufacture through conventional subtractive, i.e., machining, methods. For example, the impressive mechanical properties of IN718 also result in characteristics that makes machining difficult due to high tool wear [2]. In addition, machining can be wasteful when the subtractive method is employed for manufacturing a component made from these materials. For example,

the buy-to-fly ratio of Ti64 parts made through conventional manufacturing methods can be between 12 to 25 to 1 [1]. This means for every 100 kg of Ti64 material that is machined, only 4 to 8 kg would be realized in the part and 92 to 96 kg would be wasted as machining chips. For materials that are costly, such as refractory metals, these high buy-to-fly ratios further inhibit their use.

For refractory materials they are not only challenging to fabricate, but also prohibitively expensive and can be vulnerable to oxidation. In the case for niobium alloys, not only are they susceptible to oxidation at high temperature above 524K [11], but also are incompatible with conventional coatings. Attempts to alleviate these problems result in alloys with lower physical properties or compromises [4]. After 50 years since the cancellation of the nuclear propulsion program, which was one of the biggest endeavors for refractory alloy research, new technologies and processes have been developed that could expand the use of these promising materials. These technologies can help the development and implementation of refractory alloy applications. One such technology that has emerged is additive manufacturing, which may alleviate the machining problems of these materials while reducing waste.

## 1.2 Additive Manufacturing

Additive manufacturing (AM) is the process of adding material onto a substrate to produce a desired shape using individual layers. Shown in Figure 3 is a schematic of powder bed fusion (PBF), an AM process that involves the use of a laser or electron beam to selectively melt a small layer of powder to achieve an accurate two-dimensional representation of a desired shape. The process is repeated so that many layers are used to produce a three-dimensional part. There are several methods for AM that are applicable to metals; however, the two most common are PBF, described above, and directed energy deposition (DED), where the added material is partially melted by an energy source (either laser, electron beam or electric arc) that is manipulated to continually deposit material that ultimately becomes a near net-shape.

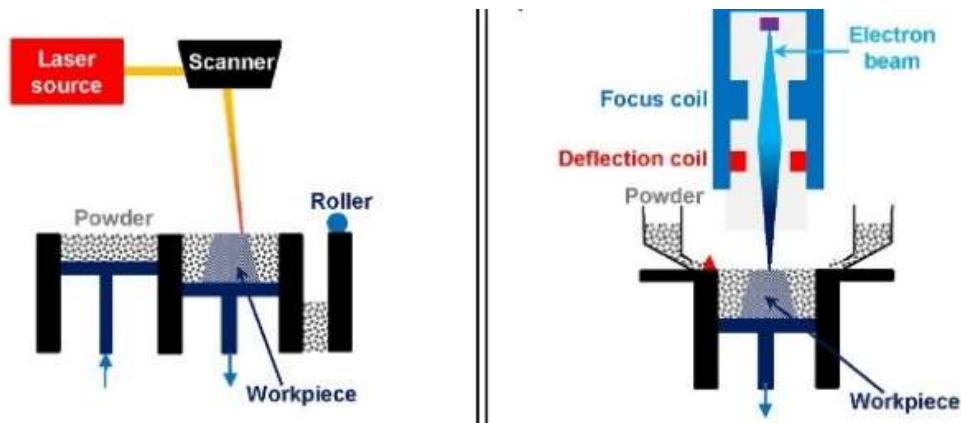


Figure 3: Schematic of a laser-based (left) and an electron beam-based (right) powder bed fusion (PBF) processes [2].

Most AM processes possess advantages that traditional manufacturing methods do not possess. One major benefit is geometric flexibility, and AM has the freedom to produce parts with complex shapes that machining or molding processes cannot create. An example of these complex shapes are gyroids where the internal channels are too complex for machining, as shown in Figure 4. The ability to produce complex shapes through AM also leads to other benefits. For example, AM process allows the production of consolidated parts with less components for assemble. A successful implementation of an AM part through consolidation is the LEAP engine jet injector. Consolidation of parts may be used to reduce manufacturing cost, as well as improve performance through modifications of the design. In the aerospace industry, manufacturing of parts strongly considers buy-to-fly ratio, and with AM the buy-to-fly ration is minimized. This is because AM may be used to create accurate features that greatly reduce machining requirements. According to Mireles et al, conventional machining has a buy-to-fly ratio of 20:1 or 50:1; whereas, with AM, this ratio is around 1.1:1, with minimal machining required to remove rough surfaces and support structures. Another bonus that AM provides in terms of cost savings is the ability to reduce the waste of expensive material through recycling of powder utilized within many of the processes [10].

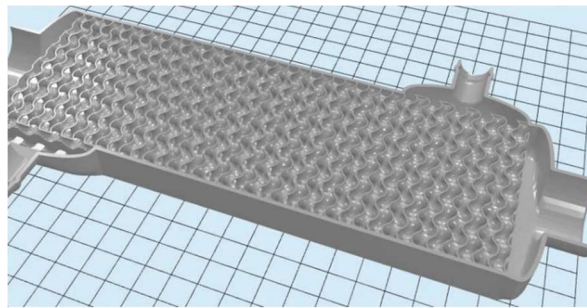


Figure 4: A 3D model of a heat exchanger with gyroid geometries that can be made possible by AM [12].

### 1.2.1 Additive Manufacturing of High Temperature Alloys

Additive manufacturing (AM) has been applied to high temperature alloys, and one of the most common materials is nickel-based superalloys, such as Inconel 718. Research on AM of these materials are numerous with extensive documentation on resultant properties being available. The viability of AM for other high temperature alloys based on propensity for cracking during processing can be deduced by their behavior during welding, the preceding technology behind AM. Lambert et al provides brief summaries of the welding behavior of refractory materials. Factors that need to be considered for welding these materials include ductile to brittle transition temperatures (DBTT), oxidation temperatures, and potential post-processing requirements to restore ductility and strength [13].

Another consideration for the viability of AM for these alloys is the powder feedstock, since the high melting temperature of these materials make processing of powder difficult. In terms of PBF, the powder feedstock must ideally be spherical to have optimal flow and spreadability across the build

platform. Philips et al described the current landscape of powder production of potential AM-compatible refractory alloys. For example, the most cost-effective method, the hydride-dehydride (HDH) process, tends to yield angular powders, which are not ideal for AM application because of uneven spreading in the powder bed. Consequently, poor-quality powder can result in defects and reduced mechanical properties in the final part. There is also the issue of which metals are compatible with the powder production methods based on the possibility of undesired interstitial contamination by oxygen and hydrogen. The electrode induction gas atomization (EIGA) process has provided promising results for powder production of refractory alloys since it minimizes reactions with the environment during spheroidization [4].

Recently, there has been significant efforts in studying AM of refractory materials. The most common AM methods explored were PBF with either laser or electron beams, with the latter employing a vacuum environment that minimizes oxidation [4]. Griemsmann et al, examined laser-based PBF of pure Nb with different parameters of laser power, scan speed, and hatch spacing (distance between laser weld tracks) on part quality [8]. Some of the specimens produced during these experiments yielded relative high densities (99%) using optimal parameters. Regarding mechanical properties, specimens produced using the optimal parameters resulted in ultimate tensile strengths of between 444 MPa to 525 MPa being achieved without post-processing. The strength exhibited from these samples was significantly higher than the ultimate tensile strength displayed by the wrought material, which was of 225 MPa. The author attributed the increase in strength due to the presence of oxygen in the laser-based PBF process [8]. Terrazas et al also performed studies on AM of pure Nb but using an electron beam energy source. This study yielded samples with comparable mechanical properties as wrought Nb; however, the yield strength (YS) and ultimate tensile strength (UTS) of these specimens were found to be 135 MPa and 205MPa, respectively.

Niobium-based alloys were also evaluated using AM with both mixed and pre-alloyed powders at NASA's Marshall Space Flight Center (MSFC). These studies utilized alloy C103, a Nb-based alloy that has been used in the aerospace industry. Studies of mixed and pre-alloyed C103 powder in the as-printed and heat-treated conditions were evaluated. The results indicated that samples with 99.99% of the theoretical density could be achieved with a slight increase by 0.003% after post-processing with stress relief (SR) and hot isostatic pressing (HIP). According to the results of tensile tests, the as-printed specimens provided an average YS of 560 MPa, UTS of 411 MPa, and percent elongation of 16.67%. Whereas the post-processed sample, which involved hot isostatic pressing at 1100°C, showed inferior yield and ultimate tensile strength but better ductility, displaying elongations of 20.8% and 18.9% with only stress relief and stress relief with HIP, respectively. This study asserted that material produced through AM had better UTS than wrought material at 24 °C but not at an elevated temperature of 1093 °C. Also, Mireles, et al showed that laser-based PBF could produce C103 alloy that exceeded the ASM specifications for UTS, YS and elongation of this material [10]. According to Lambert et al., the C103 material used to provide wrought properties during the MSFC evaluation represented recrystallized material, whereas, C103 in the cold-rolled state possesses a much higher UTS and YS, being 725 MPa and 670 MPa, respectively [13].

Another study by Philips et al also examined AM of C103 using laser-based and electron beam-based PBF. Additionally, this study also compared mechanical properties representing different orientations to examine the influence of anisotropy during solidification. Similar to the study conducted by MSFC, Philips et al also examined mechanical properties in both room and at elevated temperatures of

1366K, 1589K, and 1755K. The results of the material produced using laser-based PBF showed YS and UTS at room temperature to be very comparable to wrought material but inferior in percent elongation. These comparisons remained the same at 1366K, but at 1589K and higher the printed samples displayed lower YS and higher UTS. In terms of orientation, the specimens that were parallel to the build (transverse) direction and perpendicular to the build (longitudinal) direction exhibited similar mechanical properties. The specimen produced using laser-based PBF in the as-built condition, tested at room temperature, exhibited a YS of 438 MPa in the transverse direction, compared to the YS of 430 MPa in the longitudinal direction. The results of tests on the material produced using the electron beam-based PBF process tended to show lower UTS but comparable YS. When these results were compared to the specification for minimum strength used during the MSFC study, the material manufactured through electron-beam PBF exhibited lower UTS but higher YS and percent elongation [4]. There are also AM studies tackling other novel, high temperature materials using AM. Tungsten (W), as a pure metal, perhaps embodies refractory behavior as it has the highest melting temperature of all the metallic elements. With its relatively high thermal conductivity, tungsten also has potential applications in demanding environments, such as X-ray tubes and nuclear fusion reactors. However, these properties also make AM of tungsten very challenging. Dorow-Gerspach et al created AM-printed samples with pure W using electron beam-based PBF. In this study, material created using PBF exhibited density of 99% of theoretical density; however, cracking was also evident during the process [14]. Wang et al also examined printing of tungsten using laser-based PBF, which yielded samples with only 96% of the theoretical density. Their study also considered the absorptivity of laser energy with the tungsten, which is a consideration when using a laser-based process. They concluded that the polyhedral shaped powder, represented by the powder material that they had employed, absorbs better than spherical powder [15]. Hankwitz et al, on the other hand, blended tungsten and a Nb-based alloy (Nb-1Zr) with the purpose of using the tungsten additives to increase mechanical properties of the experimental composition at elevated temperatures above 1000°C. It should be noted that Hankwitz et al resorted to blending of powder instead of pre-alloying due to the cost effectiveness of this technique but acknowledged potential difficulties in interdiffusion between the materials involved. The authors concluded that the samples displayed high density but also exhibited a decrease of YS, UTS and ductility, through percent elongation, when compared Nb-1Zr. The root of these compromised mechanical properties, according to the author, was believed to be attributed to the difficulties in interdiffusion of blended components, as well as melt pool ejection, which could be reduced through post-processing [16].

The results within the literature and discussed in this section indicated that AM could be a viable process for fabrication of components produced using various high temperature-alloys if the resultant material displayed adequate properties. Table 1 summarizes the mechanical properties of AM material discussed previously. For the sake of brevity, only as-built properties are listed in the table. General assumptions can be made based on the data reflected in the table, such as HT material produced using laser-based PBF yielded higher YS and UTS at the cost of ductility. Also, material produced using electron beam-based PBF generally exhibited superior ductility, but for both processes, yield strengths tended to be lower than wrought material. The mechanical properties of the material could also be attributed to the microstructures formed during AM based on the level of energy utilized during processing. In AM, the resultant microstructure could potentially yield a cellular, columnar, or equiaxed solidification morphology depending upon the rate of solidification and cooling. Based on the literature examined, PBF using laser or electron beams resulted in microstructures and properties having an anisotropy representing orientations parallel and perpendicular to the build direction. Based on directional solidification inherent in the process, the material displayed cellular or columnar growth with the axes of the cells being normal

to the build direction, as shown in Figure 5 for Laser-PBF and Figure 6 for electron beam-PBF [4,6]. Obviously, understanding the mechanisms driving the formation of microstructures is extremely important if the potential of AM technology is to be fully realized.

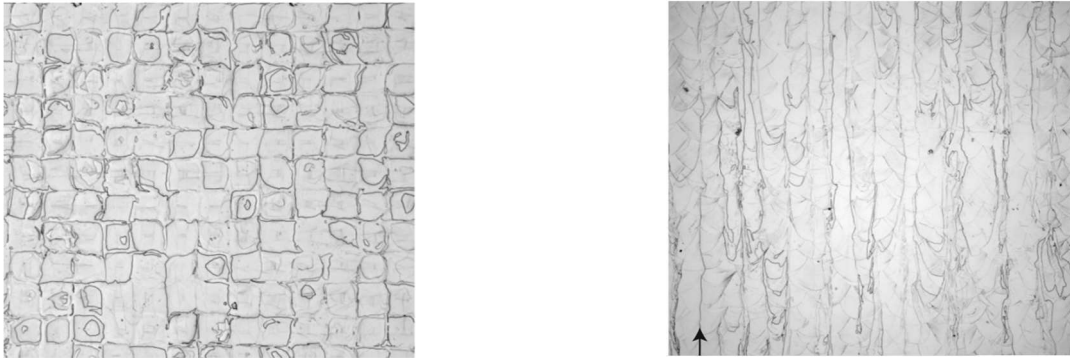


Figure 5: C103 Microstructures from Laser-PBF process in both the transverse (left) and longitudinal (right) orientations[4].

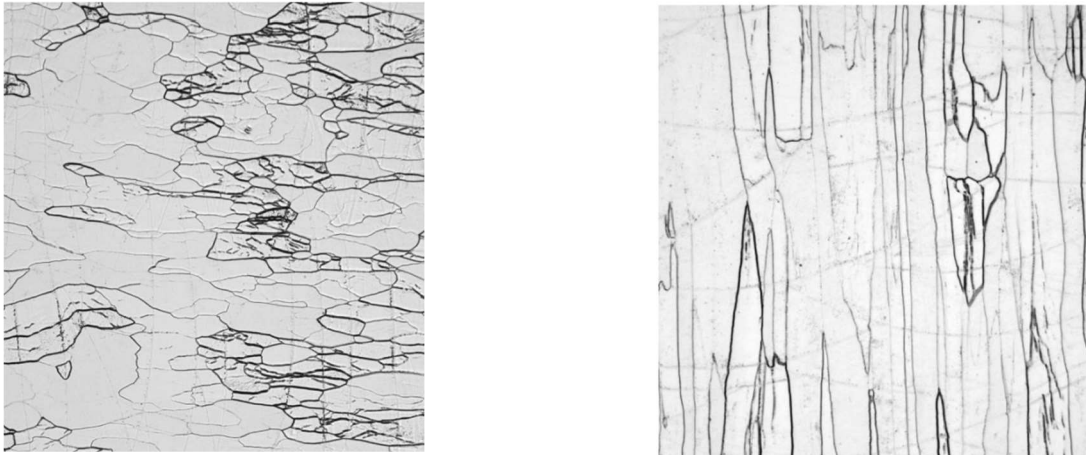


Figure 6: C103 Microstructures from electron beam-PBF process in both the transverse (left) and longitudinal (right) orientations [4].

The environment used during laser and electron beam PBF may also influence the resultant mechanical properties of the material produced using these processes. Electron beam processing requires a vacuum environment since air molecules may interfere with the stream of electrons used for heating the material, while inert gases, such as argon are used for processing with a laser beam. Although the laser-based process utilizes an inert environment, small amounts of oxygen, between 5 to 300 ppm, may be present. This makes laser powder bed fusion significantly more prone to oxidation than the electron beam powder bed fusion process. Griemsmann et al, attributed the increase in mechanical properties of their sample either to the powder atomization or introduction of oxygen in the laser powder bed fusion process [8].

Table 1: Room Temperature ultimate tensile stress (UTS), yield strength (YS) and Elongation of as-built AM-printed parts of HT alloys.

Source	Material (Method, Orientation)	YS (MPa)	UTS (MPa)	Elongation (%)
[2]	IN718 (Wrought)	~900	~1200	15
[2]	IN718 (Laser-PBF)	~700	~1000	25
[2]	IN718 (Electron Beam-PBF)	~800	~1100	20
[1]	Ti-6Al-4V (Laser-PBF, transverse)	1062	802	12.7
[1]	Ti-6Al-4V (Laser-PBF, longitudinal)	1035	910	3.3
[9]	Nb (Wrought)	135	205	45.2
[9]	Nb (Electron Beam-PBF)	141	225	34.5
[8]	Nb (Laser-PBF)	316	525	12.6
[4]	C103 (Wrought)	283	411	41
[4]	C103 (ASTM Specifications)	262	372	20
[4]	C103 (Laser-PBF, longitudinal)	438	533	30
[4]	C103 (Electron Beam-PBF, transverse)	273	356	43
[4]	C103 (Electron Beam-PBF, longitudinal)	285	353	30
[10]	C103 (Laser-PBF, transverse)	420	527	29
[16]	Nb-1Zr	366	428	23.6
[16]	Nb-10W-1Zr	301	357	13.2
[16]	Nb-20W-1Zr	-	170	4.3

### 1.2.2 Challenges in the Additive Manufacturing (AM) Process

Because AM technology is considered to be in its formative stage, there remain challenges to overcome if widescale adoption of AM is to be realized. In many instances, the root of these adversities is due to uncertainty involving the complex physics governing the process or the intricate kinetics and thermodynamics that guide microstructural evolution under extreme anisothermal conditions. For AM parts to be applied commercially, predictability of quality and properties of these parts is paramount, especially for the aerospace industry. As alluded to earlier, a common feature of AM-printed parts is microstructural and mechanical anisotropy that result in varying characteristics depending upon orientation. In terms of a part printed using laser-based PBF, mechanical properties and microstructure differ if measured parallel or perpendicular to the build direction, and this variation may be significant.

Another challenge involving AM components and structures is that the fatigue life is generally lower when compared to machined or forged parts. This can be attributed to stress concentrators, such as

rough surface finish, internal defects, such as porosity or lack-of-fusion, and variation in microstructure and properties throughout the part. Internal defects involve voids created within the material. At insufficient energy densities, lack-of-fusion may occur, which is a flaw that is created when melting and resolidification are not accomplished between the substrate, adjacent deposits, or a previous layer. Porosity may also form during processing and may be attributed to absorption of gaseous species or metal vapor that precipitates a pore upon solidification, or instability and collapse of the vapor cavity or keyhole resulting in pores forming near the root of the deposit. While lack-of-fusion results from an inadequate amount of energy for melting and solidification, porosity due to precipitation of gas porosity due to evaporated metal is exacerbated using overly high energy densities, which is illustrated in Figure 7. This can also lead to delamination of layers, which can lead to part rejection as shown in Figure 8.

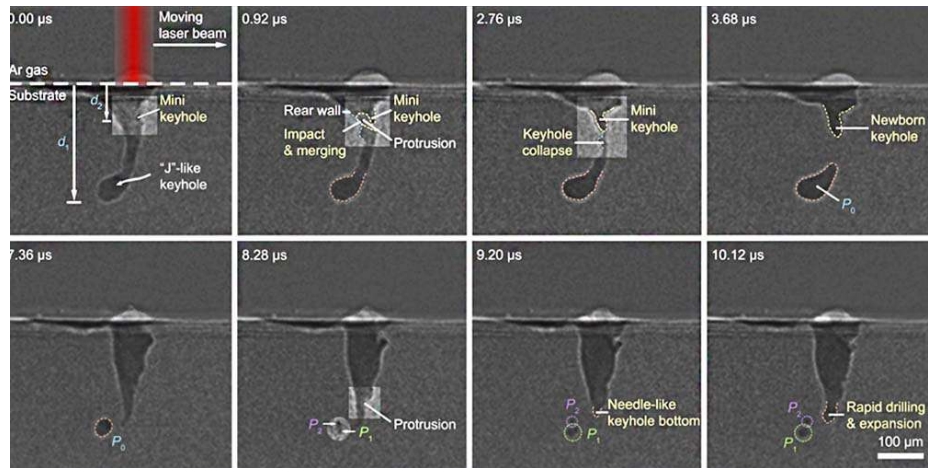


Figure 7 In-situ x-ray observation of a keyhole porosity formation [17].

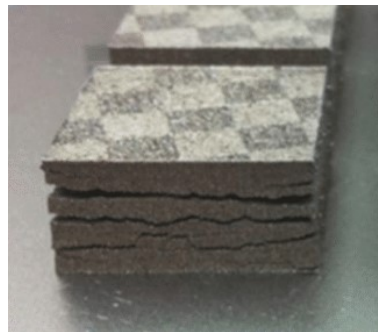


Figure 8 Delamination defect of an AM-printed part [18].

Although it is important to minimize the formation of defects through optimal process parameters and conditions, it is also imperative to be able to identify the potential presence of defects, should they occur. Hence, having a well-defined processing window, along with a full understanding of the physics behind the AM process may be used to increase the predictability of quality in the fabrication of parts.

Multiple characterization techniques have been applied to AM-fabricated parts such as microscopy, tomography, and x-ray diffraction. Both optical and electron microscopy allows for macro and micro interrogation of AM-printed samples. With these techniques, features such as melt pool geometry, grain morphologies, elemental distribution of concentration, and grain orientations may be ascertained. Inspection techniques, such as radiographic-based computed tomography (CT) can be used to detect internal defects or even observe their formation. Mireles et al pointed out that AM-printed C103 samples may not be compatible with CT due to the high atomic number of refractory elements, such as niobium, which causes attenuation of the x-ray signals [10]. Other useful experimental tools for the study of the AM process include infrared sensors to evaluate in-situ thermal responses and acoustic sensors as an alternative method to detect defect formation during processing.

Besides of the impact of the AM process on the potential integrity of the part, engineers and manufacturers who are interested in utilizing AM must also consider the cost in time and money. Mireles et al specified that C103 powder is 33% more expensive than wrought feedstock, on average [10]. Hence, AM is usually reserved for applications that require a high degree of complexity where the material is utilized efficiently. Additionally, AM is not recommended for parts requiring high production rates due to the extremely long time for completion of the AM process and post-processing. This means that the best parts for AM applications are those of critical or specialized functions that cannot be easily manufactured by conventional means and does not require fabrication on a massive scale.

## **Chapter 2: Rationale and Objective of Current Study**

As was discussed above, empirical information obtained through well-defined experiments may be used to aid in addressing the various challenges that exist for implementing additive manufacturing (AM) for parts having a critical role in complex systems. Experimental data may also be augmented with theoretical tools, such as simulations, to increasing the basic understanding of the AM process as applied to these unique materials. One of the most common AM experiments is the evaluation of single-track deposits. This involves experiments where the power source, laser or electron beam, is applied to the powder bed as a single scan path. Utilizing metallographic techniques for viewing the cross-section, the resultant deposit may then be evaluated for its important geometric dimensions. The single-track approach for evaluating the process based on a single deposit is illustrated in Figure 9. As shown in the figure, the essential dimensions are the height of the deposit, width of the deposit, and depth of penetration. Guo et al used the ratio between the depth and width of the melt pool to determine the impact of a problematic combination of two parameters, laser power and scanning speed. Criteria for these, potentially, defect-inducing parameters were found to be a very wide width with shallow depth, which implied lack-of-fusion or a very high melt pool depth but having a narrow width, which could indicate instability of the vapor cavity and keyhole porosity [19].

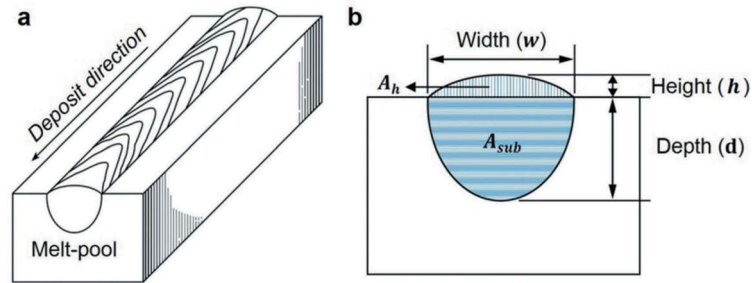


Figure 9: Single-Track Weld(left) and Characterization of the Single-Track Cross-Section (right) [20].

Experimental studies of the AM process, however, can be expensive, time consuming and may not capture all aspects of the physics. In these cases, external process sensors may be used to greater insight into the influence of process anomalies with potential defects. For example, in-situ observations such as using spectroscopy of the plasma and infrared sensors for thermal observations may be employed to monitor the thermal response of the material, which may suggest instability of the vapor cavity and potential keyhole porosity. Additionally, detailed process evaluations are not just laborious but also time consuming since the printing process can take several hours or even days for one print. The use of advanced tools, such as physics-based simulations, may also be employed to predict and gain an improved understand of the physical phenomena representing the AM process. These phenomena, which may be very difficult to view outside of virtual simulations, include transfer of energy and mass through beam and material interaction, Marangoni convection, and evaporation, to name a few. Figure 10 provides a schematic representation of many of the phenomena that can be considered by virtual simulations.

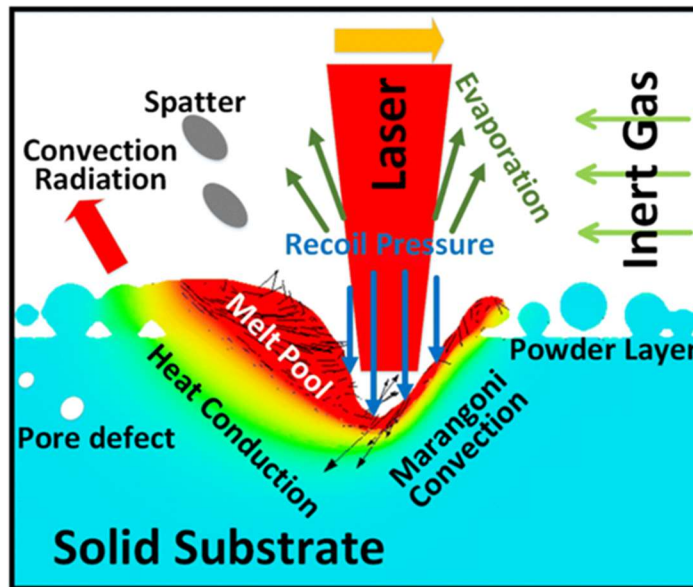


Figure 10: Physical phenomena in the AM process [21].

Another useful technology that may be brought to bear for establishing optimal AM processing conditions is informatics, which may be utilized to analyze experimental data to their fullest potential by finding and recognizing subtle yet vital patterns and relationships within the process. Due to the complex physics governing the AM process, data informatics provides a means to unravel and detect causal relationships involving processing conditions and quality of fabricated parts. Two examples on the utilization of informatics are featured in Figure 11. Griemsmann et al used experimental data coupled with statistical techniques to create a process map that could identify parameters that would result in increased part density, while Meng et al utilized a machine learning algorithm to construct a prediction map describing melt pool depth using the Gaussian process method.

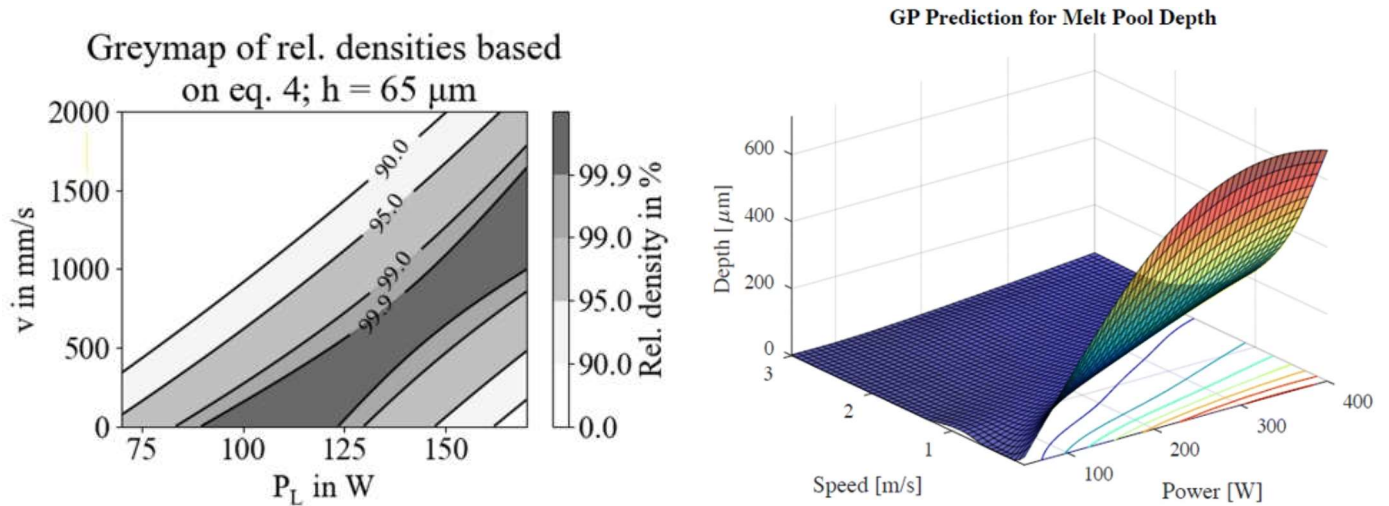


Figure 11: Process maps of predicting: relative density (left) [8] and melt pool depth(right)[22].

## 2.1 Objectives of This Research

The primary goal of this thesis is to develop tools that may be used to define relationships for laser powder bed fusion process parameters that minimize the potential of process-related defects. The first step of this study was to conduct detailed laboratory experiments using Inconel 718 and single-track melt pools to determine the impact of laser power and scanning speed parameters on key deposition attributes. The effects of powder size were also considered during the analysis of the data using data informatics methods. The results of the laboratory experiments would be used as a reference for subsequent steps, which was the construction of a physics-based model representing the laser-based PBF process and the use of this model to guide establishment of parameters that would produce material having minimal internal defects.

The physics-based model would be initially developed for Inconel 718 and would utilize features, such as a volumetric heat source representing attenuation of the laser beam in the powder layer and temperature-dependent behavior of thermophysical properties, such as density, heat capacity, and thermal conductivity. Thermal conductivity would have both temperature and path dependence based on properties of the material as a powder or fully consolidated after melting and solidification. Surface heat losses and

Marangoni effect would also be implemented as boundary conditions. The results of virtual simulations would then be compared to experimental data to determine the accuracy of the model and applicability for its use in process development.

An extremely important aspect of extending the physics-based model to use for refractory materials is the ability to compile and employ thermophysical properties of these materials as inputs for virtual simulations. This poses difficulty since there is scarcity of these properties in the literature for these materials. Sparse data exist for these thermophysical properties of refractory materials at room temperature, while good temperature-dependent data is virtually non-existent within the open literature. Therefore, another crucial step in this investigation would be the development of a database of material properties of, both, the elemental components of refractory materials as well as the alloys of interest, if those values are available. This would enable the application of the physics-based model as a tool for exploring and identifying promising processing conditions for these novel materials.

## Chapter 3: Experiment Description and Methodology

### 3.1 Physical Experiments and Characterization

This section involves the description of laboratory experiments for creating single tracks samples made from the laser powder bed fusion process. The specimens underwent sample preparations for optical microscopy for characterization of the melt pool. After the measurements were collected, the data was then processed with exploratory data analysis and statistical methods. The single-track samples were printed and characterized at the Commonwealth Center for Advanced Manufacturing (CCAM). The laser powder bed fusion machine used to create the samples was an EOS Model M290 powder bed fusion system.

#### 3.1.1 Experimental Layout

As stated in the previous chapter, the experimental part of this study involved the characterization of melt pool tracks. The main parameters of interest were laser power and scan speed with three levels for each variable. Utilizing a full-factorial design of two variables at three levels resulted in a total of nine possible combinations. The three powers utilized for the experiments were 225, 285 and 345W, and the three scan speeds were 760, 960, and 1160 mm/s. Each combination, classified as line number, could be quantified by a corresponding energy density term, specifically the surface energy density, also known as fluence, which is calculated by

$$\text{Surface Energy Density} \left[ \frac{J}{mm^2} \right] = \frac{P}{v * 2r_0} \quad (1)$$

where  $P$  and  $v$  are the parameters of laser power and scan speed, respectively. The other variable,  $r_0$ , is the beam radius valued at 40  $\mu\text{m}$ , which, when doubled, is the spot diameter. The calculations for surface energy density for each line number are listed in Table 2. It was observed that the surface energy densities for the Line Numbers of 1, 5, and 9 have very close surface energy density values of 3.7, 3.71, and 3.72  $\text{J}/\text{mm}^2$ , respectively. As this proximity would make these values indiscernible in plotting, the

surface energy values of Line Numbers 1 and 9 would be staggered by 0.30 and would be represented with the values of 3.4 and 4.02 J/mm<sup>2</sup>, respectively, instead. Using these numbers would make responses associated with Line Numbers 1 and 9 distinguishable from Line Number 5 in subsequent figures.

Another parameter considered during experimentation, which was blocked as a complete set of experiments, involved three different powders size distributions. The three powder size distributions were categorized using the distribution representing 10% and 90% mass, which resulted in a nominal size distribution of D<sub>10</sub>/D<sub>90</sub> = 15/45 μm, a distribution of finer powder size having D<sub>10</sub>/D<sub>90</sub> = 10/40 μm, and a distribution representing coarser powder size at D<sub>10</sub>/D<sub>90</sub> = 25/55 μm. To simplify calculations and avoid multicollinearity, the powder size distribution were also represented by the mean powder size, D<sub>50</sub>, which was 30 μm, 25 μm, and 40 μm for the nominal, fine and coarse powder sizes, respectively.

The build layout for the experiments were arranged into nine printed blocks housing three single-track lines. Each single-track line was associated with parameters for a particular line number, along with two replications for each build. Figure 12 shows the arrangements of each line number in each block.

Table 2: List of parameter combinations

<b>Line Number</b>	<b>Laser Power (W)</b>	<b>Scan Speed (mm/s)</b>	<b>Surface Energy Density [J/mm<sup>2</sup>] (Stagger)</b>
1	225	760	3.70 (3.4)
2	285	760	4.69
3	345	760	5.67
4	225	960	2.93
5	285	960	3.71
6	345	960	4.49
7	225	1160	2.42
8	285	1160	3.07
9	345	1160	3.72 (4.02)

This set-up provided three instances to measure the response, or dependent variables, for each combination of parameters. As mentioned above, the experiments for the different powder size distributions were blocked, which meant that the entire experiment was repeated using the different powder sizes. After the print, each block representing the line scans were machined out of the substrate using electrical discharge machining (EDM). Each EDM-machined block was also segmented as to the start, middle, and end of the line. These values were averaged to represent critical features of melt pool geometry, bead width and melt pool depth. With the three levels of laser power, scan speed, and powder size distribution, along with two replications of each line numbers and three segments of each line, the total number of experimental results yielded 243 data points.

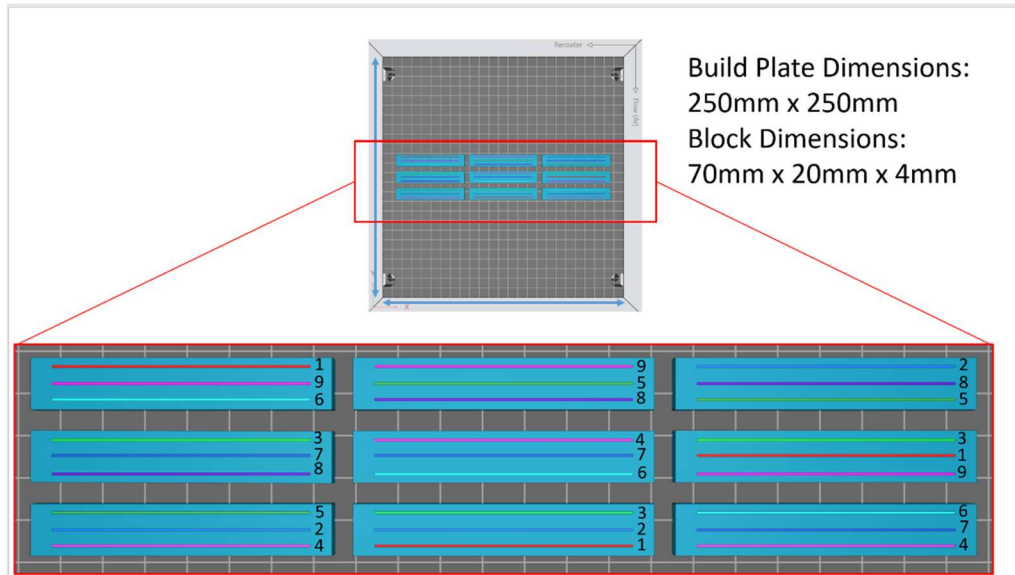


Figure 12: Arrangement of the melt pool tracks, and their line numbers as listed in Table 2.

### 3.1.2 Characterization

The single laser scan tracks were characterized using optical microscopy to ascertain details regarding the size of the melt pool and critical dimensions representing each line number. The block segments were first epoxy mounted, with the mounts later sealed within a vacuum chamber to remove trapped air bubbles and left to harden overnight. After the epoxy mount has hardened, the preparation of the specimens for optical microscopy were then conducted. This involved grinding the mounted samples using 325 to 1250 grit paper, followed by polishing using 9  $\mu\text{m}$  to 1  $\mu\text{m}$  diamond suspension polishing compound. The blocks were then etched with the mixture of 5 g of copper chloride, 100 mL of hydrochloric acid, and 100 mL of ethanol. This procedure would be considered typical for optical microscopy of nickel-based materials. Optical images showing the cross-section for each line scan at the beginning, middle, and end of the track were obtained for each run using an Olympus GX71 metallograph at 20x magnification. The digital images obtained from the microscope were then transferred to ImageJ, an open-source image processing system, for analysis. During image processing using the ImageJ software, the brightness and contrast of the images were adjusted until the boundaries between the single-track melt pool and the printed block were discernable. Critical dimensions representing the depth and width of the solidified melt pool were obtained. Figure 13 shows a cross-section of the melt pool and how the dimensions were measured.

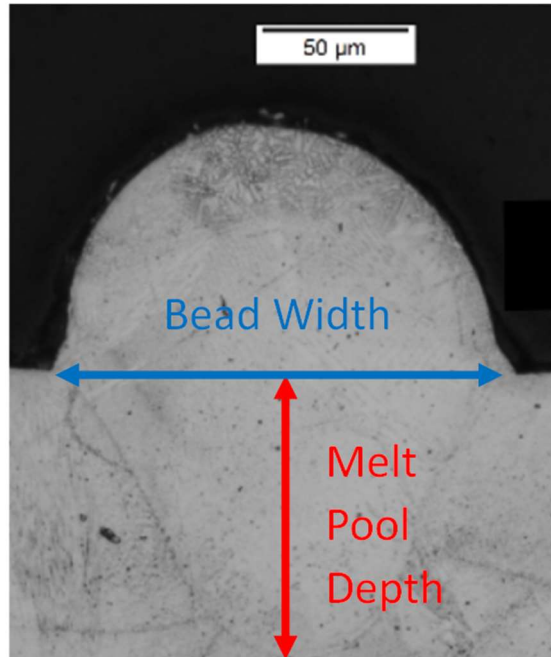


Figure 13: Characterization of the Melt Pool.

### 3.1.3 Data Processing

With the abundance of data obtained from the melt pool measurements, statistical examination of the data was utilized. Exploratory data analysis (EDA) methods were conducted to create initial impressions of the data through visual representations. This approach enables obvious outliers and relationships in the data to be easily discerned and was useful in determining the direction of the analysis in terms of data informatics. The EDA approach allows for immediate recognition of patterns within the data such as the identification of outliers using the boxplot method and visualization of the distribution of the melt pool geometry responses through histograms. The relationships between the independent process variables and the dependent track dimension variables were examined using analysis of variance (ANOVA).

The boxplot allows for the determination of outliers within the dataset, while allowing for analysis and adjustment of the data. This was performed by first finding the upper and lower extremes and the median of the data or subset. The upper and lower quartile was found by determining the median of the dataset and the upper and lower extremes, respectively. The upper quartile, median, and lower quartile forms the “box” of the plot. The difference between the quartiles is called the inter-quartile range (IQR). If the distance between a datapoint and either quartile is more than 1.5 IQR, it can be designated as an outlier and potentially removed to adjust the dataset. Figure 14 from Komoroski et al [23] shows the box method and its components. With the dataset, the boxplot was applied for each response, melt pool depth, and bead width.

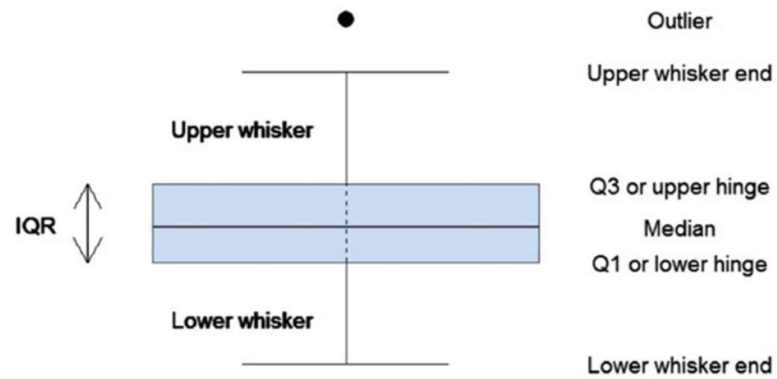


Figure 14: Boxplot and its Components [23].

Boxplots were also used to examine variance within a group i.e., the melt pool depth of a line number with the same powder size distribution. Evidence of high variance within a group was indicated by a larger IQR or “box”. Variance was also examined between groups, such as the melt pool depth measurements between different line numbers within the same powder size distribution [24]. To aid in the visualization boxplot, dot plots were added to see how each point varied within each group. Dot plots may be used in a similar manner to boxplots, with the box and whisker replaced as dots. This allowed better visualization of the distribution of each sample within a group, such as whether the sample group tended to be more towards the median or more spread out. A comparison between a boxplot and a dot plot is shown in Figure 15.

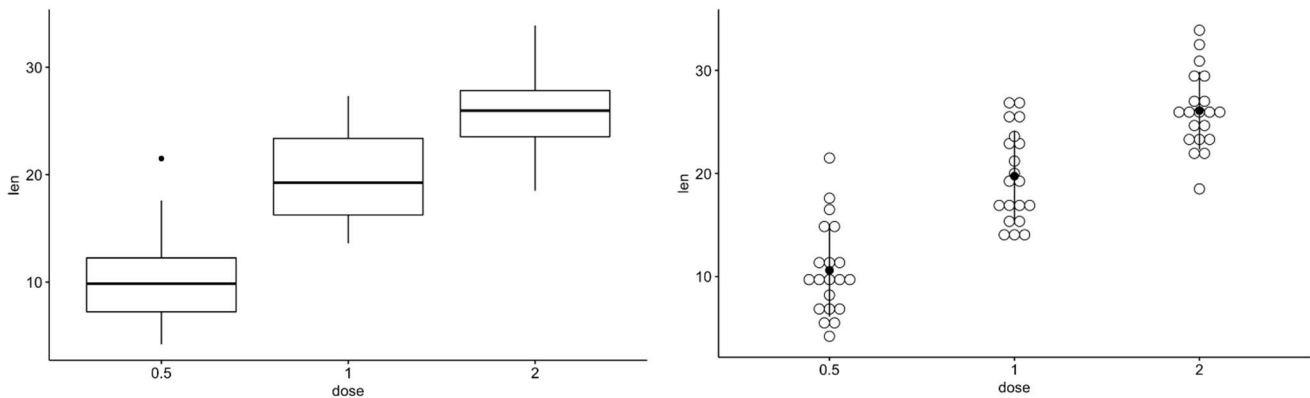


Figure 15: A boxplot(left) and its corresponding dot plot(right) [25, 26].

Another EDA method applied to the dataset were histograms. In a histogram, the responses are sectioned into intervals of bar plots in the x-axis. The y-axis is the frequency of which interval appears in the dataset. In other words, if there are more data points with a response within the range of 51 to 100  $\mu\text{m}$ ,

then this interval would have a higher frequency. Sorting the frequency of a data intervals in a histogram provides visual insight for the data, such as distribution, central tendency, and spread [23].

The correlogram, another EDA method, was also created to examine the potential relationships between the primary process parameters and powder size distribution and critical melt pool geometries of depth and width. The correlogram visually organizes the correlation between two variables into a matrix, as shown in Figure 16. The dark blue squares indicate a more positive correlation between two variables, while conversely, the dark red squares indicate a more negative correlation. The method for finding the correlation value utilized the determination of the Pearson Correlation Coefficient (PCC) [27], which is calculated using:

$$PCC = \frac{\sum(x_i - \bar{x})(y_i - \bar{y})}{\sqrt{\sum(x_i - \bar{x})^2 \sum(y_i - \bar{y})^2}} \quad (2)$$

where  $x_i$  is a sample of the  $x$  variable and  $\bar{x}$  is the mean of the  $x$  variables, while  $y_i$  is a sample of the  $y$  variable and  $\bar{y}$  is the mean of the variables. The  $x$  or  $y$  variables can be any of the variables examined in this study. The results of the PCC calculations are normalized, which means its outputs can only range between -1 and +1.

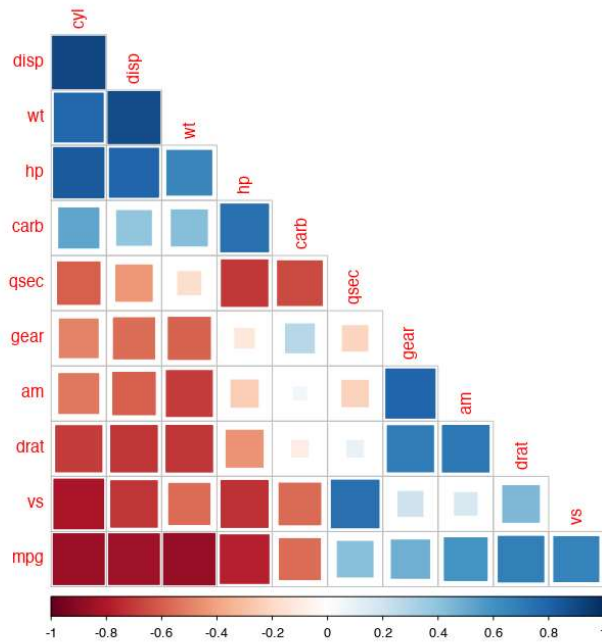


Figure 16: Example of a correlogram [28].

The statistical analysis of the data start with Analysis of Variance (ANOVA) to examine the statistical significance of each parameter (laser power, scanning speed, and powder size) for predicting each response variable of melt pool depth or melt pool width. The metric for determining the statistical significance was the p-value, which is the probability of obtaining an extreme measurement relative to the rest of the data. The p-value is weighed against the critical value,  $\alpha$ , to determine whether to reject the null hypothesis. An example of a null hypothesis would be stating that the responses between an independent variable such as powder size distribution can be considered the same. The null hypothesis can be rejected if the p-value is less than the critical value,  $\alpha$ , which is valued as 0.001, unless noted.

A linear regression of the data provided coefficients for each independent variable as well as its coefficient of determination ( $R^2$ ). This value can be found through the following equation:

$$R^2 = 1 - \frac{RSS}{TSS} \quad (3)$$

The residual sum of squares (RSS), which is the sum of the squared difference between the observed value,  $y_i$ , and the predicted value by the regression,  $\hat{y}$ , may be defined through:

$$RSS = \Sigma(y_i - \hat{y})^2 \quad (4)$$

Also, the total sum of squares (TSS), which is the total of squared differences between observed values,  $y_i$ , and the mean value of the data,  $\bar{y}$ , and is determined by:

$$TSS = \Sigma(y_i - \bar{y})^2 \quad (5)$$

If a regression fits well with the data, the total amount of residuals would be reduced, and thus, the  $R^2$  value will be higher. The  $R^2$  of each regression was used as the metric as to how well the linear equations fit the dataset.

## 3.2 Model Development

The virtual simulations were performed using ANSYS Fluent 2021 R1, which utilizes computational fluid dynamics (CFD) calculations. The model consisted of a domain having two regions, the topmost region representing the powder layer with representative material properties and the remaining portion of the computational domain representing the substrate and having bulk properties of the material. The mesh construction involves defining a refined region, which contained smaller elements and provided higher resolution compared to the rest of the model. Different properties were also assigned to the powder and bulk regions to acknowledge the distinction in the heat transfer behavior of these very different materials. Boundary conditions were applied for symmetry at the center-point, as well as heat losses due to convection and radiation at the surfaces, heat input due to the energy of the laser, and Marangoni effect of the fluid of the molten pool. The heat source relationship was from McVey et al [29], which represents a Gaussian energy distribution in the X-Y plane and exponential decay within the porous powder layer through an attenuation coefficient.

During CFD calculations, three equations govern the computations were utilized and represented conservation of energy, momentum, and continuity. The conservation of energy, which is based on energy being applied by the laser, some being retained within the material as an increase in temperature, while the remaining energy is conducted away and removed from the surface. During this process, increasing temperature within the material may result in melting and solidification under the moving heat source. The conservation of energy that is applied within ANSYS Fluent [30] is shown in Equation 6 as:

$$\frac{\partial}{\partial t}(\rho H) + \nabla \cdot (\rho \vec{v} H) = \nabla \cdot (k \nabla T) + Q_{heat} \quad (6)$$

where  $\rho$  is density,  $k$  is thermal conductivity,  $\vec{v}$  is the velocity of the heat source, and  $Q_{heat}$  is the representation of the heat source, which will be elaborated on in the section *Heat Source Shape and Position*, while  $H$  is the enthalpy, which is calculated from:

$$H = h + f_l L_{fus}$$

where in the above:

$$h = h_{ref} + \int_{T_{ref}}^T c_p dT$$

$h$  represents the sensible enthalpy,  $h_{ref}$  is the reference enthalpy, and  $c_p$  is the specific heat at constant pressure. In the above equation,  $f_l$  is the liquid fraction as a function of temperature between the liquidus temperature,  $T_l$ , and solidus temperature,  $T_s$ , and  $L_{fus}$  is the enthalpy of fusion. The liquid fraction is represented by:

$$f_l = \frac{T - T_s}{T_l - T_s}$$

The conservation of momentum involves the flow behavior of the melt pool. Equation 7 shows the relationship governing the conservation of momentum used within ANSYS Fluent [30]:

$$\frac{\partial}{\partial t}(\rho \vec{v}) + (\rho \vec{v}) \nabla \cdot (\rho \vec{v} \vec{v}) = -\nabla p + \nabla \cdot (\bar{\bar{\tau}}) + \rho \vec{g} + S \quad (7)$$

As in the conservation of energy,  $\rho$  is density of the material and  $\vec{v}$  is the velocity, while other variables are used to describe the state and response of the material due to the presence of forces acting on the material. These variables include:  $\vec{g}$  for gravity,  $p$  for static pressure, and  $\bar{\bar{\tau}}$  being the stress tensor which is defined by:

$$\bar{\bar{\tau}} = \mu \left( (\nabla \vec{v} + \nabla \vec{v}^T) - \frac{2}{3} \nabla \cdot \vec{v} I \right)$$

where  $\mu$  is the viscosity, and  $I$  is the unit tensor. The variable  $S$  can be external forces, momentum forces, or sinks. In the case of the using the solidification and melting model in ANSYS Fluent,  $S$  is defined by Equation 8.

$$S = \frac{(1 - f_l)^2}{(f_l^3 + 0.0001)} A_{mush} (\vec{v} - \vec{v}_p) \quad (8)$$

where in the above equation,  $f_l$  is the liquid fraction,  $\vec{v}$  is velocity, and  $A_{mush}$  is the mushy zone constant, which determines the dampening of the fluid flow within the mushy state. In this model, the value of the constant  $A_{mush}$  was to  $10^7$ . ANSYS recommends this value be between  $10^4$  and  $10^7$ , as exceeding this value may cause the melt pool shape to become unstable. Therefore, the latter value was chosen. With this momentum sink term, the velocity decreases as the values of  $f_l$  decreases until it reaches zero for the solid domain.

Conservation of mass is written as Equation 9, with the left-right side equal to zero to signify no mass added in the model.

$$\frac{\partial \rho}{\partial t} \cdot \nabla(\rho \vec{v}) = 0 \quad (9)$$

Within the computational scheme employed by ANSYS Fluent, many of the variables may be defined as a function of temperature through User-Defined Functions. During construction of the current model, various variables were described as a function of temperature through relationships programmed in C to apply an accurate representation of the phenomena, such as the distribution and attenuation of the heat source, thermophysical properties describing the material, and heat losses due to radiation, convection, and evaporation of the surface. In many instances, the values of these variables were constantly evaluated due to dependence on temperature, as well as state of the material.

### 3.2.1 Geometry and Mesh Construction

The geometry construction of the model consisted of three regions: the topmost region under the heat source representing the powder layer and below this region, representing the bulk material. The third region, classified as the refined region, includes the aforementioned regions located at the corner where the heat source is applied. The arrangement of these regions is illustrated in Figure 17. The purpose of the refined region was to allow for a much higher resolution of temperature over shorter distances, necessary for accurately depicting the high rate of change associated within this area. This is because most of the material's response to the laser-material interaction occurred just below the heat source.

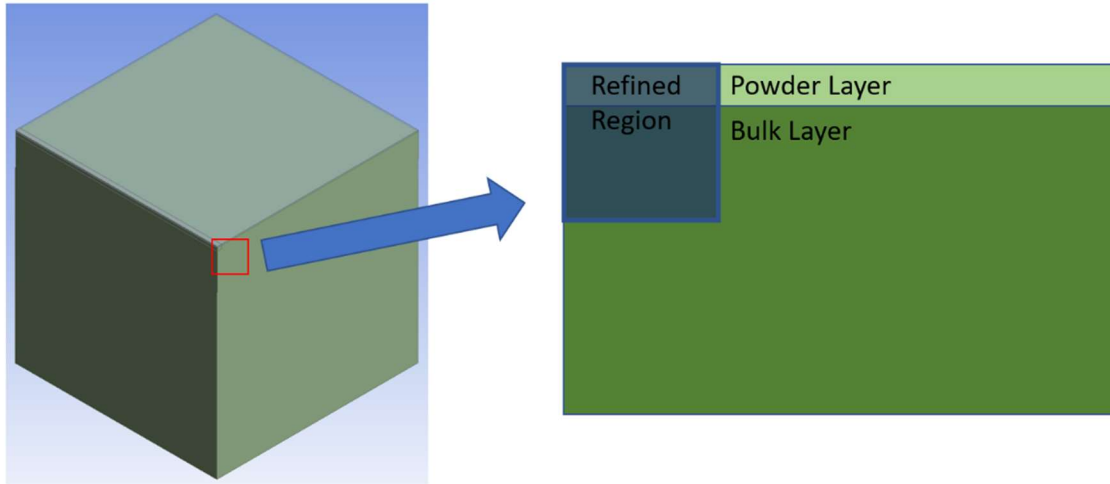


Figure 17: Image of the total geometry (left) and the cross-sectional layout featuring the two layers and the designated refined region (right).

In the refined region, the mesh sizes were kept to the dimension of  $10\ \mu\text{m}$ . Outside the regions, the mesh sizes gradually increase, based on a magnification factor, from the designated mesh size of  $10\ \mu\text{m}$ . The variable size using a tetrahedral mesh is shown in Figure 18. The definition of the mesh was extremely important during construction of the model. An appropriately refined mesh size is required to ensure convergence of the numerical calculation scheme and to accurately depict the change in temperature with location; however, extremely fine mesh dramatically increases the required allocation of memory, number of computations, and time required for completion of the simulations. Therefore, the quality and skewness of these meshes were examined before finalizing the computational model. Not only did this require the identification of a suitable mesh size and magnification but also mesh geometry. Mesh quality is related to a balance of each mesh dimension. For example, a hexahedral mesh would be considered an ideal mesh if all its dimensions are equal like a cube. In contrast, a hexahedral with poor mesh quality could result from having one dimension significantly larger than the others. A skewed mesh could potentially lead to complications in the calculations and divergence. Because of these considerations, the shape of the mesh was chosen to be tetrahedrons. The tetrahedral mesh shape is more computationally expensive due to higher amounts of nodes and cells than other options, such as hexahedrons, but results in inherently increased potential for convergence of the computational scheme. The previously considered hexahedral mesh was found to work with only a smaller total geometry, where the decrease of quality was considered acceptable. While employing the variable mesh size, hexahedral meshes became extremely skewed, up to 100 times the smaller dimension, at large distances from the refined region. These types of problems were more manageable using the tetragonal mesh geometry. Table 3 is a summary of geometric dimensions and mesh settings employed in the model and includes the dimensions representing the geometries for the powder, bulk, and refined regions, as well as notes describing the mesh settings.

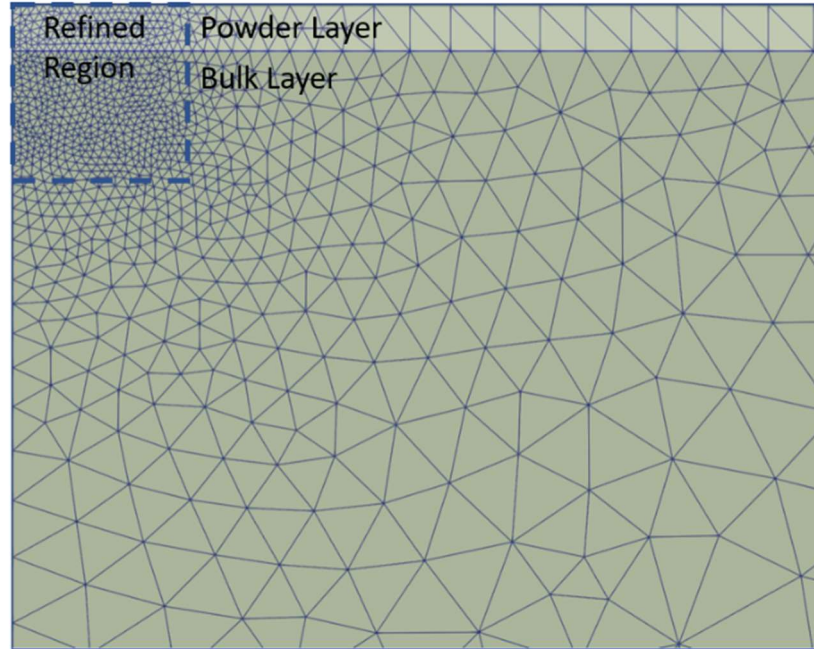


Figure 18: Cross-sectional view of the mesh, with the size increasing in size with distance from the refined region.

However, it should be noted that to operate with this mesh require an advanced ANSYS License since the memory allocation that was required exceeded the student-version limit of 521,000 cells. A developmental mesh was also developed to address this limitation, which had reduced dimensions for the total geometry (2 mm x 1 mm 0.56 mm) but had the same dimensions for the refined region.

Table 3: Summary of geometric dimensions and mesh settings.

<b>Geometry Settings</b>	
<b>Part</b>	<b>Dimension (L x W x H)</b>
<b>Total Geometry</b>	10 mm x 10 mm x 10 mm
<b>Powder Layer</b>	10mm x 10 mm x 0.060 mm
<b>Bulk Layer</b>	10.mm x 10 mm x 9.94 mm
<b>Refined Region</b>	10 mm x 0.2 mm x 0.2 mm
<b>Mesh Settings</b>	
<b>Mesh Shape</b>	Tetrahedron
<b>Mesh Size</b>	10 $\mu$ m

### 3.2.2 Model Configurations

#### Heat Source Shape and Positioning

The volumetric heat source equation is based on McVey et al, which represents the behavior of laser irradiation within a powder layer, as shown in Equation 10. This relationship is based on empirical data fitted to a modified Beer-Lambert Law, which assumes an exponential decay of absorbed laser energy as it scatters within the powder. It also accounts for the spatial distribution of energy presented to the powder layer and may represent a Gaussian distribution or a “top hat”, approximated as uniform energy. The use of a Gaussian distribution in the horizontal or xz plane (xz as defined within the current ANSYS model) with an exponential decay in the vertical or y-axis, which also resembles a decay-function of the heat source listed by Bayat et al [31]. Figure 19 graphically shows a volumetric energy within the powder layer based on a Gaussian distribution and an empirical attenuation coefficient within the McVey relationship as applied in ANSYS Fluent.

$$Q_{heat} = \left[ \frac{\gamma}{1 - e^{-\gamma y_0}} \right] \frac{3\beta P}{\pi r^2} e^{-\frac{3r^2}{r_0^2}} e^{-\gamma y} \quad (10)$$

where the radial distance from the center of the energy source,  $r$ , may be calculated using:

$$r = \sqrt{(x - v * t)^2 + (z)^2}$$

In Equation 10,  $\gamma$  is the attenuation value,  $y_0$  is the thickness of the powder layer,  $\beta$  is the laser absorptivity coefficient,  $r_0$  is the beam radius,  $P$  is the laser power,  $r$  is the radial distance for describing energy, and  $y$  is the depth within the powder where laser energy is being absorbed. The variables  $x$ ,  $y$ , and  $z$  are Cartesian coordinates, and  $v$  is the velocity of the heat source.

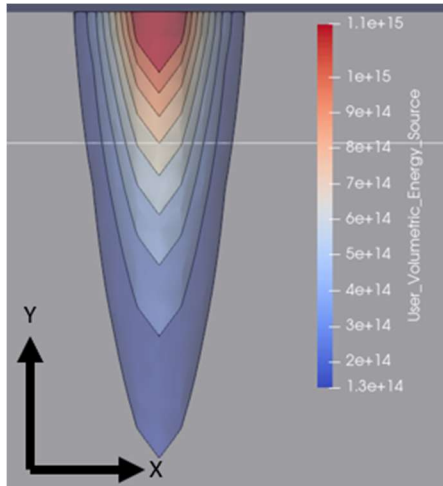


Figure 19: Volumetric energy distribution with the heat source model used (units are in W/m<sup>3</sup>).

The attenuation,  $\gamma$ , is based on the absorption of the laser as it penetrates the powder layer [29]. In this model, the scattering of the laser energy in the powder is represented as the rate of exponential decay in the vertical axis. The value for the attenuation coefficient used during the evaluation was determined by comparing depth of melting based on the physical experiments and virtual simulation results. Several simulations were conducted until the adjusted attenuation value yielded a pool depth within an acceptable error when compared to laboratory measurements for the nominal powder size distribution. To minimize computations during this assessment, only the parameter combinations represented by the Line Numbers of 3, 5 and 7 experimental runs were tested to determine a suitable attenuation value. These parameters, previously mentioned on Table 2, were chosen using a power of 345 W and a velocity of 760 mm/s for Line Number 3 and a power of 225 W and a velocity of 1160 mm/s for Line Number 7 to represent the highest and lowest energy densities of the heat source, respectively, while a power of 285 W and a velocity of 960 mm/s for Line Number 5 represented the nominal parameters. As mentioned in the *Mesh and Construction* section, the powder layer height,  $y_0$ , used in the laboratory experiments and employed during the simulations was 60  $\mu\text{m}$ . The absorption coefficient,  $\beta$ , was given the value of 0.44, based on the work of Lia et al [32].

### Boundary Conditions

Three types of boundary conditions were applied to the model. These were: symmetry along the centerline of the material; heat losses at the irradiated surface; and surface tension effects due to the Marangoni effect also at the irradiated surface. Symmetry was applied to the model on the faces normal to the positive z direction and was imposed to reduce the computational time since only one half of the physical domain is calculated within the model. Surface heat losses include radiation, convection, and evaporation and the equations describing the phenomena are discussed in the next section. The effect of fluid flow within the molten pool due to the Marangoni effect required boundary conditions between two interacting fluids. In the context of laser powder bed fusion, these fluids would be the melt pool and the atmosphere. However, in the case of the flat surface model, the only area where Marangoni effect is driven is at the top surface of the melt pool. Figure 20 shows the arrangement of the boundary conditions with respect to the model geometry.

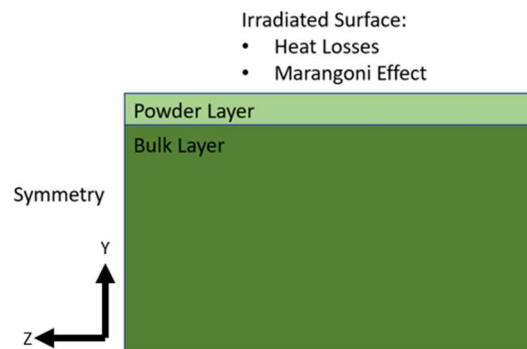


Figure 20: Application of boundary conditions with respect to the geometry.

Heat Losses (Radiative, Convective and Evaporative)

The radiative and convective heat losses are shown in Equation 11 and 12, respectively:

$$q_{rad} = \varepsilon\sigma_s(T^4 - T_{amb}^4) \quad (11)$$

$$q_{conv} = h_c(T - T_{amb}) \quad (12)$$

For both equations,  $T$  is temperature and  $T_{amb}$  is the ambient temperature, set at 300 K. For radiative losses,  $\varepsilon$  is emissivity with a value of 0.36 [33], and  $\sigma_s$  is the Stefan-Boltzmann constant. For convection,  $h_c$  is the convection heat transfer coefficient, which was applied as 80 (W/m<sup>2</sup>\*K) based on the work of Cao and Yuan[33].

The evaporation flux is also based on Cao and Yuan. [33], which is shown in Equation 13:

$$q_{vap} = \Delta H_{vap}(p_{vap} - p_{amb}) \sqrt{\frac{m}{2\pi k_b T}} \quad (13)$$

The evaporation calculation can be determined based upon the enthalpy of vaporization,  $\Delta H_{vap}$ , and the mass flux, which may be defined by the difference in vapor pressure,  $p_{vap}$ , and the ambient pressure,  $p_{amb}$ . The right term in Equation 13 describes the volume of material participating in the evaporation process, where under the square root term, consists of the molecular mass,  $m$ , Boltzmann's constant,  $k_b$ , and the temperature,  $T$ .

Cao and Yuan, employed two equations, shown below, to describe pressure of the gas or vapor during the evaporative process. The first vaporization pressure is described as the vaporization pressure between transition temperatures,  $p_{vap,transition}$ , and pressure occurring during the terminal phase of vaporization,  $p_{vap}$ . A polynomial that was constructed to create a smooth transition between the ambient pressure,  $p_{amb}$ , defined by Equation 15, and the second vaporization pressure, is shown in Equation 14. In the vaporization equation,  $\beta_r$  is the recombination rate, valued at 0.2, and  $p_0$  is the ambient pressure, which was defined as 101,325 Pa. The range of the transition temperatures utilized for the IN718 material was between  $T_{left}$ , 2935 K, and  $T_{right}$ , 3244 K, and the relationship used to smooth the transition is shown graphically in Figure 21. It must be noted that these equations represent heat losses due to evaporation as a flux at the top surface and not mass loss.

$$p_{vap,transition} = (3.376 \times 10^{-3}T^3) + (29.445T^2) + (85590.172T) + (8.282 \times 10^7) \quad (14)$$

$$p_{amb} = \frac{1 + \beta_r}{2} p_0 \quad (15)$$

$$p_{vap} = \frac{1 + \beta_r}{2} p_0 \exp \left[ \frac{m\Delta H_{vap}}{k_b} \left( \frac{1}{T_v} - \frac{1}{T} \right) \right] \quad (16)$$

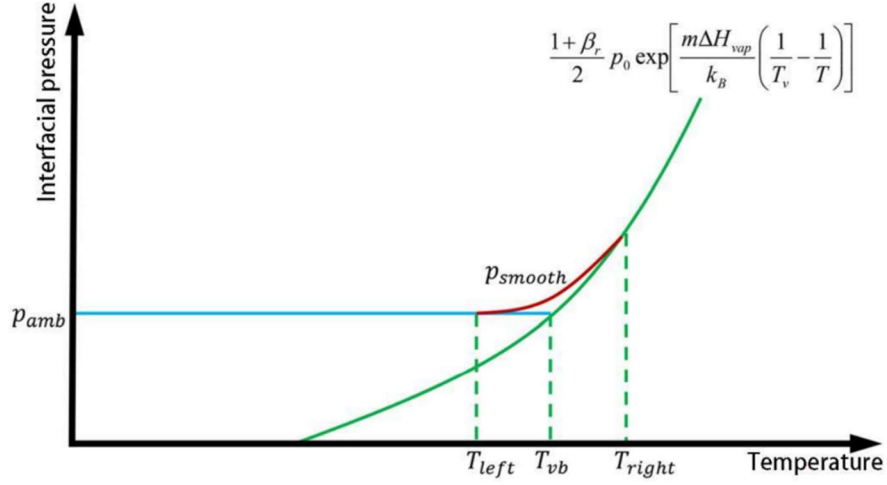


Figure 21: Pressure vs temperature model with pressure smoothing equation used by Cao and Yuan[33].

### Marangoni Stress

To allow for more accurate representation of fluid flow behavior, the Marangoni effect, which is dictated by the surface tension gradient due to thermal differences within the liquid pool, must be enabled during the simulation. Otherwise, the model will only consider pure conduction behavior within the liquid causing errors in temperature and nonrealistic melt pool geometries. Depending on the material, a positive surface tension gradient would result in an outward flow in the melt pool and would result in a melt pool geometry that is wide and shallow. In contrast, material having a negative surface tension gradient as a function of temperature, such as IN718, would result in Marangoni flow from the pool edges to the center and would be indicative of a narrower and deeper melt pool, as shown in Figure 22. Both of these conditions are illustrated in Figure 22. The figure depicts the melt pool geometry due to Marangoni flow based on the surface tension gradient for a material being negative or positive with temperature. In both cases, temperatures at the center of the pool just below the heat source is assumed to be higher than temperatures at the pool edge. Utilizing the internal capabilities of ANSYS Fluent to describe flow based on conservation of momentum, Marangoni flow was incorporated into the model using a value of  $-3.01 * 10^{-4} \text{ N}/(\text{m} * \text{K})$  for the surface tension gradient or Marangoni coefficient. This value was based on the earlier works of Queva et al and Temmler et al [28, 29].

In ANSYS Fluent, the Marangoni effect is applied to the irradiated boundary, shown in Figure 20, as shear stress. The value of this shear stress is deduced as:

$$\tau = \frac{d\sigma}{dT} \nabla_s T \quad (17)$$

where  $\frac{d\sigma}{dT}$  is the surface tension gradient and  $\nabla_s T$  is the surface gradient.

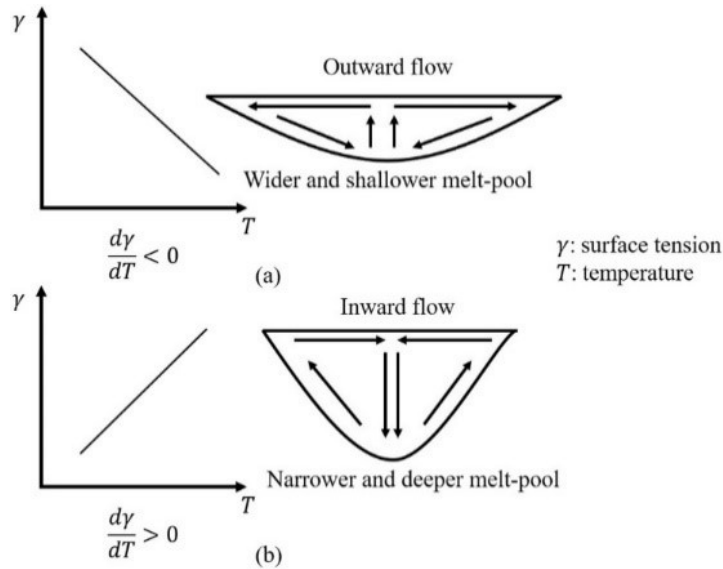


Figure 22: Marangoni effect with negative and positive surface tension gradients [36].

### 3.2.3 Representation of Material Behavior

The thermophysical properties of density, specific heat, and thermal conductivity were given temperature-dependent behavior to increase the fidelity of the model. Because IN718 material has been widely reported in the literature, its properties were well documented. This study took advantage of this by creating statistical-based regression relationships representing the property as a function of temperature based on compiled values obtained within the literature for IN718. For each thermophysical property, a regression relationship would be developed for temperatures representing the solid and liquid states, as well as for the two-phase region signifying the mushy zone liquid states. When the temperature was shared between two states, such as the solidus temperature representing the terminal point of the solid, as well as the liquidus representing the initial point of the liquid, the regression equations describing each state were forced to convergence to a common point at that temperature. This approach provided continuity during the computation and avoided unnecessary divergence problems.

Additionally, in the case of thermal conductivity, the path dependency behavior was also considered due to transformations of the powder melting to form a liquid, beginning at the solidus temperature, and forming the complete liquid at the liquidus temperature, and solidification upon cooling from elevated temperatures, through the two-phase region between the liquidus and solidus temperatures, and further cooling to approach ambient temperatures. This resulted in thermal conductivity and absorptivity changing significantly as powder is melted to form a liquid and subsequently solidified as a solid. The thermal conductivity of the powder is significantly lower than the conductivity of the bulk, solid material due to transmission of heat being impeded from the limited contact between powder particles. Thermal conductivity increases after consolidation through melting and solidification.

## Density

For density, three linear equations were formulated to represent the solid, mushy zone, and liquid states. Determining values for properties of the solid were significantly easier than for those of the liquid. Properties describing the mushy zone were the most difficult to obtain, since little information under this condition for IN718 was available in the literature. Because of the lack of data for material in this condition, an interpolation line was used to define the density between the solidus and liquidus temperatures. As mentioned earlier, the two relationships were developed to force convergence at the solidus and liquidus temperatures. Table 4 list the equations used for the density in the solid, mushy zone, and liquid state, which are also visualized in Figure 23. The information in this figure was compiled from Mills [37], Cao and Yuan [33], Pottlacher et al [38], Agazhanov et al [39], and Abdullaev et al [40].

Table 4: Temperature-dependent density equations.

State (Temperature Range)	Equation
Solid ( $T < 1533\text{K}$ )	$\rho = 8348.36973 - 0.48898T$
Mushy Zone ( $1533 < T < 1610\text{K}$ )	$\rho = 10307.37 - 1.7668674025974T$
Liquid ( $T > 1610\text{K}$ )	$\rho = 8771.1616 - 0.8127T$

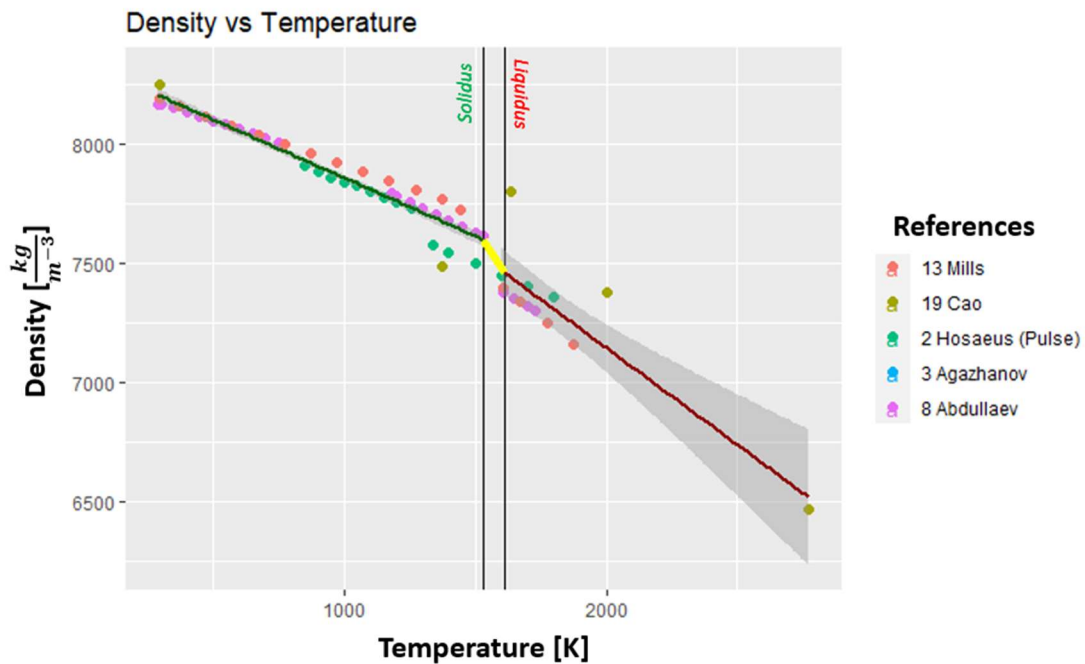


Figure 23: Compilation of density values in literature and linear regression lines listed in Table 5 [33, 37–40].

### *Specific Heat Capacity*

During the compilation of data for representing specific heat for IN718, it was quickly observed that the data did not follow a linear relationship throughout the solid-state temperatures. The data was observed to have had a linear relationship until around 800 K with a polynomial relationship describing the data until the liquidus temperature (1610 K). In the case of specific heat for this alloy, the polynomial was also used to describe the specific heat from the solid state through the two-phase region to the liquidus temperature. This approach was utilized because of the meager data available within the literature for this region. Therefore, two piecewise regression relationships were constructed to describe the solid state: a linear relationship from room temperature to around 800 K followed by a third-degree polynomial from around 800 K to the liquidus temperature of 1610 K. The regressions were first performed using  $c_p$  values below and above 800 K. Brooks also noticed that around 800 K, there was a shift in the relationship between  $c_p$  and temperature [41]. The linear relationship from 298 K to approximately 800 K is shown below in Equation 18:

$$c_p = 393.6 + 0.1631T \quad (18)$$

The polynomial for the second relationship representing the solid state was based on the equation employed by the National Institute of Standards and Technology (NIST) derived using their thermochemical tables [42]. After examining the data, a third-degree polynomial was considered the best fit and resulted in the highest  $R^2$  value of 77.6%. The third-degree polynomial used to describe the specific heat in this region is shown below in Equation 19:

$$c_p = -2901 + 8.82T - (7.267 \times 10^{-3}T^2) + (1.983 \times 10^{-6} T^3) \quad (19)$$

To create a smoother transition between the two equations, the intercept value for the lower temperature, linear relationship and the third-order polynomial describing specific heat at the higher temperatures was determined to be 812.86K. For the specific heat of the liquid, the value was calculated from Equation 19 at the liquidus temperature (1610K) and kept constant for temperatures above the liquidus. This approach was utilized because of the extremely limited data available at high temperatures within the liquid. The complete specific heat-temperature relationship is shown in Figure 24, which includes values from the intermediate temperature readings between 400 and 1250 K by Basak et al [43], and values from pulse-heating and differential scanning calorimetry (DSC) methods from Pottlacher et al (Hoeasus) [38], the equation from Tanda and Misale [44], and data points from Agazhanov et al [39], Brooks et al [41], Lee and Zhang [45], Mills [37], Pawell and Williams [46] and Valencia and Queded [47].

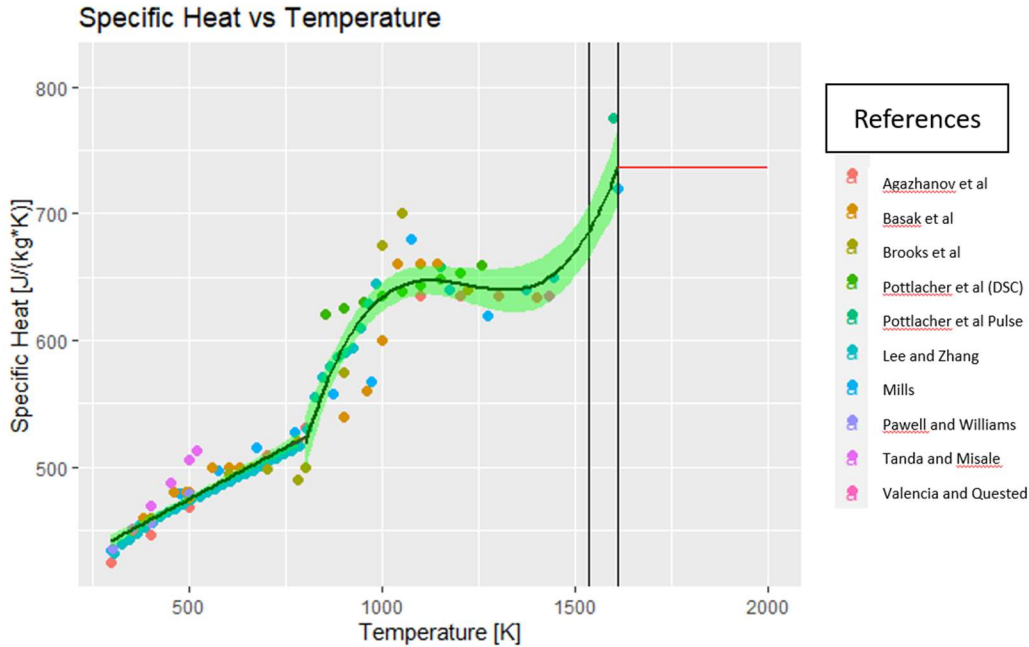


Figure 24: Compilation of specific heat capacity literature values with the regression equations [38,39,41,43,44,46-48].

### *Thermal Conductivity*

Similar to the relationships discussed above to describe density as a function of temperature for the IN718 alloy, the relationships for thermal conductivity were composed of linear equations representing the solid, mushy zone, and liquid states. However, in the case of powder bed fusion simulations, one must consider whether the solid material is in powder or bulk form. The thermal conductivity of the former is significantly smaller than the latter due to the limited thermal diffusion through contact between powder particles. In this study, the effective thermal conductivity of the IN718 in powder form was assumed to be 5% of the bulk material. The current value to describe the powder is similar to studies by Hedreen that used an effective thermal conductivity value of 7.5% of the bulk material [49] and Zhang, S. et al which concluded that the thermal conductivity ratio between powder to bulk solid could range from 3.4% to 6.9% [6]. As with the development of the regression lines for density, the value for thermal conductivities between both solid forms (powder and bulk) and the liquid are performed through interpolation of the thermal conductivities at the liquidus and solidus temperatures. Table 5 list the equations describing thermal conductivity for all states, including both solid forms and transitions from powder and bulk solids to the liquid state.

Table 5: Thermal conductivity equations.

<b>State (Temperature Range)</b>	<b>Thermal Conductivity Equation</b>
Bulk Solid (T<1533 K)	$k = 5.564 + 0.016T$
Powder Solid (298 -1533 K)	$k = (5.564 + 0.016T) * 0.05$
Liquid-to-Bulk (1533 -1610 K)	$k = 46.753 - 0.011T$
Powder-to-Liquid (1533-1610 K)	$k = -557.506 + 0.365T$
Liquid (T>1610 K)	$k = 29.6$

As stated earlier, path dependency for describing the thermal conductivity must also be considered. During cooling from an elevated temperature that results in resolidification, the thermal conductivity of the melted powder does not revert to the conductivity of the solid in powder form. Instead, upon cooling the melted powder would exhibit properties of a bulk solid since the powder particles would have consolidated during melting. To implement this behavior in ANSYS Fluent, User-Defined Functions were utilized to create conditional statements that identified powder that had been resolidified after melting. The flowchart of path dependency of thermal conductivity is illustrated in Figure 25. In the diagram the inputs of the time step, location, temperature, and current thermal conductivity of the node is used as conditional statements. The time step conditional statement is used to apply initial conditions. Conditional statements based on location determines whether the node is in powder or bulk layers. The temperature conditions are used to verify if the state of the node represents the solid, mushy, or liquid form, and finally, the thermal conductivity conditional statements allow for identification of nodes that have been solidified. Figure 26 graphically depicts the thermal conductivity of the powder, bulk solid, and liquid and a function of temperature and path. The graphical relationships within the figure represent data values or regression fits of the data (based on regression equations defined in Table 54) based on the literature and includes data from McElroy et al [50], Mills [37], Pawell and Williams [46], Agazhanov et al [39], Valencia and Queded [47], Raghavan [51] and Rai et al [52].

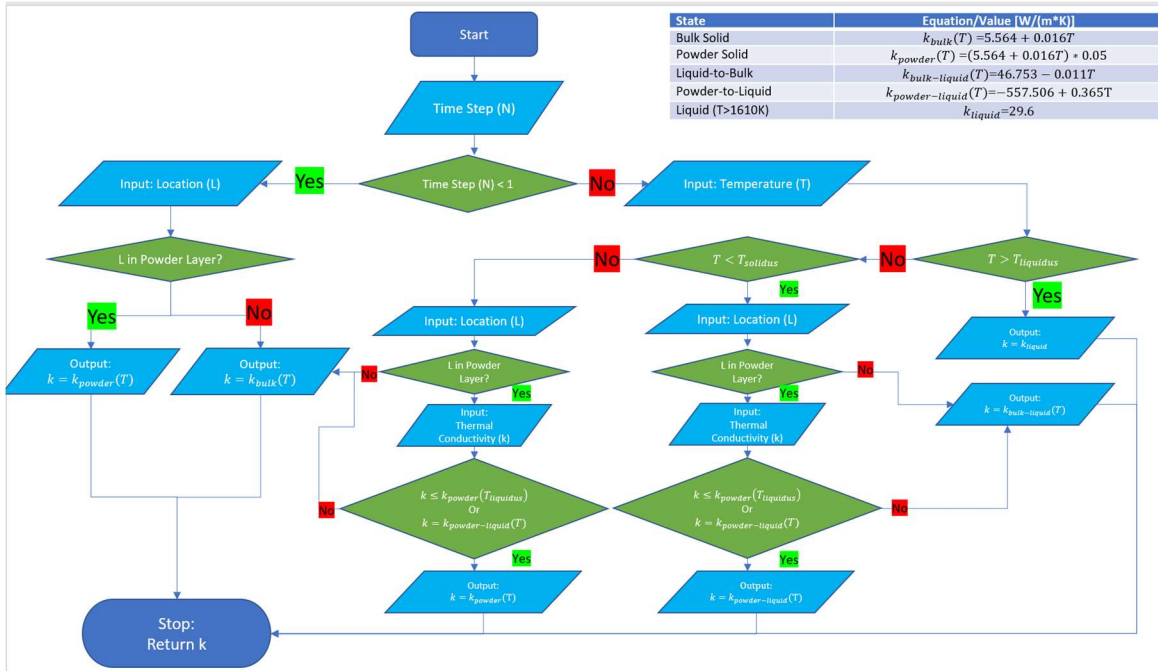


Figure 25: Flowchart for path-dependency of thermal conductivity

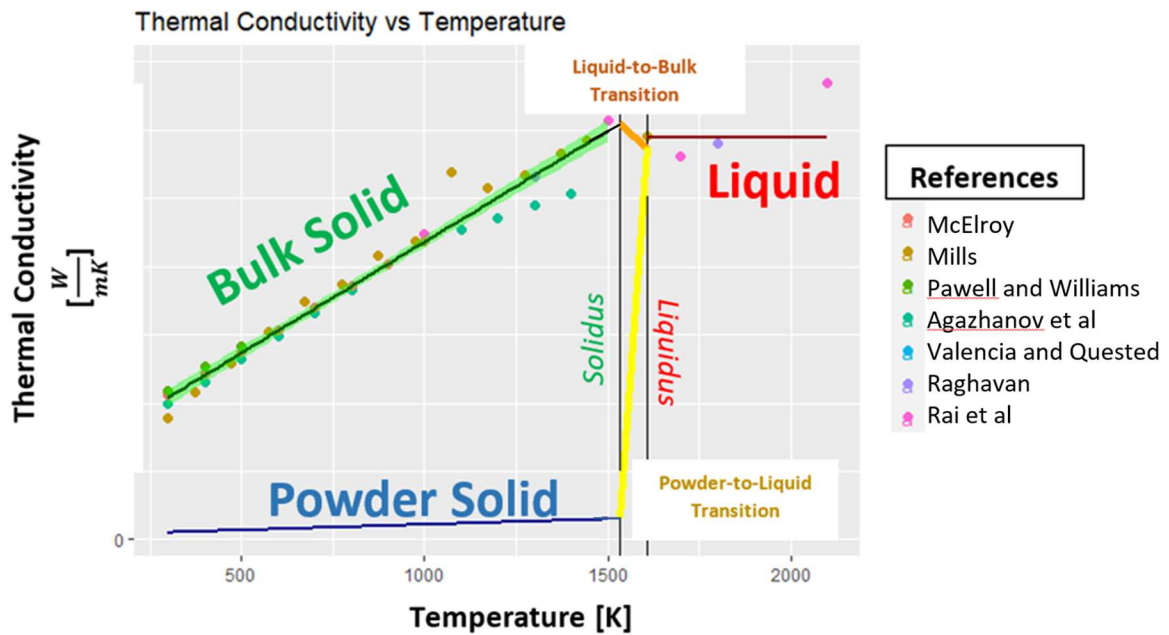


Figure 26: Compilation of thermal conductivity literature and regression lines [37,39,46,47,50-52].

### 3.2.4 Simulation Settings and Summary

All settings for performing the virtual simulations using the model in ANSYS Fluent are shown in Table 6. The table includes material properties, boundary conditions, and various ANSYS and computational settings, and many of these parameters have been discussed previously. For material properties, constants such as viscosity, heat of fusion, surface tension gradient, and the solidus and liquidus temperatures are listed. The solution limits for temperature were also defined and was adjusted to be between 295K for the minimum temperature and 3500K, which is 500K above the vaporization, for maximum allowable temperature. Before confirming this adjustment, the temperature profiles with the 3500K temperature limit and the ANSYS Fluent's default temperature limit of 5000K were compared. As demonstrated by Figure 27, the shape of the isotherm curves for the liquidus and vaporization curves in both instances appeared very similar. For calculation setting, a total time of 300  $\mu$ s was chosen. This time was considered sufficient for the melt pool to reach quasi-steady state conditions in which the melt pool depth and width remains constant at future times. This was confirmed by tracking the temperature directly under the heat source over time and indicated that the maximum temperature at the pool surface remained constant at that time shown in Figures 28 and 29.

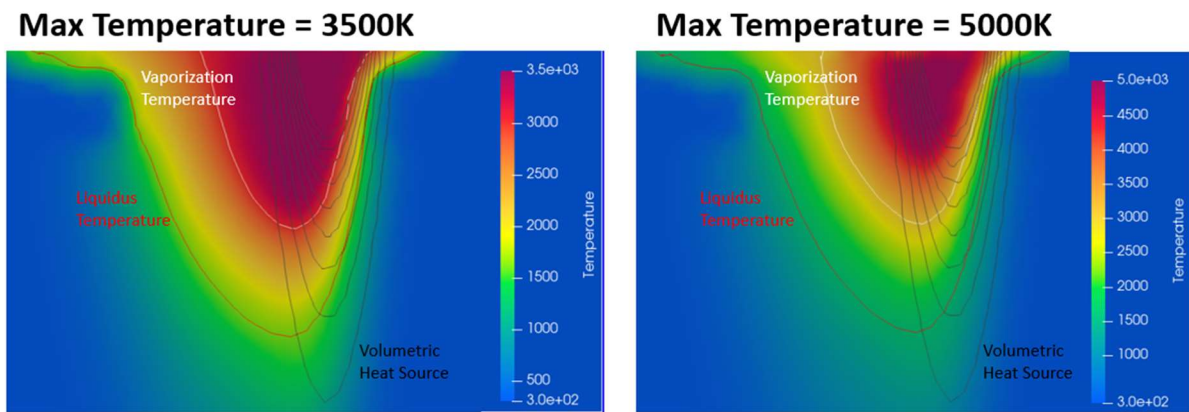


Figure 27: Comparison of temperature profiles between adjusted (3500K) and default (5000K) temperature limits



Figure 28: Verification of quasi-steady state condition for melt pool depth

Table 6: Summary of settings for the IN718 Model.

<b>Model Settings Enabled</b>	
Viscous Laminar	
Energy	
Solidification and Melting	
<b>Material Properties</b>	
Density [kg/m <sup>3</sup> ]	Table 4
Specific Heat [J/(kg*K)]	$c_p = 393.6 + 0.1631T$ (T<812.86K)
	$c_p = -2901 + 8.82T - (7.267E - 3 * T^2) + (1.983E - 6 * T^3)$ (812.86-1610K)
	738.026 (T>1610K)
Thermal Conductivity	User Define Function based on Table 5
Viscosity [kg/(m*s)]	0.0053 [53]
Heat of Fusion [J/kg]	219,000 [33]
Solidus Temperature [K]	1533
Liquidus Temperature [K]	1609
Marangoni coefficient/Surface Tension Gradient [N/(m*K)]	-0.000301 [34], [35]
<b>Solution Method</b>	
Pressure Velocity Coupling	SIMPLE
Spatial Discretization	
Gradient	Least Square Cell Based
Pressure	Second Order
Momentum	Second Order Upwind
Energy	Second Order Upwind
<b>Boundary Condition</b>	
Condition	Location
Heat Losses (Convection, Radiation and Evaporation)	Irradiated Surface (Normal to Y axis)
Marangoni Effect	Irradiated Surface (Normal to Y axis)
Symmetry	Plane Normal to Z axis
<b>Cell Zone Conditions</b>	
Apply heat source on both powder and bulk layers	
<b>Equations Enabled</b>	
Flow	
Energy	
<b>Relaxation Factors</b>	
Momentum	0.5
Density	1
Body Forces	1
Momentum	0.5
Liquid Fraction Update	0.9
Energy	0.975
<b>Solution Limits</b>	
Minimum Temperature [K]	295
Maximum Temperature [K]	3500
<b>Calculation Settings</b>	
Number of Time Steps	300
Time Step Size [s]	1e-06
Max Iterations/ Time Step	20

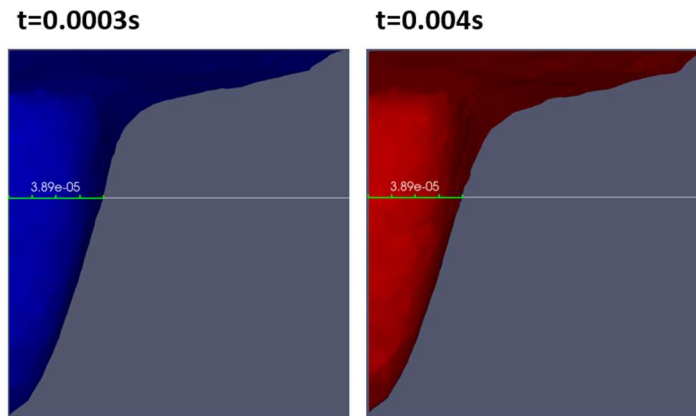


Figure 29: Verification of quasi-steady state condition for bead width

### 3.3 Database Creation of Properties for Niobium Alloy C103

There was also interest in utilizing the model to simulate the powder bed fusion process using a refractory metal, such as the niobium-based alloy, C103. To accomplish this, properties for C103 used for describing the various phenomena discussed above would be necessary. Properties of interest for C103 alloy included: solidus and liquidus temperatures, latent heat of fusion and vaporization, viscosity, surface tension gradient (Marangoni coefficient), and most importantly, the thermophysical properties of density, specific heat, and thermal conductivity. These properties would be required for use as inputs for conducting virtual simulations in ANSYS Fluent at the same level of fidelity of that developed for the prior IN718 model. Although a scarce amount of information and data was observed to be available in the open literature regarding this alloy, a relatively extensive survey provided a reasonable degree of data for use in virtual simulations. Table 7 list the properties for C103 alloy that would be of interest for conducting the virtual experiments with that alloy

Table 7: Properties of interest to be compiled formatted as: property, column name, [units]

Constants	Temperature Dependent
<ul style="list-style-type: none"> <li>• Composition, <i>Comp.</i> [%]</li> <li>• Molar Mass, <i>M</i> [kg/mol]</li> <li>• Molecular Mass, <i>M_Na</i> [kg]</li> <li>• Solidus Temperature [K]</li> <li>• Liquidus Temperature [K]</li> <li>• Vaporization Temperature [K]</li> <li>• Heat of Fusion, <i>H_fus</i> [J/kg/K]</li> <li>• Heat of Evaporation, <i>H_vap</i> [J/kg/K]</li> <li>• Viscosity, <i>mu</i> [Pa*s]</li> <li>• Surface Tension Gradient, <i>deltagamma</i> [N/m/K]</li> </ul>	<ul style="list-style-type: none"> <li>• Density, <i>rho</i> [kg/m<sup>3</sup>]</li> <li>• Specific Heat Capacity, <i>cp</i> [J/kg/K]</li> <li>• Thermal Conductivity, <i>k</i> [W/m/K]</li> <li>• Surface Tension, <i>gamma</i> [N/m]</li> </ul>

## Chapter 4: Results and Discussion

The outcomes of processing and analyses of the characterization data resulting from the physical experiments are discussed in Section 4.1. Meanwhile, Section 4.2 discusses the result of the melt pool geometries obtained through virtual experimentation using the physics-based model. Finally, the compilation of thermophysical properties for C103 and its elemental components, along with subsequent simulations are discussed in Section 4.3

### 4.1 Data Processing of Experimental Data

The characterization data from metallography of single-track experiments were analyzed using statistical methods to potentially discover any relationships between the primary process parameters, laser power and scan speed, and powder size distribution on melt pool geometry. The statistical analysis initially examined the dataset as a whole. This is then followed by a more thorough approach by examining the subsets sorted by powder size distribution and their line numbers.

#### 4.1.1 Initial Analyses

The initial box plot for both responses are shown in Figure 30, which shows the outliers with respect to the median and inter-quartile ranges. Based on this figure, the melt pool depth only has one outlier, the point representing a 195  $\mu\text{m}$  depth, which had only a 2  $\mu\text{m}$  difference from the maximum of the box plot depth value of 193  $\mu\text{m}$ . Based on this observation, the outlier was retained for further analysis. Interestingly, the extrema of the melt pool depth measurement went from 0  $\mu\text{m}$  to 200  $\mu\text{m}$ . As expected, the parameters for these extremes were 225 W of power and travel speed of 1160 mm/s for the minimum depth and 345 W and 760 mm/s for the maximum depth. Further discussions will also employ “P” to represent power and “V” to describe scan speed of the heat source.

In terms of width, the range was much shorter with the minimum value of 97  $\mu\text{m}$  and maximum of 181  $\mu\text{m}$  for depth of penetration. As shown in Figure 30, the bead width data contained more outliers in comparison to the box plot. All the of the outlier data points are from the fine powder distribution, representing the powder diameter having a range between 10 and 40  $\mu\text{m}$ . The histograms in Figure 31 showed more details in the distribution of the measurements of melt pool depth and bead width, respectively.

After removing the outliers shown in Figure 30, the histograms of for both melt pool depth and bead width were created and are shown in Figure 31. Both histograms were asymmetrical and similarly shaped but mirrored in skewness. Evaluating the energy density in Table 2 showed that its distribution was not symmetrical, with line numbers 3 (P=225 W and V=760 mm/s), 5 (P=285 W and V=960 mm/s), and 9 (P=345 W and V=1160 mm/s) all have the same energy densities of approximately 3.7 J/m<sup>2</sup>. This causes the histogram distribution to lean towards the medians of 87 $\mu\text{m}$  and 141 $\mu\text{m}$  for melt pool depth and bead width, respectively.

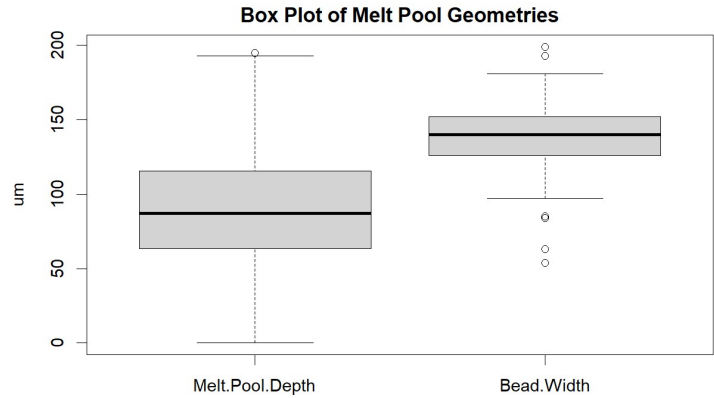


Figure 30: Initial boxplot of melt pool depth and bead width showing the outliers.

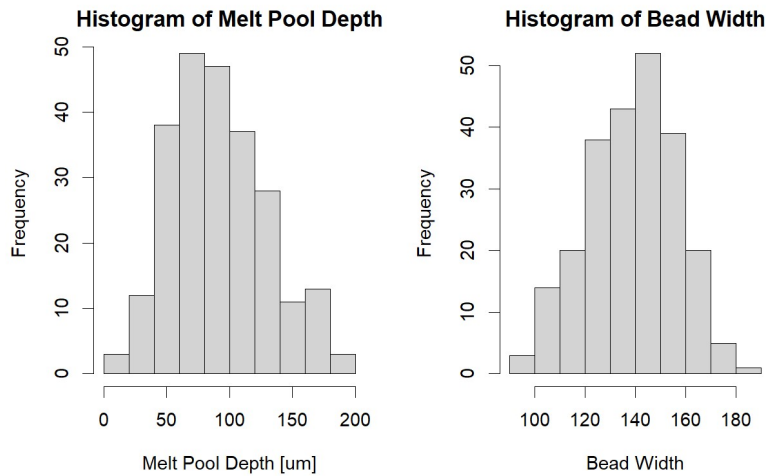


Figure 31: Initial histogram of melt pool depth and bead width responses.

Alongside analysis of variance (ANOVA) of the data, a linear regression equation was created with laser power, scan speed, and powder size to predict bead width and depth. Additionally, for each independent variable (power, speed, and powder diameter), ANOVA was utilized to determine the statistical significance. Another useful output from ANOVA was the coefficient of determination,  $R^2$ , which was used to determine how well the regression equation fit the data. The ANOVA results are summarized in Tables 8 and 9.

The ANOVA analysis for melt pool depth in response to changes in P, V, and  $D_{50}$  indicated that laser power had a strong positive relationship with response, having a coefficient of 0.545. Scan speed, however, had a negative response and weaker relationship compared to power with a coefficient of -0.129. Interestingly, powder size had the largest coefficient value of 0.875. All three of these predictors were considered statistically significant. With these three predictors, the resulting regression line had an  $R^2$  value of 0.813, which was indicative of a rather strong prediction for melt pool depth.

Table 8: Initial analysis of variance results and linear regression for melt pool depth.

<b>Melt Pool Depth</b>		
<b>Predictor</b>	<b>Coefficient</b>	<b>Statistically Significant</b>
Intercept	33.279	Yes
Laser Powder	0.545	Yes
Scan Speed	-0.129	Yes
Powder Size	0.875	Yes
R <sup>2</sup>		0.813

In the case of bead width, the coefficients for each predictor were of lower magnitude compared to that of melt pool depth. As with melt pool depth, linear regression analysis of bead width provided a positive relationship with laser power, while scan speed showed a negative influence with the coefficient being of lower magnitude. The linear regression analysis showed a large difference between the coefficient of powder size distribution for melt pool depth and bead width. This predictor was considered statistically insignificant with the lowest coefficient. Finally, the fitting of the bead width from linear regression resulted in a lower R<sup>2</sup> value of 0.643, which indicated a poor quality for prediction for width as opposed to the relationship for melt pool depth.

Table 9: Initial analysis of variance and linear regression results for bead width.

<b>Bead Width</b>		
<b>Predictor</b>	<b>Coefficient</b>	<b>Statistically Significant</b>
Intercept	139.783	Yes
Laser Powder	0.207	Yes
Scan Speed	-0.0622	Yes
Powder Size	0.00592	No
R <sup>2</sup>		0.623

Based on the initial analysis of the experimental data, a few patterns were recognized. Based on the box plot, the melt pool depth measurements would have wider range compared to the bead width, spanning from 0  $\mu\text{m}$  to 195  $\mu\text{m}$ . Whereas, bead width ranged from 97  $\mu\text{m}$  to 181  $\mu\text{m}$ . The histogram showed that the distribution of responses was skewed towards the 50 to 100  $\mu\text{m}$  for melt pool depth and 140 to 160  $\mu\text{m}$  for bead width. Initial ANOVA and linear regressions analyses showed that both primary process parameters, laser power and scan speed, were statistically significant to bead width and melt pool depth responses. However, powder size distribution was only considered statistically significant for melt pool depth but not for bead width. To further confirm these initial observations, more thorough exploratory data analyses (EDA) was performed. Boxplots were again constructed for displaying melt pool depth and bead width, but instead of utilizing the whole dataset, the data was examined using each subset based on

the three powder size distributions. This was pursued due to the initial results from linear regression and ANOVA indicating statistical significance of powder size distribution to the melt pool depth.

4.1.2 Correlation Analysis

The results of the correlation matrices are visually organized in Figure 32, while Table 10 charts the Pearson correlation coefficient (PCC) values. Similar to the initial analyses, the PCCs of the primary process parameters of laser power and scan speed had positive and negative relationships, respectively, with melt pool depth and bead width responses. However, in terms of magnitudes, the PCC for laser power and scan speed for bead width were closer to each other with values of 0.55 and -0.56, respectively. Meanwhile, the magnitudes for the correlation coefficients between these primary process parameters with respect to melt pool depth were further apart, being 0.69 and -0.55, respectively. In terms of powder size, the correlation with melt pool depth was much stronger than with bead width, with a coefficient value for the former that is at least eight times larger than the latter. This corroborates the initial ANOVA results that powder size distribution was statistically significant only for melt pool depth but not for bead width.

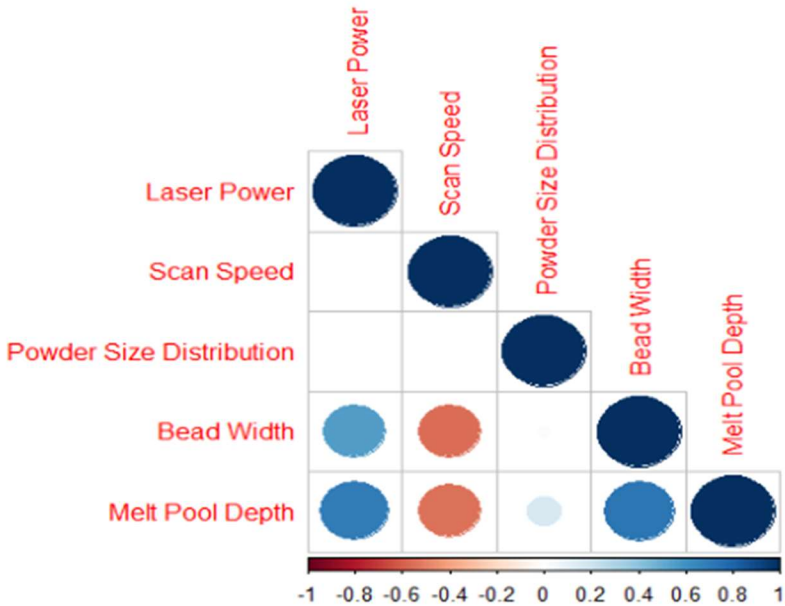


Figure 32: Correlation matrices between independent and dependent variables.

Table 10: Pearson correlation coefficient values between independent and dependent variables.

Pearson Correlation Coefficient (PCC) Results					
	Laser Power	Scan Speed	Powder Size Distribution	Bead Width	Melt Pool Depth
Bead Width	0.55	-0.56	0.02	1	0.72
Melt Pool Depth	0.69	-0.55	0.17	0.72	1

### 4.1.3 Boxplots, Dot plots and Histograms

Revising the EDA with boxplots and dot plots, the dataset set was split into three subsets based on powder size distribution. For each of these subsets, the data would be further split into groups based on the line number, which represents a particular combination of the primary process parameters listed in Table 2. The resulting melt pool depth boxplots for each subsets are shown in Figure 33, which also shows a total of 12 statistical outliers. Of all these outliers, eight were from the coarse powder ( $D_{10}/D_{90} = 25/55 \mu\text{m}$ ), three from the nominal sized powder ( $D_{10}/D_{90} = 15/45 \mu\text{m}$ ), and only one for the fine powder size ( $D_{10}/D_{90} = 10/40 \mu\text{m}$ ). Though the fine sized powder had only one outlier, visual examination of Figure 33 showed that the interquartile range (IQR) for each group was much larger than those compared to the other powder size distributions. In contrast, while the coarse powder size contains more statistical outliers, the IQR of each group were more compact. As mentioned in Section 3.1.3, a large IQR implies a large variance. To obtain a better visualization of the distribution of melt pool depth measurements for each group, the boxplots were converted into dot plots.

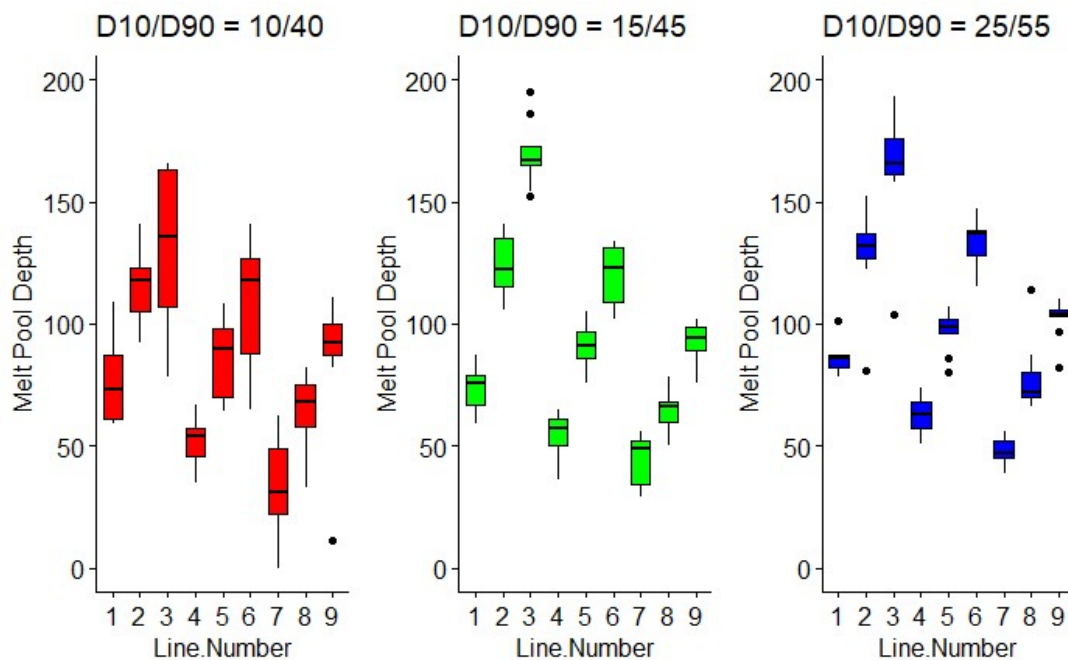


Figure 33: Boxplot of melt pool depth across different powder size distribution.

Before the conversion of the boxplots into dot plots, the outliers shown in the prior graph were first removed. The resulting dot plots are shown in

Figure 34. The previously mentioned assumptions in the boxplots were corroborated based on the scattering of samples for each group. For the coarse powder size, the data points tended to be in a tighter cluster and very close to their respective medians, especially in the case of Line Numbers 1 ( $P=225 \text{ W}$  and

V=760 mm/s), 6 (P=345 W and V=960 mm/s), and 9 (P=345 W and V=1160 mm/s). With the finer powder size, the expectation of large variance, and thus deviation from the median due to the large IQR, were validated.

Prior to examining the boxplots and dot plots for bead width, the boxplots in Figure 33 were rearranged based on their surface energy density values from Table 2. This was conducted to evaluate possible relationship between variance and surface energy density. The arranged boxplot is shown in Figure 35. Examination of Figure 35 under this presentation showed no discernable patterns between energy density and IQR.

The same procedures were also conducted with bead width and similar results also appeared; although, to a more limited extent. As shown in both Figures 36 and 37, the fine powder size tended to have somewhat larger IQR. However, the overall distribution of bead width measurements between each groups tended to be more compact than the measurements of melt pool depth.

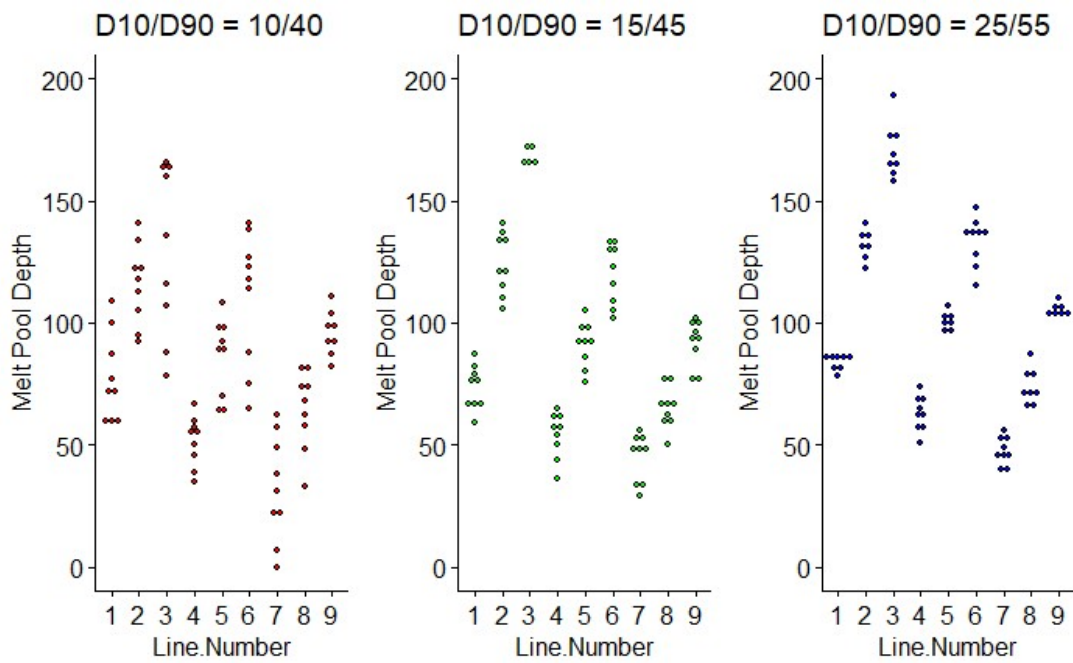


Figure 34: Dot plot of melt pool depth across different powder size distribution with outliers omitted.

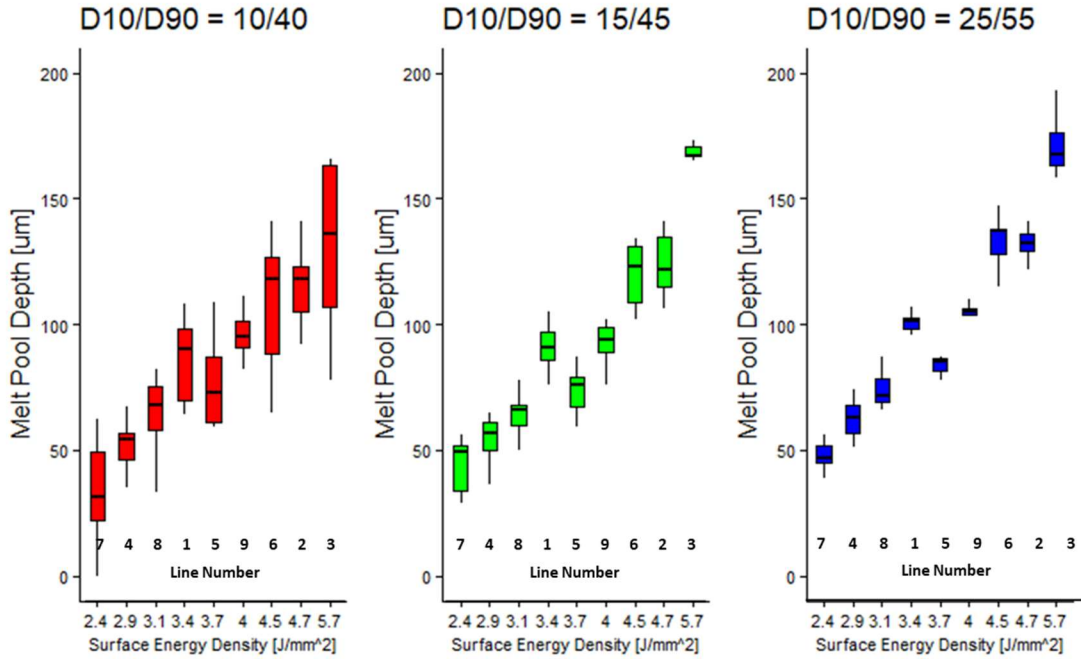


Figure 35: Boxplot arranged by energy density with corresponding line number designation.

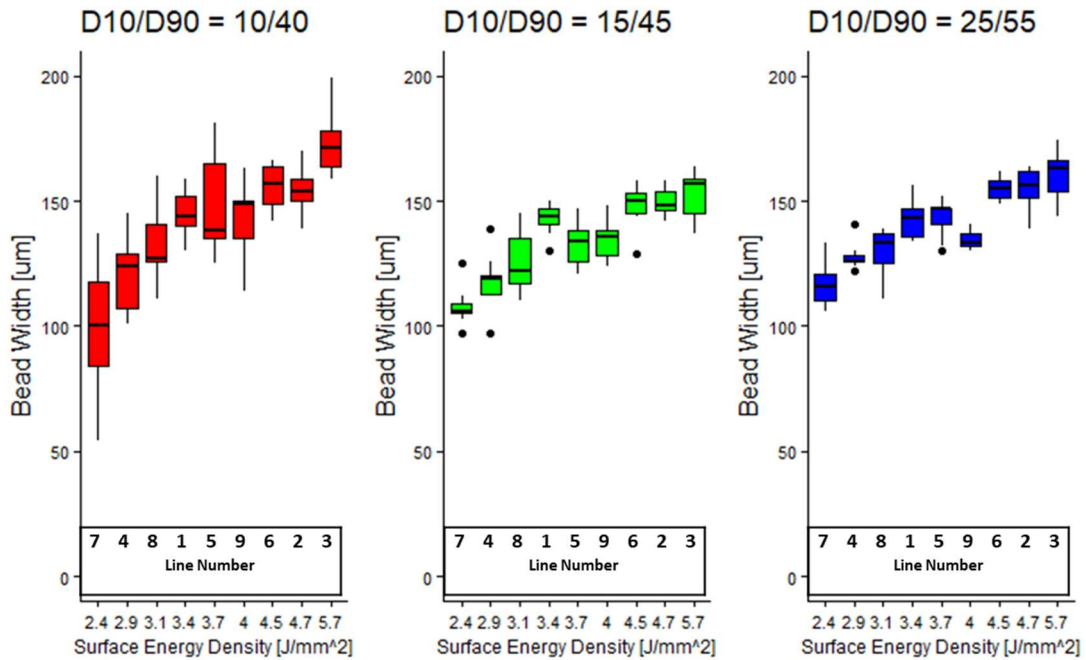


Figure 36: Boxplots of bead width arranged in terms of energy density including outliers.

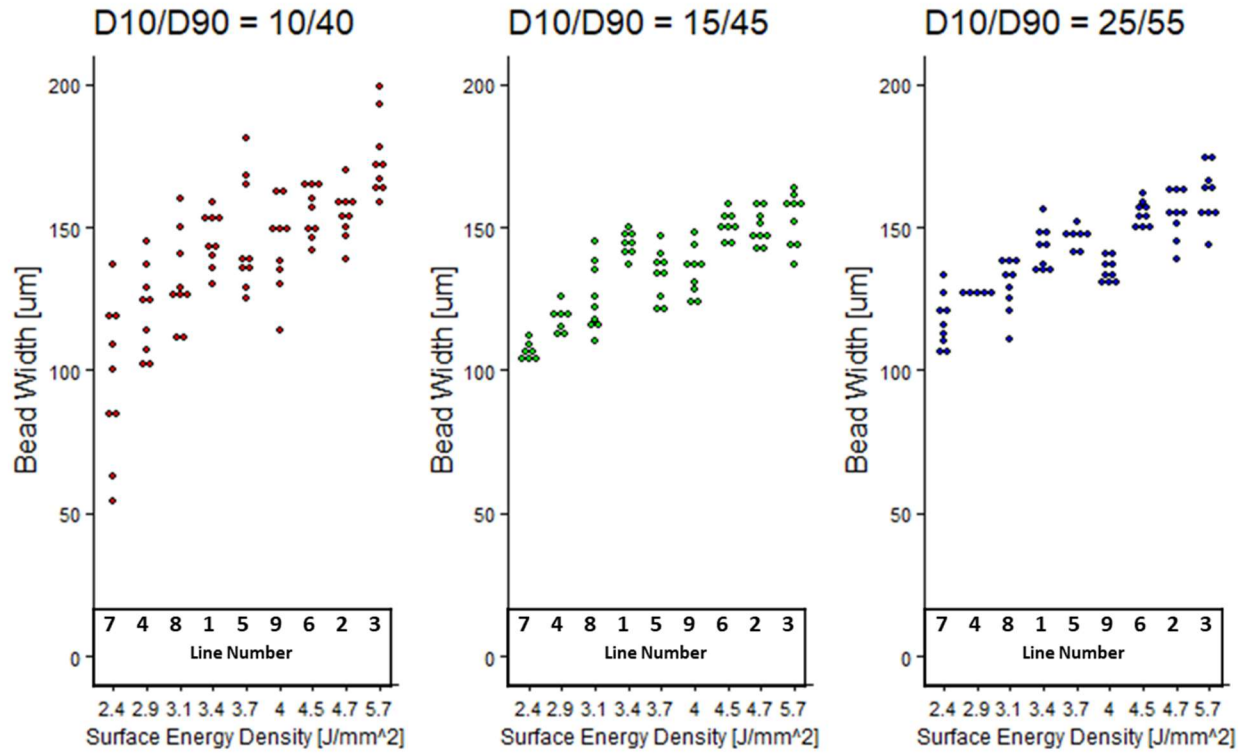


Figure 37: Dot plot of bead width arranged in terms of energy density including outliers

Through a more thorough removal of statistical outliers by applying box plots for each line number per subset, another histogram was created for both bead width and melt pool geometry and is shown in Figure 38. The distribution of the melt pool depth is similar to the initial histogram in Figure 31, where the distribution is tilted towards the left for melt pool depth. For bead width, the distribution is skewed towards the 150 µm interval with a frequency of more than 80, which meant that around 35% of the sample population had a bead width of approximately 150µm. Meanwhile, for melt pool depth, 131 out of the 229 remaining samples or 57%, lied in a wider interval between 50 and 100 µm.

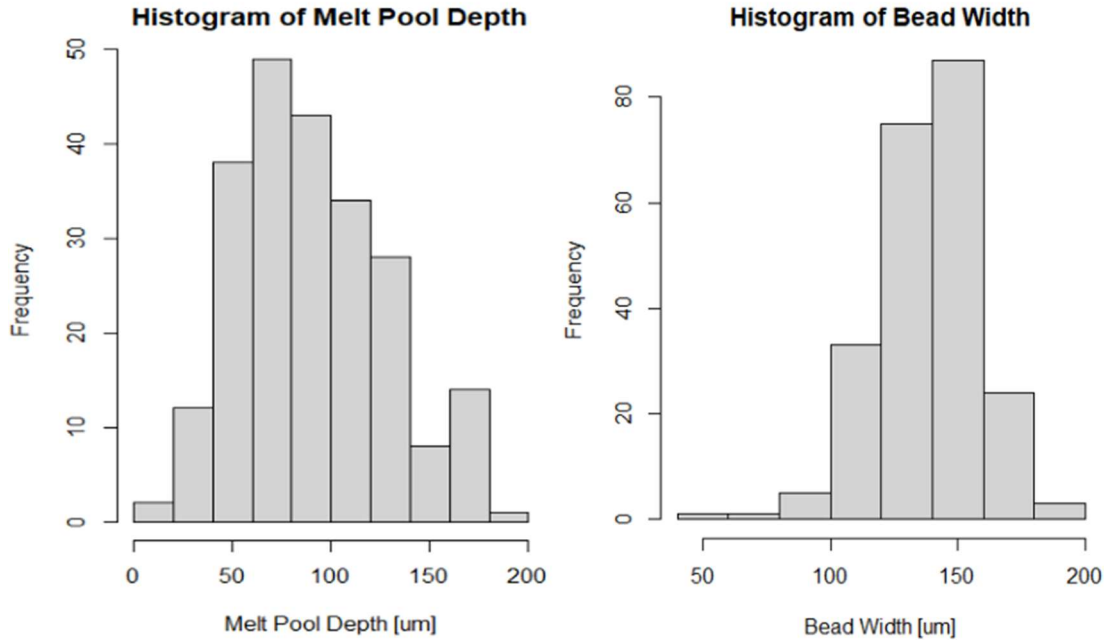


Figure 38: Histograms of melt pool depth (left) and bead width (right) with outliers omitted.

#### 4.1.4 Regression Analyses

The complete dataset with omitted outliers from the boxplots, as well as its subsets, were also re-evaluated using linear regression and ANOVA. The analysis results for melt pool depth were organized in Table 11 for the complete dataset and Table 12 for each subset representing the powder size distributions. Similar to Table 8, these tables included the linear regression coefficients and the coefficient of determination ( $R^2$ ), but the statistical significance would be represented by their respective p-values. If the p-value return from the analysis is very small, i.e.,  $p < 1e-8$ , it was displayed within the table as  $\sim 0$ . These very low p-values, representing an indication of the potential to reject the null hypothesis, indicated that the respective coefficients could be considered statistically significant. The adjusted coefficient of determination,  $R^2$ , used in these tables would also factor sample size, and thus, was tabulated. Other metrics that factor sample size, such as the standard deviation and mean squared error, are also included in Tables 11 and 12.

Compared to the initial linear regression and analysis in Table 8, the values for the coefficients describing the effect of the primary process parameters and powder size distribution were similar. Laser power and powder size distribution had positive coefficients, while the scan speed showed a negative coefficient. The magnitudes of laser power and scan speed were similar to the initial analysis of Table 8. However, the linear regression intercept value and powder size coefficients were lower. Additionally, comparing the magnitudes of the coefficients for each of the independent variables, again, showed that powder size had the largest coefficient, with the value of 1.07. This is believed due to bias from the smaller numbers representing powder size distribution levels, which were 25, 30 and 40  $\mu\text{m}$ , whilst the two other variables had their levels in the hundreds.

In terms of the ANOVA results, all primary process parameters and powder size distribution were, again, considered significant for melt pool depth. The linear regression equation of the complete dataset differed from the individual subsets based on powder size, which displayed similar coefficients. The adjusted  $R^2$  values from each subset showed improvement with increasing powder size, with the coefficient of determination being 95%, an almost ideal fit. Conversely, the fine powder size showed an inferior fit, with an  $R^2$  of 69.1%. As expected, the lower  $R^2$  value correlated to increases in the mean squared error, derived from the square root of the residual sum of squares (RSS). Standard deviations are also included in these tables, since the visual impression from Figure 33 showed higher variation in melt pool depth with finer powder sizes. However, the standard deviations between the subsets for powder size in Table 12 were similar, with the coarse powder exhibiting a slightly higher value. These standard deviations were calculated with respect to the subsets, and the box plots of Figure 34 account for the variation with each line number within a powder size subset. Thus, the standard deviation within each line number in each powder size subset were calculated and listed in Table 13. The results for the standard deviations found in Table 13 provide a statistical basis for the visual assumption made from Figure 33, that greater variability was seen with smaller powder size. An example would be that the Line Number 3 (P=345 W and V=760 mm/s) in the fine powder size subset had the highest standard deviation in Table 13 and the longest boxplot in Figure 33. Conversely, Line Number 9 (P=345 W and V=1160 mm/s) in the coarse powder size exhibited the lowest standard deviation, as well the smallest box plot in Figure 33. Comparing the average standard deviation within a powder size subset in Table 13 showed that the fine powder possessed the largest standard deviation, thus, statistically reinforcing the belief that variation in melt pool depth was influenced by powder size.

The same linear regressions were also applied to bead width. The results shown in Tables 14, 15, and 16 yield similar behaviors between powder size. In both cases, the regression improved with increased powder size distribution; however, the line of best fit for bead width was considered to be, generally, inferior when compared to the predictions for melt pool depth. An analogous pattern was also observed between the powder size distribution and standard deviation, with each line number within a powder size subset. The fine powder size distribution yielded an average standard deviation that was at least twice the standard deviation of the nominal and coarse powder distributions, both of which have near identical values. In general, the standard deviations within each line number for bead width tended to be lower than those of melt pool depth. This somewhat supports the assumptions from the histograms in Table 16 that the measured bead width tended to be more centralized around 150  $\mu\text{m}$ .

Figure 39 provides a bar graph that compares the linear regression adjusted  $R^2$  values for the melt pool depth and bead width in terms of the whole dataset and each powder size distribution subsets as listed in Tables 11, 12, 14 and 15. The standard deviation of for melt pool depth and bead width for each line numbers as tabulated in Tables 13 and 16 was also visually summarized as a bar graph in Figures 40 and 41, respectively.

Table 11: Melt pool depth linear regression and ANOVA results for the complete dataset

<b>Melt Pool Depth (Complete Dataset)</b>		
<b>Predictor</b>	<b>Coefficient</b>	<b>p-value</b>
Intercept	21.948	0.0234
Laser Powder	0.544	0
Scan Speed	-0.124	0
Powder Size	1.07	0
Standard Deviation ( $\mu\text{m}$ )	37.01	
Mean Squared Error	223	
Adjusted R <sup>2</sup>	0.84	

Table 12: Melt pool depth linear regression and ANOVA results for each powder size distribution subsets

<b>Melt Pool Depth (<math>D_{10}/D_{90} = 10/40\mu\text{m}</math>)</b>			<b>Melt Pool Depth (<math>D_{10}/D_{90} = 15/45\mu\text{m}</math>)</b>			<b>Melt Pool Depth (<math>D_{10}/D_{90} = 25/55\mu\text{m}</math>)</b>		
<b>Predictor</b>	<b>Coefficient</b>	<b>p-value</b>	<b>Predictor</b>	<b>Coefficient</b>	<b>P-value</b>	<b>Predictor</b>	<b>Coefficient</b>	<b>P-value</b>
Intercept	52.14	0.0073	Intercept	58.22	0	Intercept	57.39	0
Laser Powder	0.49	0	Laser Powder	0.56	0	Laser Powder	0.60	0
Scan Speed	-0.11	0	Scan Speed	-0.13	0	Scan Speed	-0.13	0
Standard Deviation ( $\mu\text{m}$ )	36.18		Standard Deviation ( $\mu\text{m}$ )	35.22		Standard Deviation ( $\mu\text{m}$ )	38.50	
Mean Squared Error	405.00		Mean Squared Error	162.00		Mean Squared Error	75.00	
Adjusted R <sup>2</sup>	0.691		Adjusted R <sup>2</sup>	0.870		Adjusted R <sup>2</sup>	0.949	

Table 13: Melt pool depth standard deviation between line numbers with each powder size distribution [ $\mu\text{m}$ ]

<b>Line Number</b>	<b>Laser Power</b>	<b>Scan Speed</b>	<b>Surface Energy Density [<math>\text{J}/\text{mm}^2</math>]</b>	<b>Standard Deviation (<math>\mu\text{m}</math>)</b>		
				<b><math>D_{10}/D_{90}=10/40\mu\text{m}</math></b>	<b><math>D_{10}/D_{90}=15/45\mu\text{m}</math></b>	<b><math>D_{10}/D_{90}=25/55\mu\text{m}</math></b>
1	225	760	3.70	17.9	9.0	3.3
2	285	760	4.69	16.5	12.6	9.1
3	345	760	5.67	34.8	6.6	11.3
4	225	960	2.93	10.2	9.3	7.1
5	285	960	3.71	16.0	9.2	3.6
6	345	960	4.49	27.4	12.4	9.9
7	225	1160	2.42	21.5	10.1	5.7
8	285	1160	3.07	16.1	8.7	7.3
9	345	1160	3.72	9.4	9.4	2.5
<b>Powder Size Subset Average Stand Deviation</b>				18.9	9.7	6.7

Table 14: Bead width linear regression and ANOVA results for the complete dataset

<b>Bead Width (Complete Dataset)</b>		
<b>Predictor</b>	<b>Coefficient</b>	<b>P-value</b>
Intercept	137.908	0
Laser Powder	0.231	0
Scan Speed	-0.070	0
Powder Size	0.060	0.878
Standard Deviation ( $\mu\text{m}$ )	20.24	
Mean Squared Error	151.7	
Adjusted R <sup>2</sup>	0.63	

Table 15: Bead width linear regression and ANOVA results for each powder size distribution subsets:

<b>Bead Width (<math>D_{10}/D_{90} = 10/40\text{mm}</math>)</b>			<b>Bead Width (<math>D_{10}/D_{90} = 15/45\text{mm}</math>)</b>			<b>Bead Width (<math>D_{10}/D_{90} = 25/55\text{mm}</math>)</b>		
<b>Predictor</b>	<b>Coefficient</b>	<b>P-value</b>	<b>Predictor</b>	<b>Coefficient</b>	<b>P-value</b>	<b>Predictor</b>	<b>Coefficient</b>	<b>P-value</b>
Intercept	137.341	~0	Intercept	128.362	~0	Intercept	157.516	0
Laser Powder	0.303	~0	Laser Powder	0.217	~0	Laser Powder	0.165	0
Scan Speed	-0.086	~0	Scan Speed	-0.057	~0	Scan Speed	-0.066	0
Standard Deviation (mm)	36.877		Standard Deviation (mm)	39.137		Standard Deviation (mm)	38.500	
Mean Squared Error	258.900		Mean Squared Error	0.727		Mean Squared Error	58.200	
Adjusted R <sup>2</sup>	0.611		Adjusted R <sup>2</sup>	0.714		Adjusted R <sup>2</sup>	0.777	

Table 16: Bead width standard deviation between line numbers within each powder size distribution [ $\mu\text{m}$ ]

<b>Line Number</b>	<b>Laser Power</b>	<b>Scan Speed</b>	<b>Surface Energy Density [<math>\text{J}/\text{mm}^2</math>]</b>	<b>Standard Deviation (<math>\mu\text{m}</math>)</b>		
				<b><math>D_{10}/D_{90}=10/40\mu\text{m}</math></b>	<b><math>D_{10}/D_{90}=15/45\mu\text{m}</math></b>	<b><math>D_{10}/D_{90}=25/55\mu\text{m}</math></b>
1	225	760	3.70	19.7	8.8	6.1
2	285	760	4.69	8.8	6.0	8.3
3	345	760	5.67	13.6	9.3	9.9
4	225	960	2.93	15.4	4.8	1.9
5	285	960	3.71	9.4	4.2	7.4
6	345	960	4.49	8.8	4.6	4.3
7	225	1160	2.42	27.5	3.0	9.1
8	285	1160	3.07	16.3	11.8	9.4
9	345	1160	3.72	15.7	8.4	4.0
<b>Powder Size Subset Average Stand Deviation</b>				15.0	6.8	6.7

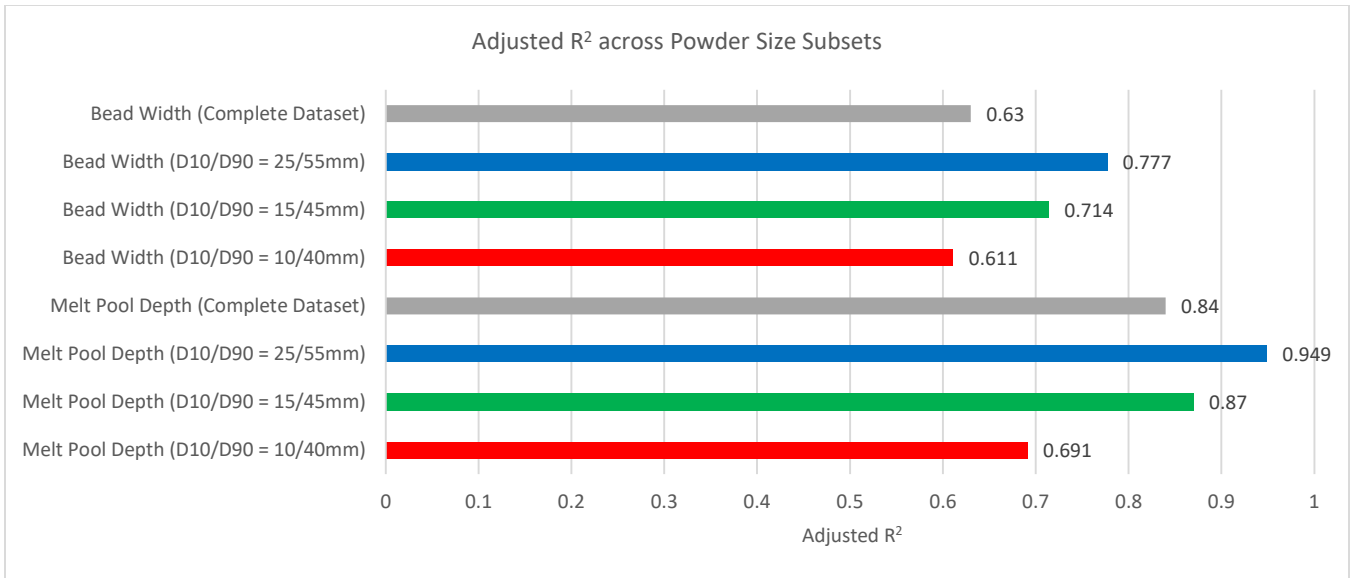


Figure 39: Adjusted R<sup>2</sup> across powder size subsets.

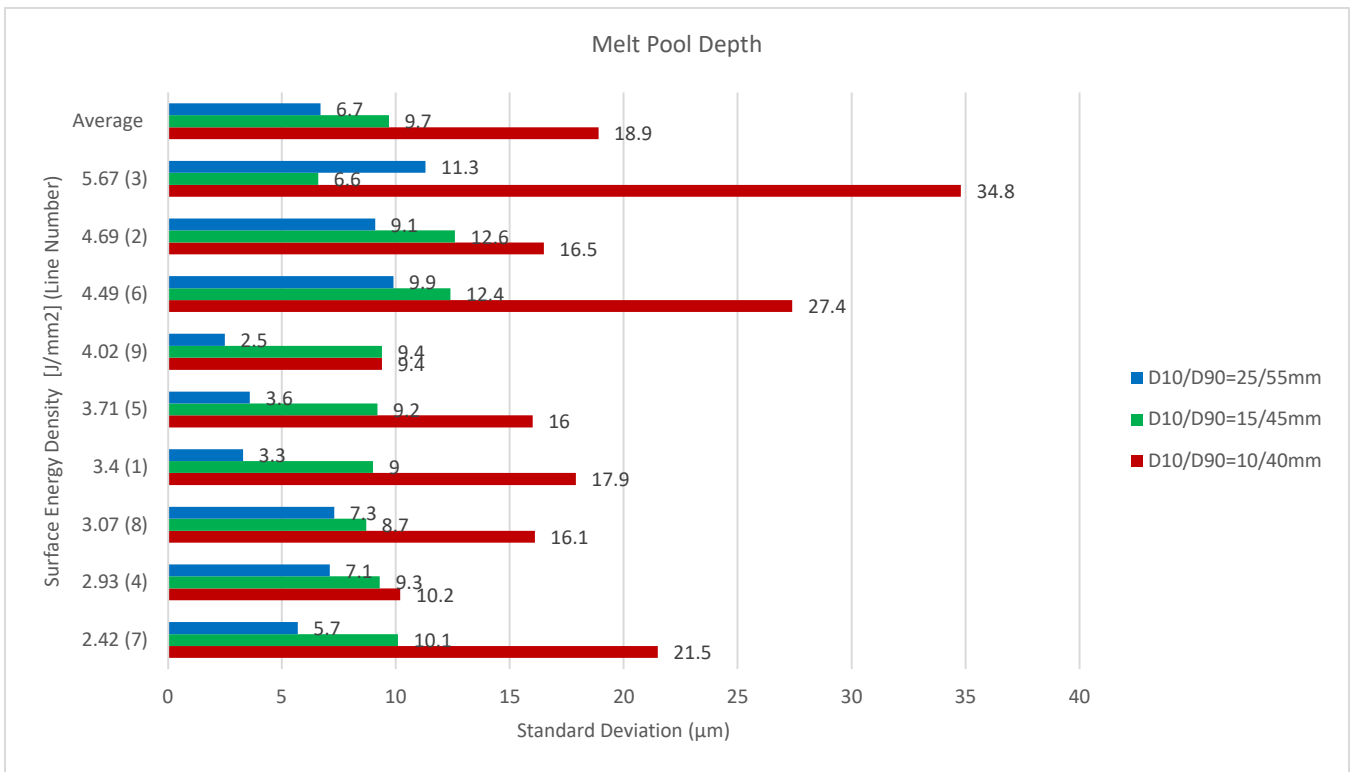


Figure 40: Bar graph for melt pool depth standard deviation for each line number.

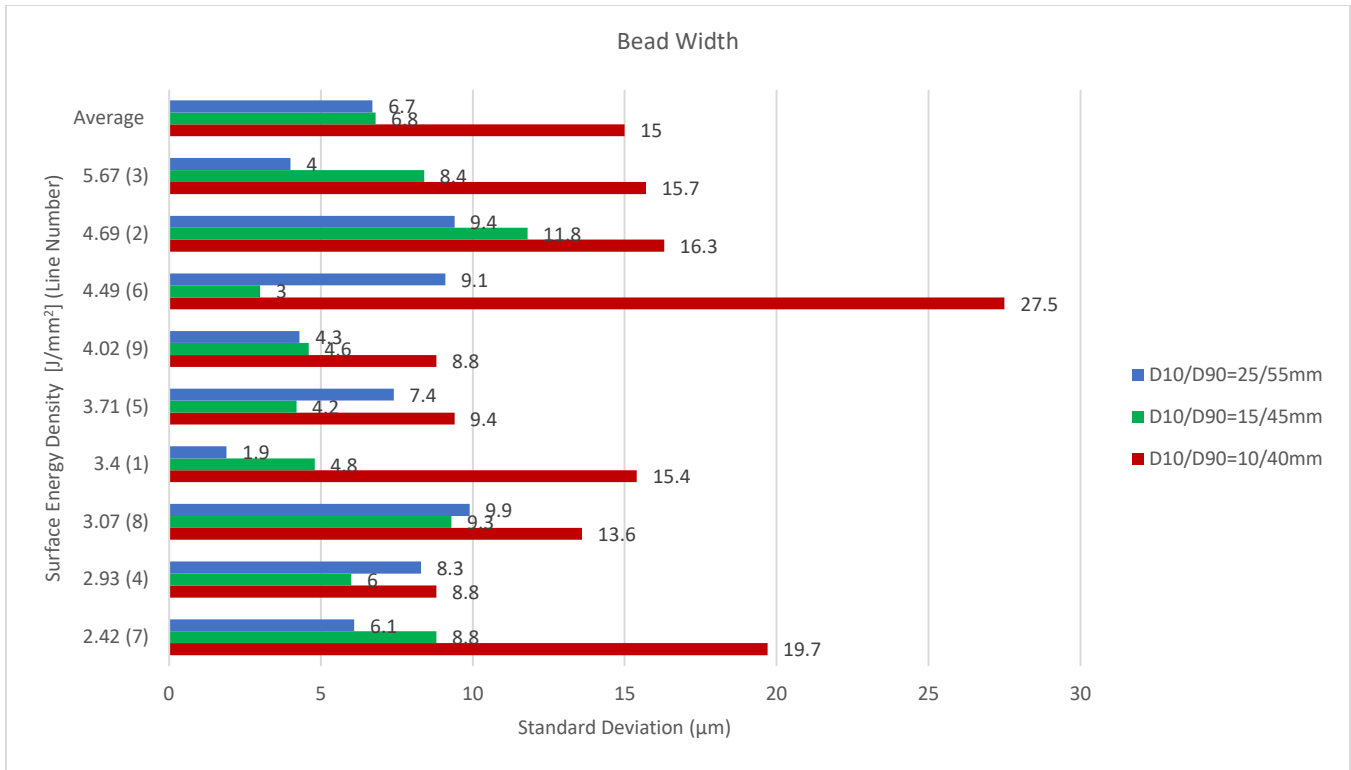


Figure 41: Bar graph for bead width standard deviation for each line number.

#### 4.1.5 Discussion of the Data Analyses

The results of the statistical analyses of the data revealed the implications of powder size on determining melt pool depth and variability. Figure 42 from McVey et al provides a visual demonstration of the scattering behavior of laser irradiation within a layer of metallic powder [29]. As the laser beam contacts a powder particle, a fraction of the laser is absorbed as heat while the rest is reflected away with a lower intensity. The laser energy reflected from the particle then contacts another particle and the process is repeated with the laser energy continuing to lose energy or become attenuated as it penetrates the powder. This process is much different than when a laser beam is presented to a solid metal, whereas, in this case the laser energy is absorbed at the surface and the reflected energy is directed away from the material.

In the case of a finer powder size distribution, the smaller particle size results in the incident laser reflecting more often than with coarser powders and displaying a greater attenuation. The larger particle sizes of coarser powder, however, would have larger gaps. These gaps allow the incident laser to travel further within the powder layer, as there is a relatively lower probability of interacting with a particle. The scattered laser going through the coarser powder would likely have higher intensity values, owing to less prior reflections, which allow for greater energy for melting and relatively deeper melt pools. McVey et al tabulated the attenuation coefficients,  $\gamma$ , for pure copper and iron at three powder size distributions. Their analysis showed that the finer iron powder, having a size range of between 14 and 105  $\mu\text{m}$ , displayed a higher attenuation coefficient though this estimation was noted to have poor regression fitting with the

experimental data. The author noted in their conclusion that the multiple scattering effect may have contributed to the lack of accuracy. This conclusion could also help in explaining the higher variability associated with the fine power. McVey also remarked that the coarser powder distribution of between 106 and 210  $\mu\text{m}$  had a lower attenuation coefficient, which supports the observation made during the current research [29].

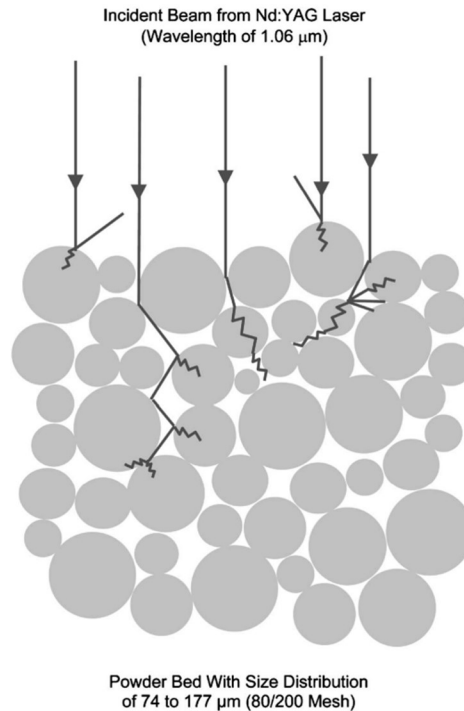


Figure 42: Scattering of laser as it goes through the powder layer[29]

Other research reported in the literature also discussed the implications of powder size distribution on the laser powder bed process. Lee et al applied informatics on data obtained from physical experiments for predicting melt pool geometry. This study examined a more expansive design space by factoring not just the primary process parameters and powder size distribution but also elemental composition, materials properties, and other process variables, such as layer thickness and beam diameter. Additionally, besides linear regression Lee et al used other techniques, such as super vector machines and neural networks. Analysis of these variables also included the utilization of Equation 2 for the Pearson Correlation Coefficient (PCC). The correlation of the variables involved in that study were compared to the results in Section 4.1.2. Unsurprisingly, both primary process parameters of laser power and scan speed showed the highest PCC. Subsequently, the following highest coefficients were from the powder size distribution variables. However, the PCC for powder size distribution was higher for width than depth, which contrasts with the conclusion drawn from correlation analysis. Another divergence from Lee et al is that the results compared to the prior informatics investigation was in the quality of the predictive relationships between bead width and melt pool depth. The current analysis using regression of the width resulted in highly accurate coefficients of determination ( $R^2$ ), hovering around 0.9 for all models used in this study. In contrast, depth regressions from other research showed  $R^2$  of slightly above 0.7 at the minimum, with

some models having improved accuracies when factoring more variables, such as support vector machines, random forest regression, and neural networks [20].

Brika et al, in the meantime studied the implications of powder morphology and manufacturing method in terms of powder flow, mechanical properties, and dimensional accuracy of their prints. Three powders were examined in that study: the first powder was produced from gas atomization, the second powder having the same powder size distribution as the first but produced from plasma atomization which contained more spherical powder, and the third powder, which was also produced through plasma atomization but having a finer powder size distribution. This study concluded that the quality of powder had implications from a macro or part scale. The conclusion also stated that finer powder size could result in poorer powder flow due to high inter-particle friction [54]. Though the analysis of this paper demonstrated the potential of coarser powder size to provide more consistent melt pools, which could possibly lead to parts having greater predictability of properties. Rausch et al had a more cautious opinion towards coarse powder size. Their study concluded that a higher powder size mean could lead to high surface roughness and subsequently a porous part. Examining the experimental data in this study indicated that most of the mean powder size utilized was higher than those of the coarse powder for the current study, which had a  $D_{50}$  of  $40\ \mu\text{m}$ [55]. Therefore, based on this study, the potential benefits of coarser powder size, in general, could either have tradeoffs in the form surface roughness and porosity but must not be too large to induce these defects.

Other literature regarding the implications of powder size distribution tended to focus more on their effects on macro or part-scale properties, similar to the aforementioned studies by Brika et al and Rausch et al. Determining the effects of powder size distribution on the meso-scale, such as melt pool geometry, appears to be scarce. Though Lee et al included powder size distribution in their analyses, each  $D_{10}$ ,  $D_{50}$ , and  $D_{90}$  levels were associated with different materials and machines and included IN628 and IN718 printed with an ExOne Mlab system and IN718 printed with a Concept Laser M2 system. Additionally, the  $D_{10}$ ,  $D_{50}$ , and  $D_{90}$  values between each material and machine in Lee et al were almost identical. In contrast, the three levels of powder size distributions featured in the current research represented significant differences for the same material and the same AM machine. Spurek et al also examined the relationship between melt pool geometry with different powder size distributions [56]. The results of that study are shown in Figure 43. Interestingly, the results of their study had the opposite conclusion that was drawn from the current work. Their analysis indicated that coarser powder size distributions decreased melt pool depth and the variability, at least in terms of bead width, increased. Spurek et al attributed these results due to more energy being required to melt larger powder particles. However, it should be noted that the environment that Spurek et al operated their experiment was drastically different from the current study. Spurek et al used 316L stainless steel powder with a smaller layer thickness of  $30\ \mu\text{m}$  and a larger beam diameter of  $105\ \mu\text{m}$ . The machine used in their study was the Concept Laser M2 with a nitrogen atmosphere, whereas the physical experiments in the current study used an EOS system and argon gas. In terms of primary process parameters, Spurek et al used a constant laser power of 180 W and scan speeds ranging from 1000 mm/s to 2000 mm/s, which yielded much lower surface energy densities of 0.86 and 1.71 J/mm<sup>2</sup>. Because of the contradicting results between the current research and that conducted by Spurek et al, further experiments using the energy densities employed by Spurek et al and the powder sizes utilized in this research are suggested to provide a more definitive conclusion on the impact of powder size distribution on melt pool depth and width.

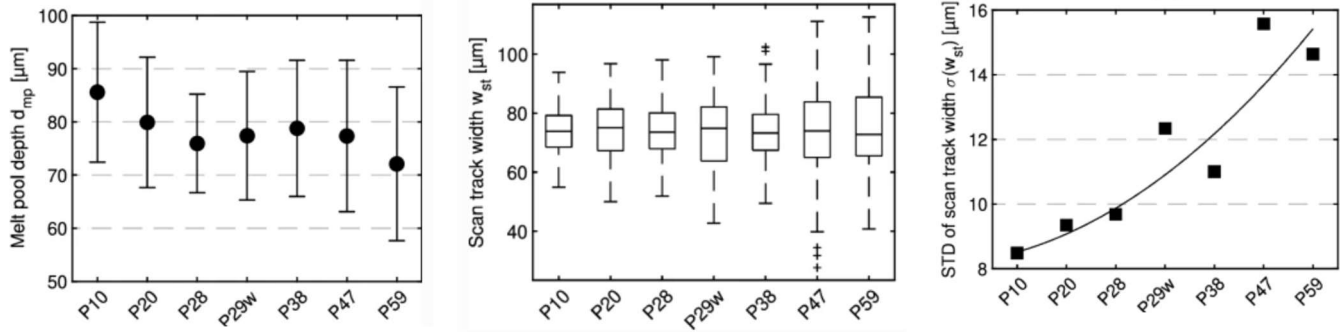


Figure 43: Effect of Powder  $D_{50}$  on melt pool depth, bead width and bead width standard deviation according to Spurek et al [56]

Another factor that should be considered in future work would be location on the build plate. During the literature search for the implication of powder size distribution on melt geometry for the powder bed fusion process, Pal et al considered the effects of location with respect the recoater to the overall part density. The general results of that study showed that further distances yielded parts with lower density [57]. However, Figure 44 from Pal et al showed the distribution of particle sizes with respect to the distance travelled by the recoater could have ramifications in melt pool geometry. In the lower half of Figure 44, the shorter distance travelled by the recoater resulted in more large particles, while the distribution of powder sizes skewed towards smaller particles with increasing distances.

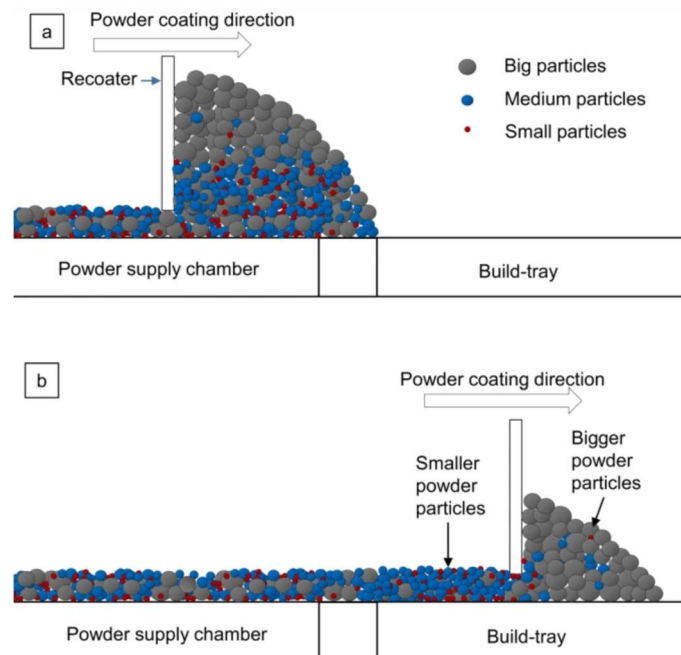


Figure 44: Distribution of powder particle size with recoater distance [57].

## 4.2 Simulation Results and Comparison with Experimental Data

### 4.2.1 Temperature and Velocity Profiles

Before examining melt pool dimensions of the simulations, the path dependency of the thermal conductivity had to be verified. Figure 45 shows the initial thermal conductivity of the powder and bulk layers. If the code in Figure 25 performed as intended, the top and bottom layers should share the same thermal conductivity after the laser passes. Figures 45, 46, and 47 shows the thermal conductivity distribution at the initial condition, during melting after 500  $\mu\text{s}$  of simulation time, and cooling after 900  $\mu\text{s}$  of time. It should also be noted that the units in these figures for thermal conductivity is in  $\text{W/m}\cdot\text{K}$ . As Figure 47 demonstrates, the thermal conductivity of the melted powder layer matches that of the bulk layer once the temperature has cooled. Therefore, it can be concluded that the algorithm of Figure 25 provides the anticipated path dependent behavior for thermal conductivity.



Figure 45: Initial thermal conductivity distribution between powder and substrate (longitudinal view).

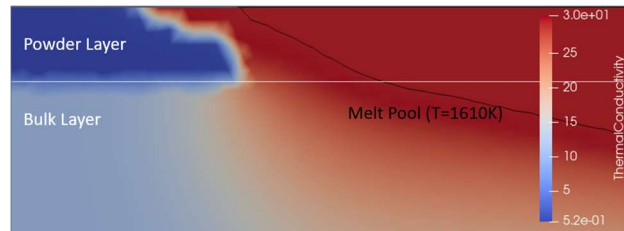


Figure 46: Powder conductivity at 500 $\mu\text{s}$  with melt pool present.

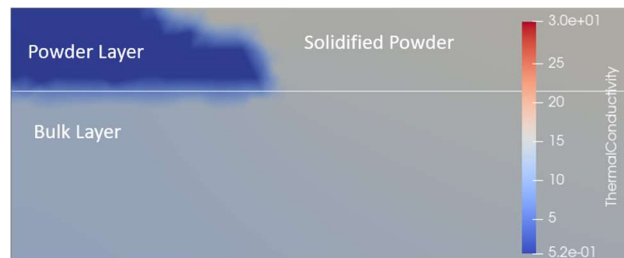


Figure 47: Thermal conductivity at 9000 $\mu\text{s}$  after cooling to near room temperature.

With the path dependence of the thermal conductivity verified, the thermal response, fluid flow, and melt pool dimensions were evaluated. Figures 48 and 49 illustrate the thermal responses in the longitudinal and cross-sectional views, respectively. Both figures showed black contour lines for the solidus and liquidus temperatures. A contour line for vaporization temperature is also added to show a potential vapor cavity based solely on temperature. While in the longitudinal view, additional white contours were added to represent the volumetric energy distribution representing laser attenuation used in the model. The melt pool depth was measured from the powder-bulk interface to the lowest liquidus point, similar to Figure 9. Also, the bead width was measured from the symmetrical plane to the liquidus point along the interface between the powder and bulk layers. These measurements were performed on simulation results after 300 time steps, which represented  $300 \mu\text{s}$  of simulation time. As stated in Section 3.2.3, this time was shown to achieve quasi-steady state conditions based on melt pool depth and bead width.

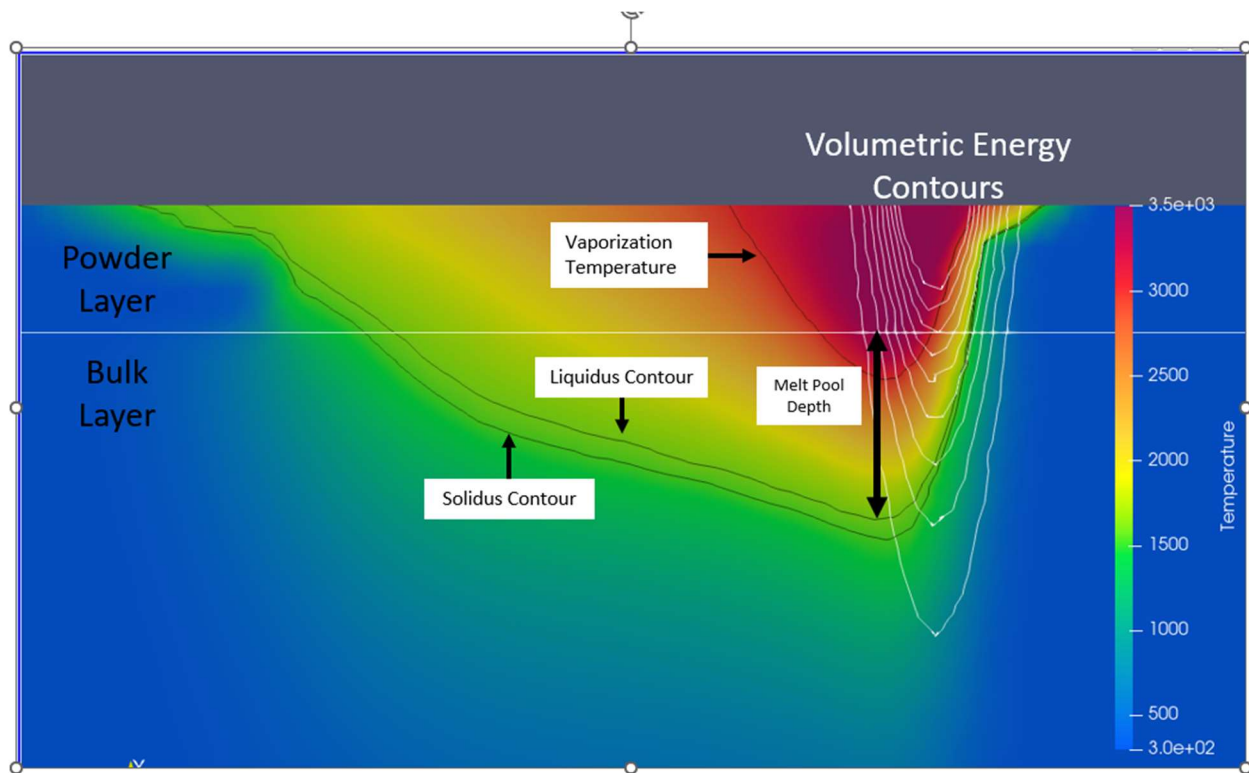


Figure 48: Longitudinal temperature profile for parameters 285W and 960mm/s at  $300 \mu\text{s}$  (in Kelvin).

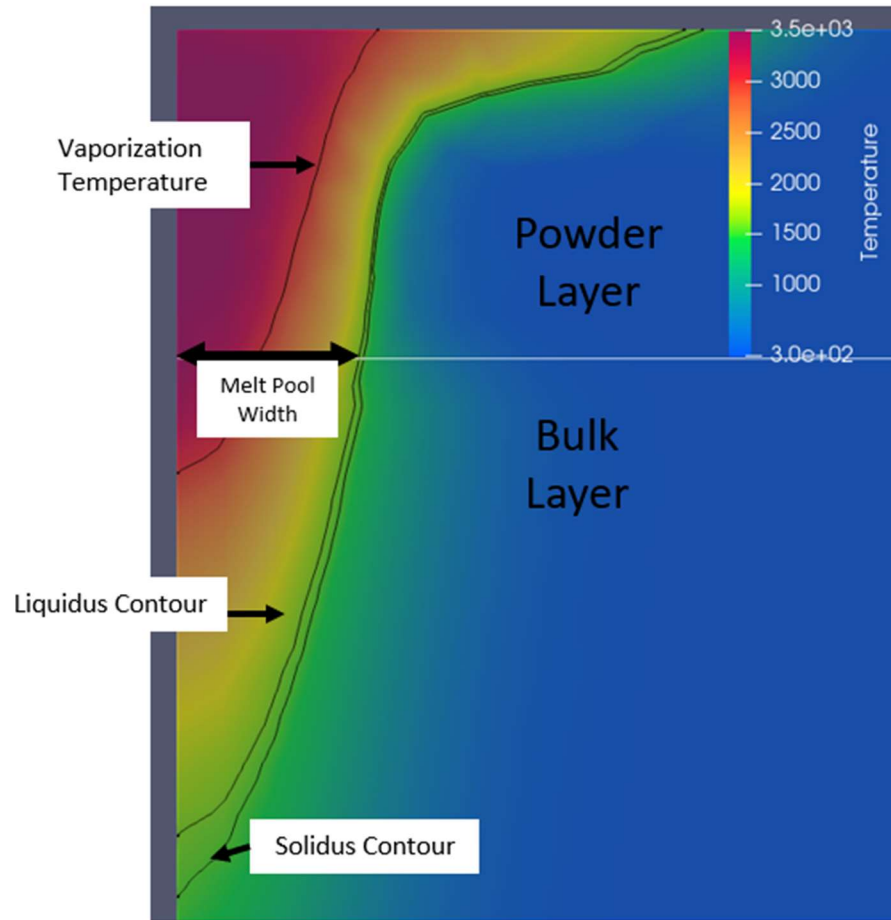


Figure 49: Cross section temperature profile for parameters 285W and 960mm/s at 300µs (in Kelvin).

The velocity vectors were also examined to observe the flow behavior predicted within the model, specifically, flow resulting from the Marangoni effect. Similar to the thermal responses, a longitudinal and cross-sectional view is provided in Figures 50 and 51, respectively. In the longitudinal view, the direction of the vectors is projected from the solidus contours towards more elevated temperatures, such as found within the potential vaporization cavity seen in the left of Figure 50. Additionally, the longitudinal view showed two convective loops, one under the beam and another trailing the beam but within the liquid. According to Cheng et al, the two loops cause the melt pool to split due to the surface tension being unable to maintain the melt pool geometry. This split, caused by the backward melt loop as the rear solidifies, could contribute to surface humps and balling effects [21]. The highest flow velocities of the liquid metal tended to be at the top surface where Marangoni convection was the highest due to the presence of larger thermal gradients. The maximum velocity shown in Figure 51 is 3 m/s, which corroborates with results of other flat surface models for IN718 performed using ANSYS Fluent, such as with Le et al [58] and Cao and Yuan [33]. Whereas, other flat surface models, Zhang et al [59] and Wei et al [60], reported maximum velocities of 0.79 m/s and 0.2 m/s, respectively. Lee and Zhang's models,

however, possessed a higher fidelity by including the ability to form a free surface and also had comparable velocity with vectors that were scaled to 2 m/s [45].

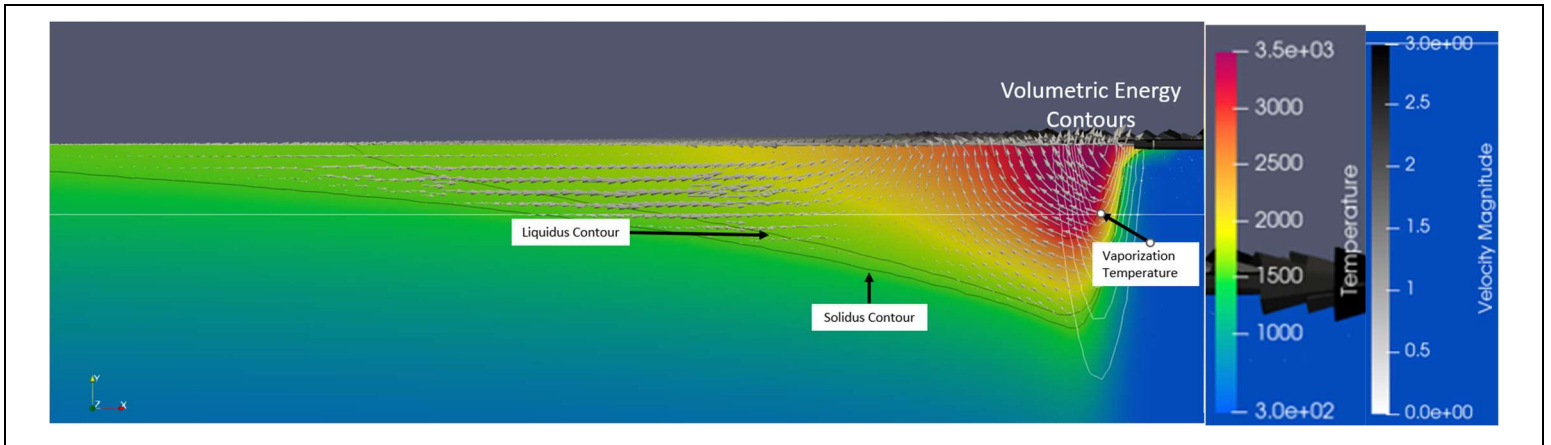


Figure 50: Longitudinal view of velocity vectors at 1300µs (in m/s).

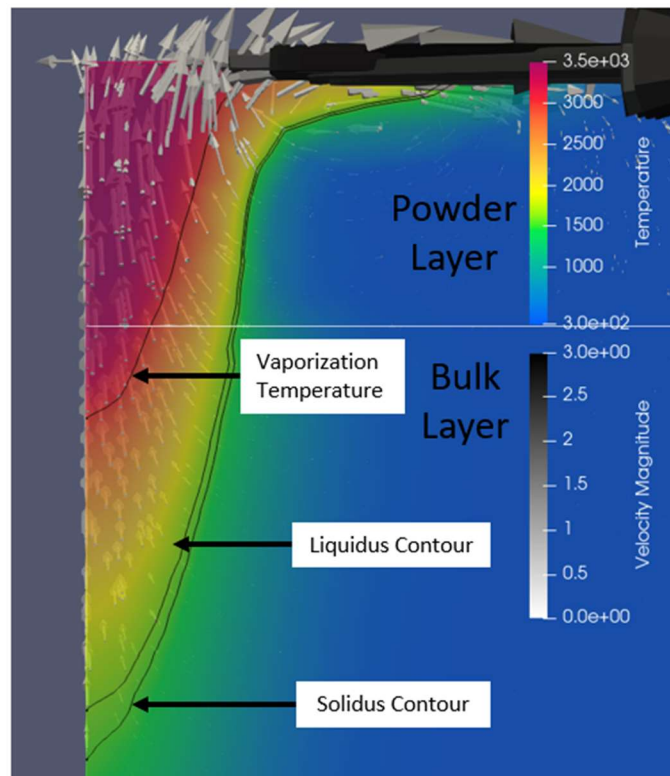


Figure 51: Cross-section view of velocity vectors at 1300µs (in m/s).

The limitations of the current model are more evident in the cross-sectional view. As mentioned earlier, the Marangoni effect on flow is most evident at the top surface where the model considers this boundary as a static “free surface”. Examining the cross-sectional view indicates that the melt pool only expands along the top surface, while the rest of the melt pool stayed relatively narrower. Another anomaly of the melt pool profile is that there are some velocity vectors that are present outside the solidus line at the top surface. This is likely due to the tracking of the liquid fraction, where the solidus line aligns roughly with the liquid fraction of 0.25, while the liquidus line aligns at 0.75. The extremely close proximity between the liquidus to the solidus line at the top surface could have also impeded the dampening of the velocity to 0 m/s.

#### 4.2.2 Melt Pool Geometry Measurements

Tables 17 and 18 list the melt pool geometry measurements for depth and width, respectively, based on the physical experiments and virtual simulations. The tables were organized by line number and their corresponding primary process parameters, laser power and scan speed, and the mean average response for each line number starting with the simulated measurement. Because the results of Section 4.2 found that powder size distribution was statistically significant with respect to the melt pool depth, the average responses for the whole data set, and subsets based on the powder size distributions, were also listed. The percent error between the results of simulations and the average of the measurements from the physical experiments are also listed in the tables.

As mentioned earlier the attenuation coefficient or  $\gamma$ -value from Equation 10 was adjusted to minimize the percent error between the simulation and experimental results. The subset for the nominal powder size ( $D_{10}/D_{90} = 15/45 \mu\text{m}$ ) was used for this calibration. During this adjustment, Line Numbers 3 ( $P=345 \text{ W}$  and  $V=760 \text{ mm/s}$ ) and 7 ( $P=225 \text{ W}$  and  $V=1160 \text{ mm/s}$ ) which had the highest and lowest surface energy densities, respectively, yielded the highest percent errors. An attenuation factor that minimized the error for one condition, increased the error for another. The highest percentage of errors with a selected attenuation value of 13,500/m were approximately 33%, as listed in Table 17. Compared to the other subsets, the percent error was generally higher when compared with the fine powder size ( $D_{10}/D_{90} = 10/40 \mu\text{m}$ ), with an extreme difference in the case of Line Number 7 having an 85% error. Conversely, comparing the simulation measurements to the averages for coarser powder size ( $D_{10}/D_{90} = 25/55 \mu\text{m}$ ) for Line Numbers 3 and 7 showed a decrease in percent error. The Line Numbers of 1, 5, and 9 had surface energy densities of approximately  $3.7 \text{ J/mm}^2$  and tended to have lowest differences between the results from simulations and mean of the experimental measurements. However, the error between the two increased when viewing the results for the coarser powder. Despite that, the total average error within each powder size subset decreased as the powder size increased.

For the width, all the results from the virtual simulations were significantly less than the experimental values. Interestingly, the percentage errors were consistently in the range between 46 and 49%. Other than that, there were no discernable patterns for the differences between the simulations and experimental measurements for width, which is seen in Table 18 in terms of the percentage errors. In order to further examine the data for any potential patterns, both the results shown Tables 17 and 18 were visualized using the graphs of Figures 52 and 53. These graphs further confirmed the belief that powder size had a statistically relevant influence on melt pool depth. In Figure 52, it is evident that finer powder size resulted in a decrease in melt pool depth over the range of energy densities evaluated. This pattern,

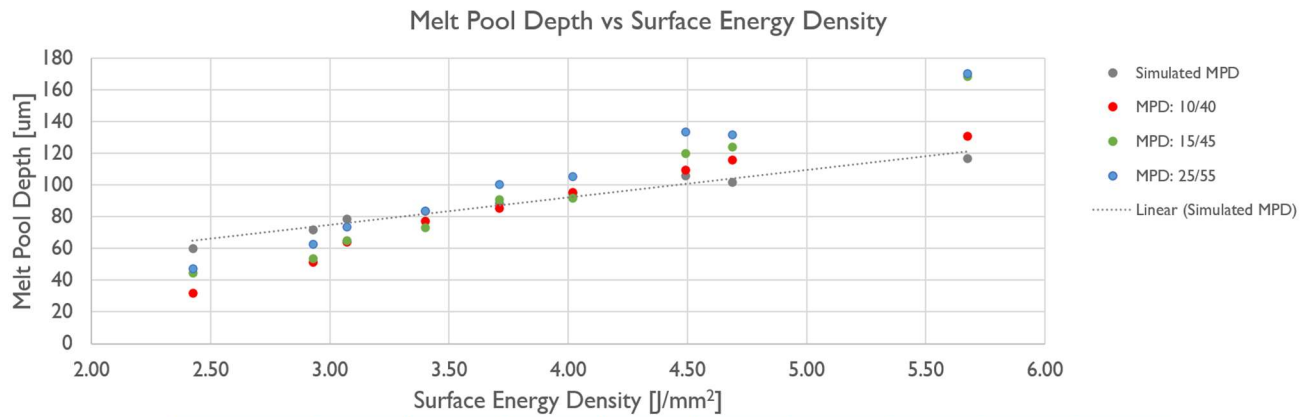
however, is not as apparent with the average measurements for Lines 1 (P=225 W and V=760 mm/s) and 9 (P=345 W and V=1160 mm/s), where the calculated mean for the nominal powder size for these parameter combinations showed slightly deeper penetration. At the extremes of the energy densities, the difference in melt pool depth from the simulations and the physical experiments were observed to be larger.

Table 17: Comparison between simulated vs experimental melt pool depth.

Line Number	Laser Power [W]	Scan Speed [mm/s]	Surface Energy Density [J/mm <sup>2</sup> ]	Total Dataset			D10/D90 = 10/40		D10/D90 = 15/45		D10/D90 = 25/55	
				Simulated MPD [μm]	Average Measured MPD [μm]	% Error						
1	225	760	3.70	84	78	7.28%	77	8.5%	73	14.4%	84	0.00%
2	285	760	4.69	102	124	-17.82%	116	-12.0%	124	-18.0%	132	-22.81%
3	345	760	5.67	117	157	-25.32%	131	-10.6%	169	-30.6%	171	-31.38%
4	225	960	2.93	72	56	28.23%	52	39.7%	54	33.3%	63	14.49%
5	285	960	3.71	89	93	-3.79%	86	3.8%	91	-2.1%	101	-11.76%
6	345	960	4.49	106	121	-12.56%	110	-3.5%	120	-11.7%	134	-20.70%
7	225	1160	2.42	60	41	44.64%	32	87.5%	45	33.7%	48	26.17%
8	285	1160	3.07	79	68	16.57%	64	22.6%	65	21.3%	74	7.12%
9	345	1160	3.72	95	98	-2.79%	96	-0.8%	92	3.3%	105	-9.89%
<b>AVERAGE Error</b>						<b>17.7%</b>		<b>21.0%</b>		<b>18.7%</b>		<b>16.0%</b>

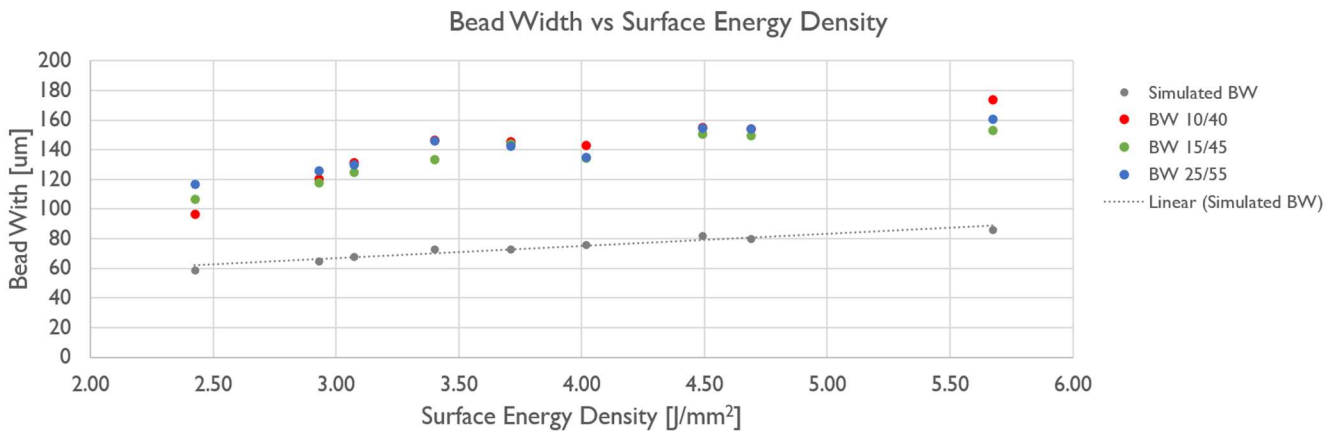
Table 18: Comparison between simulated vs experimental bead width.

Line Number	Laser Power [W]	Scan Speed [mm/s]	Surface Energy Density [J/mm <sup>2</sup> ]	Simulated BW [μm]	Total Dataset		D10/D90 = 10/40		D10/D90 = 15/45		D10/D90 = 25/55	
					Average BW [μm]	% Error						
1	225	760	3.70	73	142	-48.6%	146	-50.2%	133	-45.3%	146	-50.1%
2	285	760	4.69	80	153	-47.6%	154	-48.2%	150	-46.5%	154	-48.2%
3	345	760	5.67	86	163	-47.1%	174	-50.6%	153	-43.8%	161	-46.6%
4	225	960	2.93	65	121	-46.5%	121	-46.1%	118	-44.8%	126	-48.4%
5	285	960	3.71	73	144	-49.3%	146	-49.8%	144	-49.4%	143	-48.8%
6	345	960	4.49	82	154	-46.6%	155	-47.2%	151	-45.5%	155	-47.1%
7	225	1160	2.42	59	107	-44.8%	97	-39.0%	107	-44.7%	117	-49.6%
8	285	1160	3.07	68	129	-47.2%	131	-48.3%	125	-45.6%	130	-47.6%
9	345	1160	3.72	76	138	-44.7%	143	-47.0%	134	-43.4%	135	-43.7%
<b>AVERAGE Error</b>						<b>46.9%</b>		<b>47.4%</b>		<b>45.4%</b>		<b>47.8%</b>



Line Number	7	4	8	5	6	2	3	1	9
Laser Power (W)	225	225	285	285	345	285	345	225	345
Scan Speed (mm/s)	1160	960	1160	960	960	760	760	760	1160
SED [J/mm <sup>2</sup> ] (Stagger)	2.42	2.93	3.07	3.71	4.49	4.69	5.67	3.70 (3.4)	3.72 (4.02)

Figure 52: Melt pool depth vs surface energy density.



Line Number	7	4	8	5	6	2	3	1	9
Laser Power (W)	225	225	285	285	345	285	345	225	345
Scan Speed (mm/s)	1160	960	1160	960	960	760	760	760	1160
SED [J/mm <sup>2</sup> ] (Stagger)	2.42	2.93	3.07	3.71	4.49	4.69	5.67	3.70 (3.4)	3.72 (4.02)

Figure 53: Bead width vs surface energy density.

### 4.2.3 Discussion on the Physics-based Model

Due to its sensitivity to the primary process parameters, the melt pool measurements from the simulations can be considered reasonable when compared to the physical experiment. The bead width found from experiments were consistently under predicted in the simulations. The difference between the simulations and physical experiments also increased with, both, higher and lower energy densities. The

underestimation of the melt pool depth with higher energy densities, and potentially, the bead width may be attributed to the lack of several physical phenomena, such as the inability to create a vapor cavity through the use of a free surface and absence of vapor pressure. The presence of the vapor cavity would allow for further penetration of the laser beam through secondary reflections within the cavity and thus more heat to be applied at greater depths in the melt pool. The formation of the vapor cavity is due to loss of mass through vaporization with the subsequent recoil forces maintaining the liquid walls of the cavity. This phenomenon affects melt pool geometry, as this pressure pushes towards the vapor cavity and subsequently expands, both, melt pool depth and bead width. Lee and Zhang provided a simple graphic on how vapor pressure affects the melt pool, which is shown in Figure 54[45]. A similar flat surface model by Le et al experienced similar complications in that the differences between virtual simulation and physical experimentation measurements increased with higher energy density [58]. Though melt pool depth was shown to be directly influenced by the primary process parameters, it is hypothesized that there is a point at which the applied energy density may increase the extent of vaporization, and this could significantly impact melt pool depth and render the flat surface model inaccurate.

The overestimation of melt pool depth at lower energy densities, however, is more ambiguous. It could possibly be due to how the size of the powder influences the melt pool depth, as seen in Section 4.1. The finer powder could mean that the laser is unable to penetrate deeper into the powder layer, and thus, its potential to create a deeper melt is diminished when compared to larger powders diameters. The heat source model described in Equation 10 does have the potential to define an attenuation based on several physical traits of the power, such as size and optical properties. Hence, the model may be used to reproduce the effect of powder size on attenuation for a given material and powder size distribution. However, because these determinations are experimentally cumbersome, the determination of a reasonable attenuation coefficient is typically performed through trial and error. This is achieved by adjusting the attenuation coefficient, the variable  $\gamma$ , to converge the measured depth with the simulation depth. Utilizing this approach,  $\gamma$  was calibrated within the model. These adjustments showed that higher values of  $\gamma$  resulted in a shallower melt pool. Conversely, the lower  $\gamma$  values provided deeper melt pools. Therefore, it can be induced that  $\gamma$  can be used as a representation of how powder size influences melt pool depth through the modification of laser energy attenuation through the powder layer.

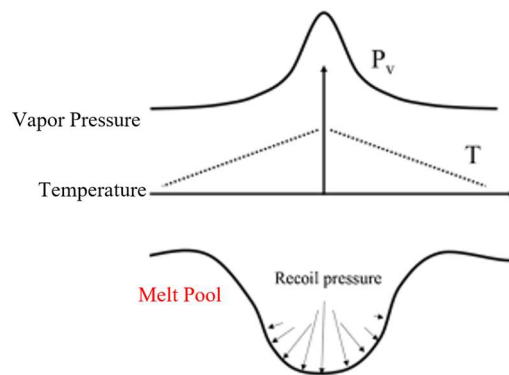


Figure 54: Vapor pressure illustration [45].

The physics-based model in this study, however, was unable to replicate accurate bead width, as defined through measurements from the physical experiments, which was believed to be partly due to the lack of the model to represent a free surface. The same anomalous melt pool shape observed in the cross-section from this work was also observed on the melt pool shape of Cao and Yuan, which is pictured in Figure 55. In the figure, the melt pool width is seen to only expand at the top surface where the Marangoni effect is applied as a boundary condition. However, the bead width at the powder-bulk interface appears wider than that pictured in Figure 51. It should be noted that the melt pool profile between the powder layer and bulk layer were discontinuous as shown in Figure 56. This implies that Cao and Yuan had the powder layer and bulk defined within the model as two separate geometries, unlike the model constructed for this study. Cao and Yuan's model has a flaw in that flow only applies to the top geometry representing the powder but not in the melt pool of the bulk layer, as seen in Figure 56 [33]. Another flat surface model using ANSYS Fluent was based on the work of Le et al that featured a wider width. Further examination of this study found major differences between the current model and that constructed by Le et al. Both heat sources have a Gaussian profile with respect to the horizontal plane. However, while the model of this study uses a heat source based on the experiments of McVey et al, which featured exponential decay, the heat source behavior of Lee et al is based on a varying absorption coefficient. Additionally, the absorptivity values are also state dependent with a corresponding value for the bulk and liquid states. Another major difference between these two approaches involves how the Marangoni coefficient was applied. In the case of Le et al, the temperature dependency of the surface tension is exponential instead of linear, which was used in their model, to account for the presence of oxidizing elements, such as sulfur and oxygen. It is also noted that Le et al had the opposite complication regarding bead width. Whereas the model in this study severely underestimate bead width, Le et al overestimates it by 34% [58].

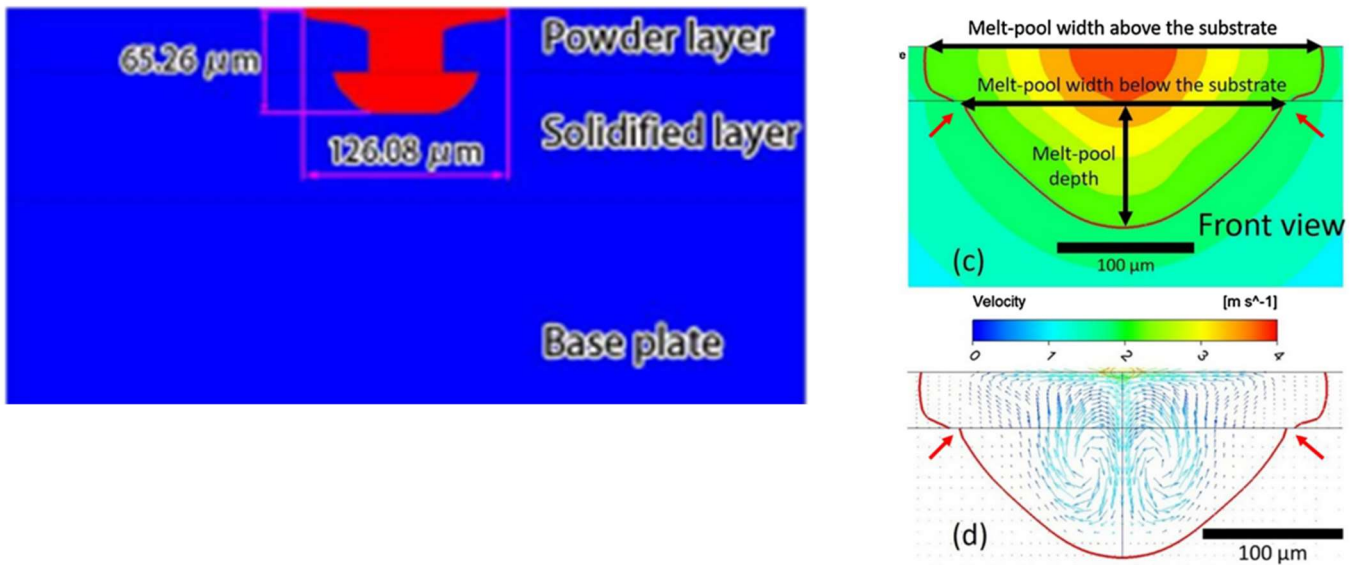


Figure 55: Cross-sectional melt pool from Cao and Yuan [33] (left) and from Le et al[58](right).

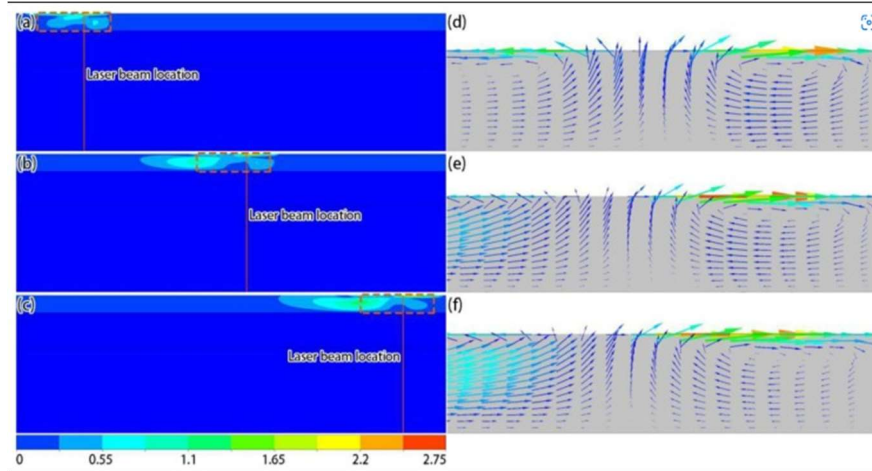


Figure 56: Velocity profile of Cao and Yuan [33].

Despite its inability to create a verifiable melt pool geometry, the limitation of the current model to not account for certain physical phenomena appears to impact the ability to accurately simulate bead width more than melt pool depth. Whereas the inaccuracies in melt pool measurements do not appear with moderate energy densities, the simulated bead width was constantly narrower than measured values, regardless of the combination of primary process parameters. A possible explanation of how vapor pressure influences bead width more than melt pool depth could be based on the depth having more resistance to the recoil forces generated by vaporization. The recoil forces applied at the root of the vapor cavity would be in close proximity to the solid or bulk material providing a much greater resistance. With lower energy densities, secondary laser reflections in the vapor cavity may not have sufficient intensity to encourage more evaporation, and the vapor pressure would be too low to further displace the liquid metal.

A demonstrative example of a higher fidelity model that includes the missing phenomena of vaporization, recoil/vapor pressure, and a changing free surface is one constructed by Queva et al [34]. Figure 57 is adopted from this work that shows the effect of the addition and omission of vaporization. Figure 57 (a) shows the effect based on an isometric view of the melt pool under both conditions, and Figure 57 (b) illustrates the influence of vaporization on the cross section of the melt pool. Figure 57 (c), also from Queva et al, shows the effect of vaporization on maximum temperature and melt pool volume over time. To further elucidate the influence of vaporization and establishment of a free surface within the CFD model, Figure 58 features the cross section of the vapor cavity and its velocity and temperature profiles from Queva et al [34]. As shown, the shape of the vapor cavity is strongly influenced by the vaporization, recoil pressure, and the establishment of the vapor cavity or free surface. One of the notable behaviors seen in both figures is the velocity profiles, particularly in Figure 58, where the highest velocities are concentrated at the edge of the melt pool width, while in Figure 57 the high velocity vectors are moving along the vapor cavity. Queva et al also noted that the presence of vaporization caused the maximum temperature to plateau, as seen in Figure 57 (c). The Marangoni effect shown in these figures also resulted in the melt pool of Figure 57 (b) where the one with the presence of vaporization exhibited a narrower but slightly deeper melt geometry when compared to the melt pool lacking vaporization.

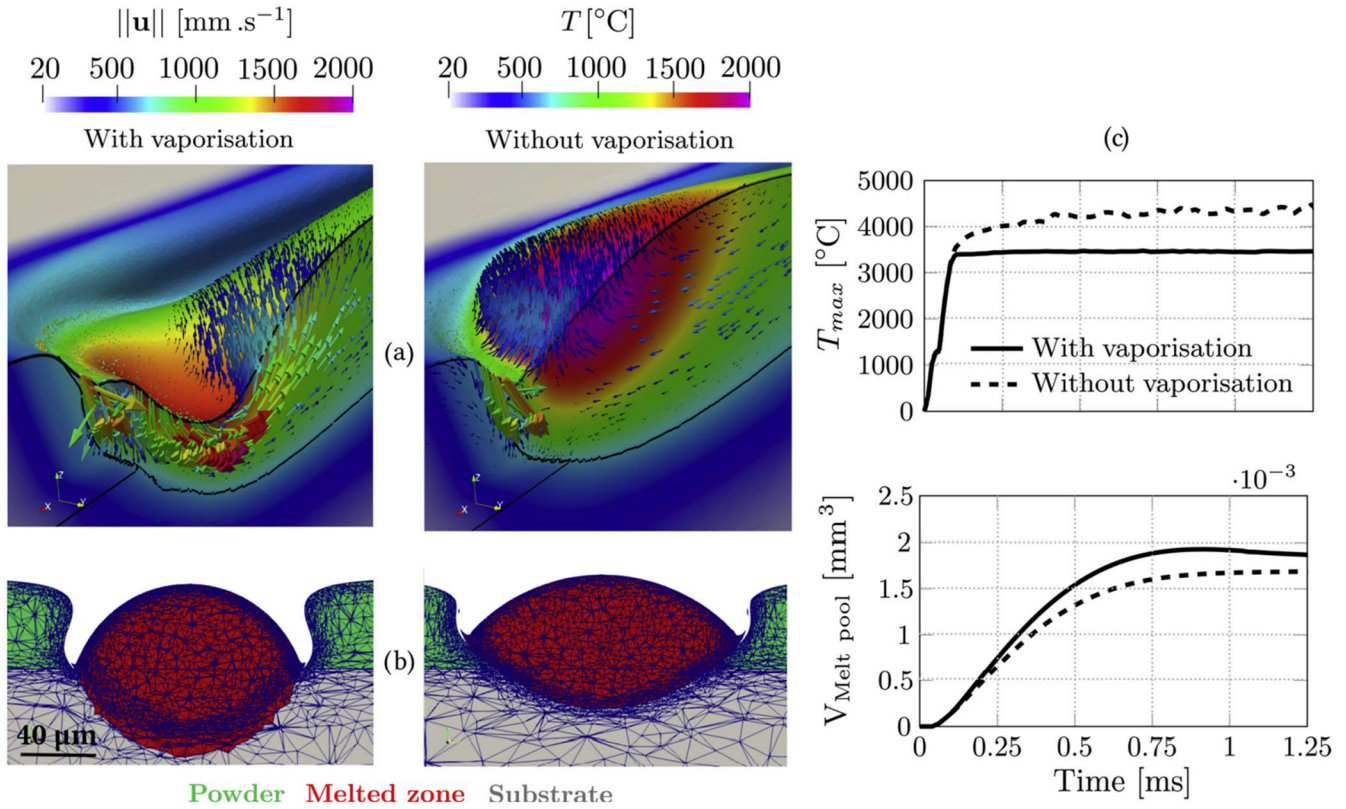


Figure 57: Effects of featuring vaporization mass loss: (a) shows an isometric view of the melt pool temperature and velocity profiles with and without vaporization; (b) shows the cross-section melt pool profile and (c) shows maximum temperature and melt pool volume over time [34].

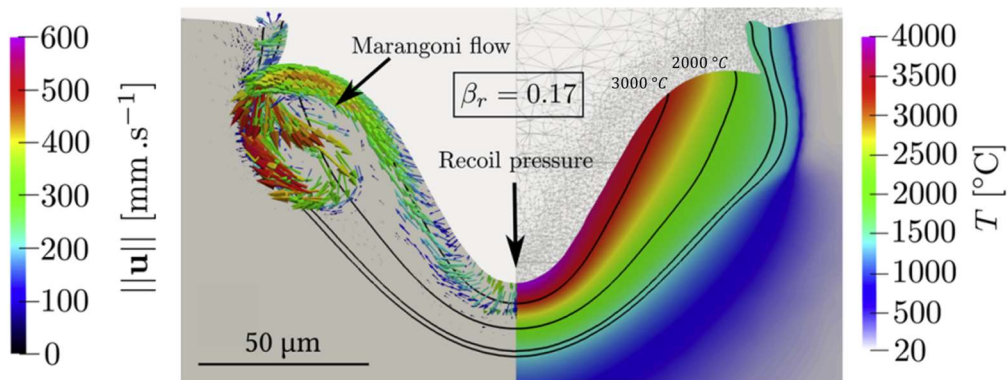


Figure 58: Cross section of the velocity (left) and temperature profiles of the vapor cavity due to evaporation and recoil pressure [34].

The IN718 melt pool measurements from the model by Queva et al were compared to the physical results obtained in the current research. The parameters Queva et al used included a laser power of 285 W

and a scan speed of 1000 mm/s with a laser diameter of 100  $\mu\text{m}$ . The powder layer thickness used was 50  $\mu\text{m}$ . Based on these parameters, the surface energy density applied to the material was 2.85 J/mm<sup>2</sup>, which is comparable to Line Number 4 (P=225 W and V=960 mm/s) of this work. These parameters resulted in a surface energy density of 2.92 J/mm<sup>2</sup>, similar to the energy density of Queva et al. The bead width and depth that were predicted by their model were 108  $\mu\text{m}$  and 43  $\mu\text{m}$ , respectively. These values were then compared with the average depth and width obtained from the physical experiments of Line Number 4 found in the entire dataset of Table 18 (bead width = 121  $\mu\text{m}$ ) and Table 17 (melt pool depth = 56  $\mu\text{m}$ ). The percent differences between the model by Queva et al and the physical experiments of this study yielded 10.7% for the width and 23.2% for the depth. Considering that parameters for both conditions were somewhat mismatched, some discrepancy was expected. It is noted that the bead width predicted by the Queva model, which included a more accurate physical representation, yielded results similar to the measured values found from this work. Although this model appeared to provide a more accurate prediction for bead width, it was also significantly more computationally intensive. According to Queva et al, their model took 32 hours for a 1 mm track with 56 cores. The model created in this study took 19 hours for 0.288 mm with 12 cores using the Rivanna high-performance computing system at the University of Virginia, which compared to Queva, was approximately two times faster. Although greater accuracy for predicting bead width requires a higher fidelity model that captures vaporization, vapor/recoil pressure, and a changing free surface, the addition of these capabilities in the model greatly increases complexity and computational time.

## 4.3 High Temperature Alloy Simulation

### 4.3.1 Database Compilation Results

The properties of interest were defined in Table 7 previously. As expected, there was scarce literature for properties of C103 and other high temperature alloys. Of those values found, they usually represented a single temperature, or at best two. For example, Lambert and Rausch reported only two values for thermal conductivity [13]. Fortunately, the properties of the elemental components of C103 were more accessible and provided, in some cases, the ability to estimate properties based on composition of the alloy. The niobium thermophysical properties were from Ishikawa and Paradis [61] for density, Chase for specific heat [62], and Mills et al for thermal conductivity [63]. For hafnium, the density equation below 2200K is from Onufriev et al[64] and Ishikawa and Paradis [61] for temperatures above 220K. The specific heat equation and constant for hafnium is based on Arblaster [64], while Onufriev et al [64] also provided data on thermal conductivity. For titanium, Mills [48] provided the density and thermal conductivity equations, while the specific heat was from Chase [62]. Ishikawa and Paradis also provided additional properties for all three elements, such as surface tension and its gradient, as well as viscosity. The melting temperature and enthalpy and vaporization temperature and enthalpy were provided by Valencia and Quested [47] and Zhang et al [65], respectively. Finally, the density functions for zirconium are from Korobenko and Savvatimskii[66]. Results of these compilations are listed Tables 19 to 22, and graphical comparisons are provided in Figures 59 to 62. During the compilation of these properties for the refractory materials, discernable patterns were observed.

Similar to Figure 23, the density values of the refractory materials were represented as a linear relationship with temperature during the solid phase. However, during the phase change to liquid, the linear relationship would shift. Also, depending upon the material, the thermal conductivity could be

represented by either a parabolic or linear relationship with temperature during the solid phase but remained constant in the liquid phase. The regression required to capture specific heat, however, was more complex. As shown in Figure 60, they are primarily composed of polynomials during the solid phase and then having a constant value at the liquid phase. Fortunately, the specific heat capacities for pure metals are readily available through NIST JANAF Tables. These tables allow for the coefficients of an equation, shown below as Equation 20 to accurately describe specific heat. In Equation 20,  $A$ ,  $B$ ,  $C$ , and  $D$  are coefficients from the JANAF Tables [42] and  $M$  is the molar mass of the element required to convert the units from J/(mol\*K) to J/(kg\*K). These tables also usually provide additional information about the melting and vaporization temperatures. NIST also provides coefficients for using Equation 20 to determine the specific heat of the liquid phase. However, it was realized that these liquid phase equations basically converge to a single value, and thus, would be treated as a constant.

$$c_p = \frac{A + B * \frac{T}{1000} + C * \left(\frac{T}{1000}\right)^2 + D * \left(\frac{T}{1000}\right)^3 + D * \left(\frac{T}{1000}\right)^{-2}}{M} \quad (20)$$

The properties of the C103 alloy listed in Table 23 were based on the patterns found during review and construction of the data based on elemental composition. It was believed that density of the elements would be represented as a series of linear equations, and that the density of C103 could be calculated as the weighted average, based on the elemental composition. The validity of this approach was determined by comparing the density of C103 calculated from its composition to the only literature value available, which was 8870 kg/m<sup>3</sup>, by Lambert et al [13]. Based on the density graph of Figure 59, the value for density from the literature was between the density of pure niobium and calculated density. The composition of 88.3% Nb, 10% Hf, and 1% Ti with a minor addition of 0.7% Zr was used for determination of density and specific heat was calculated using Thermo-Calc, a computational materials science tool which is capable of calculating other thermophysical properties, such as the solidus and liquidus temperatures and the heat of fusion. The calculations by Thermo-Calc were provided by Dr. Kang Wang of the Computational Thermodynamics and Kinetics Group under Dr. Bi-Cheng Zhou. Prior to receiving the Thermo-Calc computations, the projected specific heat was estimated using the same weighted average by composition employed for density. After receiving the results from Thermo-Calc, both approaches for determining specific heat were compared. These results are depicted in Figure 60. The data in the figure indicates that the linear relationships for specific heat within an interval between 543K to 2747K are very close between the weighted average and Thermo-Calc estimations. The projection of thermal conductivity was based on observations that the solid phase has either a linear or parabolic relationship with respect to temperature, followed by a constant value for the liquid phase., Though in some materials, such as niobium, titanium and IN718, the thermal conductivity decreases within the liquid. Wojcik provided two thermal conductivity measurements for two temperatures, 37.4 W/(m\*K) for 1073K and 42.4 W/(m\*K) at 1473K. Though only two values were available, there were sufficient to create a linear equation from room temperature to the liquidus temperature. With the three thermophysical properties estimated and compiled, the thermal diffusivity was then calculated using:

$$\alpha = \frac{k}{\rho c_p} \quad (21)$$

where  $\alpha$  is thermal diffusivity (in the units of  $m^2/s$ ),  $k$  is thermal conductivity,  $\rho$  is density, and  $c_p$  is specific heat. The thermal diffusivity of each material that composes the database is visualized in Figure 62. Relative to IN718, all other materials within the database are shown to have higher thermal diffusivity. Based on this observation, the temperature profile for C103 would be anticipated to be very different than the IN718 alloy, given the same energy density. This would be based on the higher thermal diffusivity, as well as the higher solidus and liquidus temperatures for C103, which are at least 1000K higher than of IN718.

Table 19: Niobium properties

<b>Niobium</b>		
<b>Property</b>	<b>Temperature Range [K], Reference</b>	<b>Equation/Value</b>
Density [kg/m <sup>3</sup> ]	[61]	$\rho = -0.38 * T + 8764.32$
Specific Heat Capacity [J/(kg*K)]	$T < 2741$ [62]	$c_p = \frac{\left( 22.014 + 9.89 * \left( \frac{T}{1000} \right) - \left( 5.65 * \left( \frac{T}{1000} \right)^2 \right) + \left( 1.76 * \left( \frac{T}{1000} \right)^3 \right) + \left( \frac{0.021839}{\left( \frac{T}{1000} \right)^2} \right) \right)}{0.09291}$
	$T \geq 2741$ [62]	$c_p = 360.25$
Thermal Conductivity [W/(m*K)]	[63]	$k = 61.466968 + 0.008988 * T$
	[63]	$k = 66$
<b>Constants</b>		
Viscosity [kg/(m*s)]		0.0045 [61]
Heat of Fusion [J/kg]		315,400 [47]
Heat of Vaporization [J/kg]		692,750 [64]
Melting Temperature [K]		2741 [47]
Vaporization Temperature [K]		5130 [64]
Surface Tension at Melting Point [N/m]		1.937 [61]
Marangoni coefficient/Surface Tension Gradient [N/(m*K)]		-0.00021 [61]

Table 20: Hafnium properties

Hafnium		
Property	Temperature Range [K], Reference	Equation/Value
Density [kg/m <sup>3</sup> ]	$T < 2200$ [65]	$\rho = \frac{13310}{1 + 3\{[6.58 \times 10^{-6}(T - 293)] - [3.34 \times 10^{-10}(T - 293)^2] + [5.75 \times 10^{-13}(T - 293)^2]\}}$
	$T \geq 2200$ [61]	$\rho = -0.525 * T + 13135.564$
Specific Heat Capacity [J/(kg*K)]	$T < 2500$ [67]	$c_p = \frac{\left( 23.92 + (7.016 \times 10^{-3}T) - \left( \frac{28746.4}{\left( \frac{T}{1000} \right)^2} \right) \right)}{0.09291}$
	$T \geq 2500$ [67]	$c_p = 203.14$
Thermal Conductivity [W/(m*K)]	$T < 2500$ [65]	$k = 26.05 - (0.01548T) + ((8.957 \times 10^{-6}(T)^2) + \left( \frac{845.8}{T} \right))$
	$T \geq 2500$ [65]	$k = 40.84$
Constants		
Viscosity [kg/(m*s)]		0.0052 [61]
Heat of Fusion [J/kg]		134850 [47]
Heat of Vaporization [J/kg]		60400 [64]
Melting Temperature [K]		2500 [47]
Vaporization Temperature [K]		4964 [64]
Surface Tension at Melting Point [N/m]		1.614 [61]
Marangoni coefficient/Surface Tension Gradient [N/(m*K)]		-0.00017 [61]

Table 21: Titanium properties

Titanium		
Property	Temperature Range [K], Reference	Equation/Value
Density [kg/m <sup>3</sup> ]	$T \leq 1958 K$ [48]	$\rho = 4540 - 0.15 * (T - 298)$
	$T \leq 1958 K$ [48]	$\rho = 4140 - 0.225 * (T - 1958)$
Specific Heat Capacity [J/(kg*K)]	$T < 1958 K$ [62]	$c_p = \frac{\left( 22.62 + (18.99 * \left( \frac{T}{1000} \right)) - \left( 18.19 * \left( \frac{T}{1000} \right)^2 \right) + \left( 1.76 * \left( \frac{T}{1000} \right)^3 \right) + \left( \frac{0.021839}{\left( \frac{T}{1000} \right)^2} \right) \right)}{0.09291}$
	$T > 1958 K$ [62]	$c_p = 986.84$
Thermal Conductivity [W/(m*K)]	$T < 2100 K$ [48]	$k = 0.0131T + 5.549$
	$T \geq 2100 K$ [48]	$k = 31$
Constants		
Viscosity [kg/(m*s)]		0.0044 [61]
Heat of Fusion [J/kg]		295000 [47]
Heat of Vaporization [J/kg]		426500 [64]
Melting Temperature [K]		1958 [47]
Vaporization Temperature [K]		3631 [64]
Surface Tension at Melting Point [N/m]		1.557 [61]
Marangoni coefficient/Surface Tension Gradient [N/(m*K)]		-0.00023 [61]

Table 22: Zirconium properties

Zirconium		
Property	Temperature Range [K]	Equation/Value
Density [kg/m <sup>3</sup> ]	$T < 2200$ [66]	$\rho = 6340 - 0.15 * (T - 2128)$
	$T \geq 2200$ [66]	$6844.51 - (0.610 * T) + (2.050 \times 10^{-4} T^2) - (4.478 \times 10^{-8} T^3) + (3.264 \times 10^{-12} T^4)$

Table 23: Projected properties of C103 used for the simulation

C103		
Property	Temperature Range [K], Reference	Equation/Value
Density [kg/m <sup>3</sup> ]		Composition based (88.3%Nb, 10%Hf, 1%Ti, 0.07%Zr)
Specific Heat Capacity [J/(kg*K)]	$T < 543$	$c_p = 196.27 + 0.249 * T$
	$543 \leq T < 2747$	$c_p = 0.0705 * T + 222.87$
	$T \geq 2747$	$c_p = 434.96$
Thermal Conductivity [W/(m*K)]	$T < 2677$ [7]	$k = 0.0125 * T + 24$
	$T \geq 2677$	$k = 57.46$
Constants		
Viscosity [kg/(m*s)]		0.0052 (Nb)
Heat of Fusion [J/kg]		204338 [Thermo-Calc]
Heat of Vaporization [J/kg]		N/A
Solidus Temperature [K]		2622 [Thermo-Calc]
Liquidus Temperature [K]		2677 [Thermo-Calc]
Vaporization Temperature [K]		5000 (assumed)
Surface Tension at Melting Point [N/m]		1.937 (Nb)
Marangoni coefficient/Surface Tension Gradient [N/(m*K)]		-0.00021 (Nb)

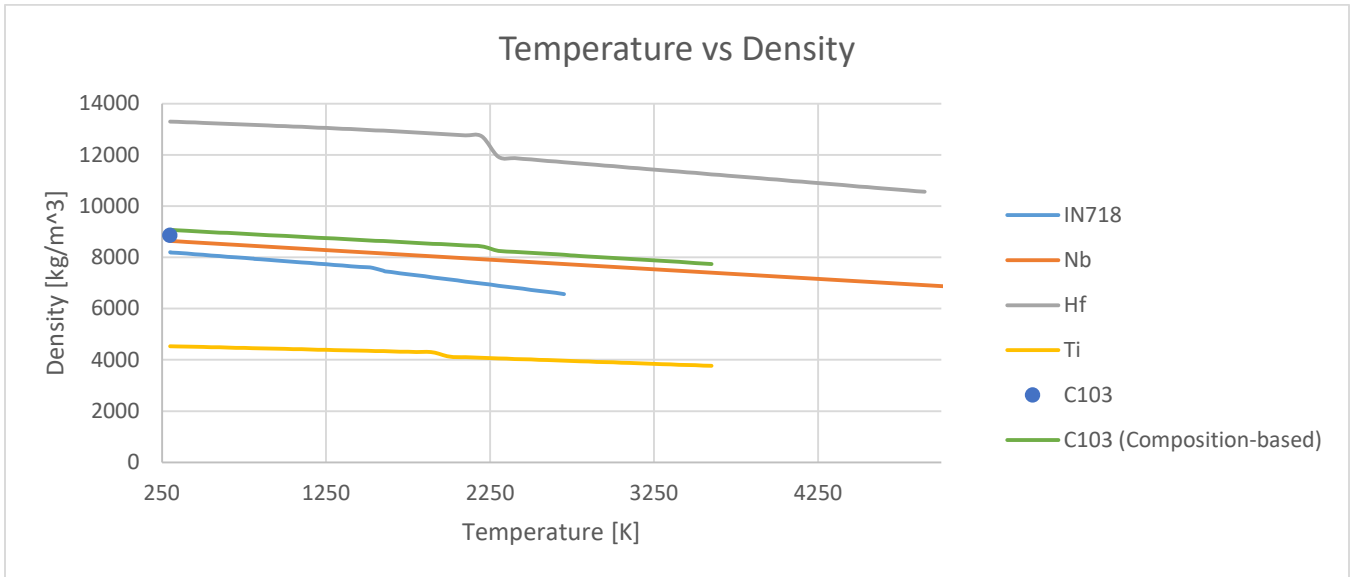


Figure 59: Density vs temperature for IN718, C103, Nb, Hf and Ti.

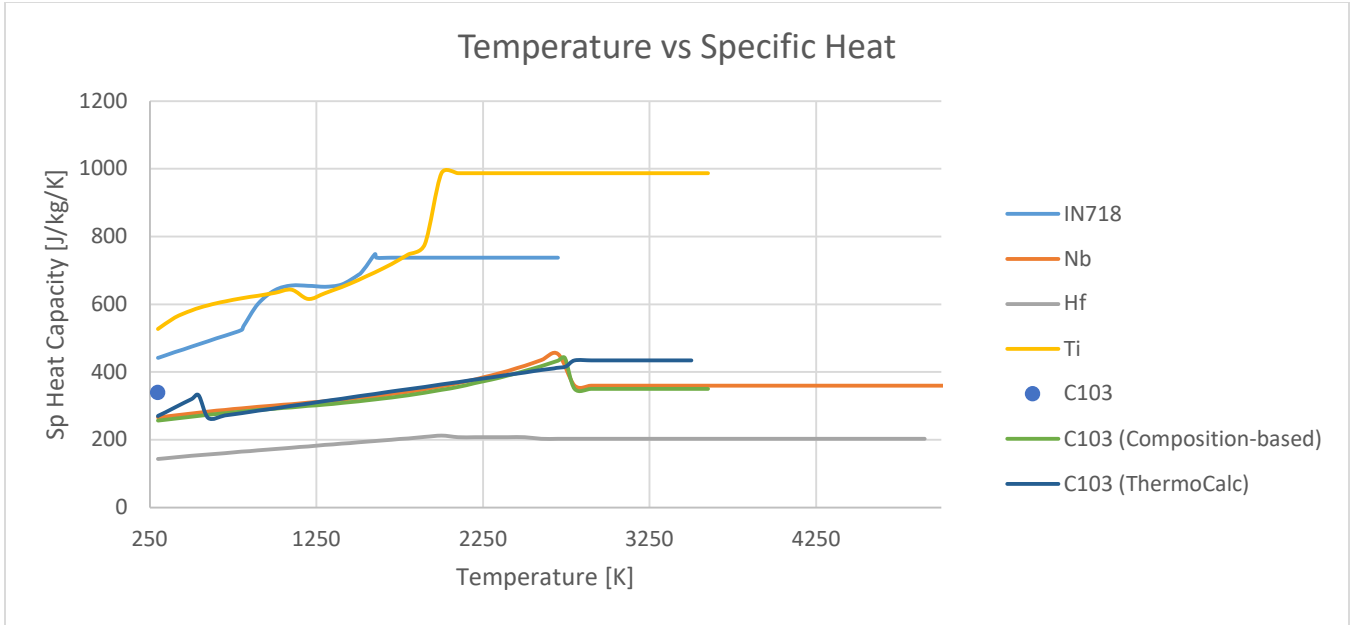


Figure 60: Specific heat vs temperature for IN718, C103, Nb, Hf and Ti.

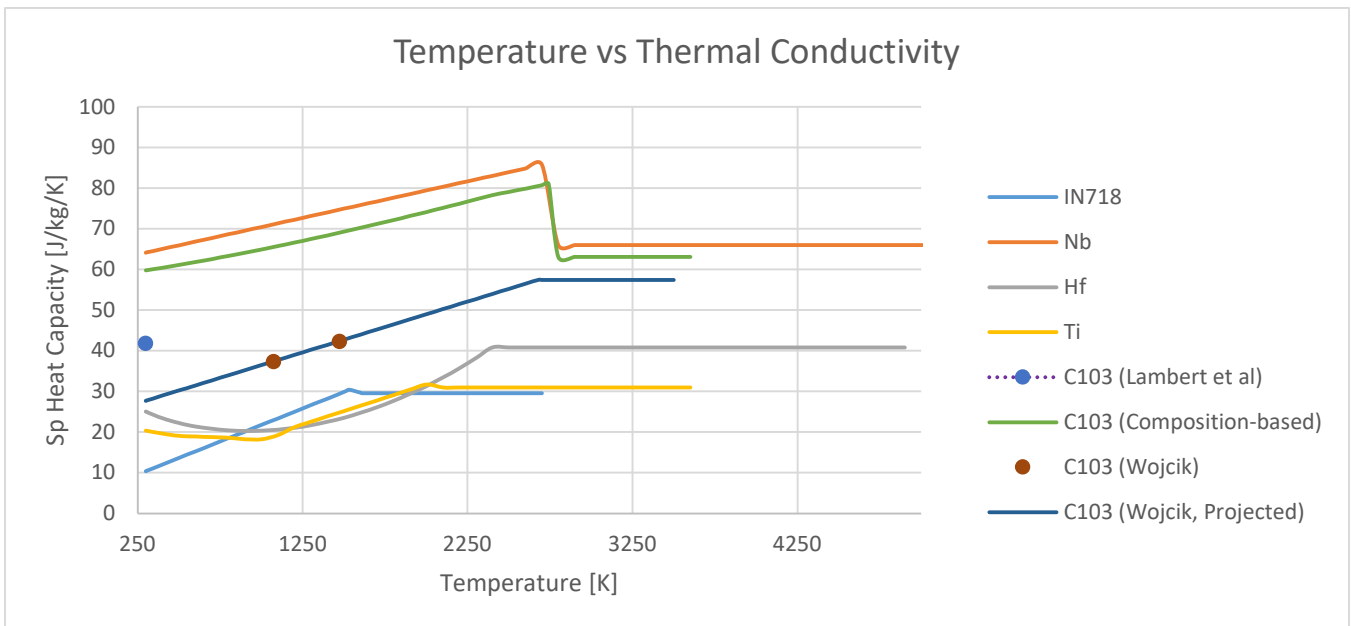


Figure 61: Thermal conductivity vs temperature for IN718, C103, Nb, Hf and Ti.

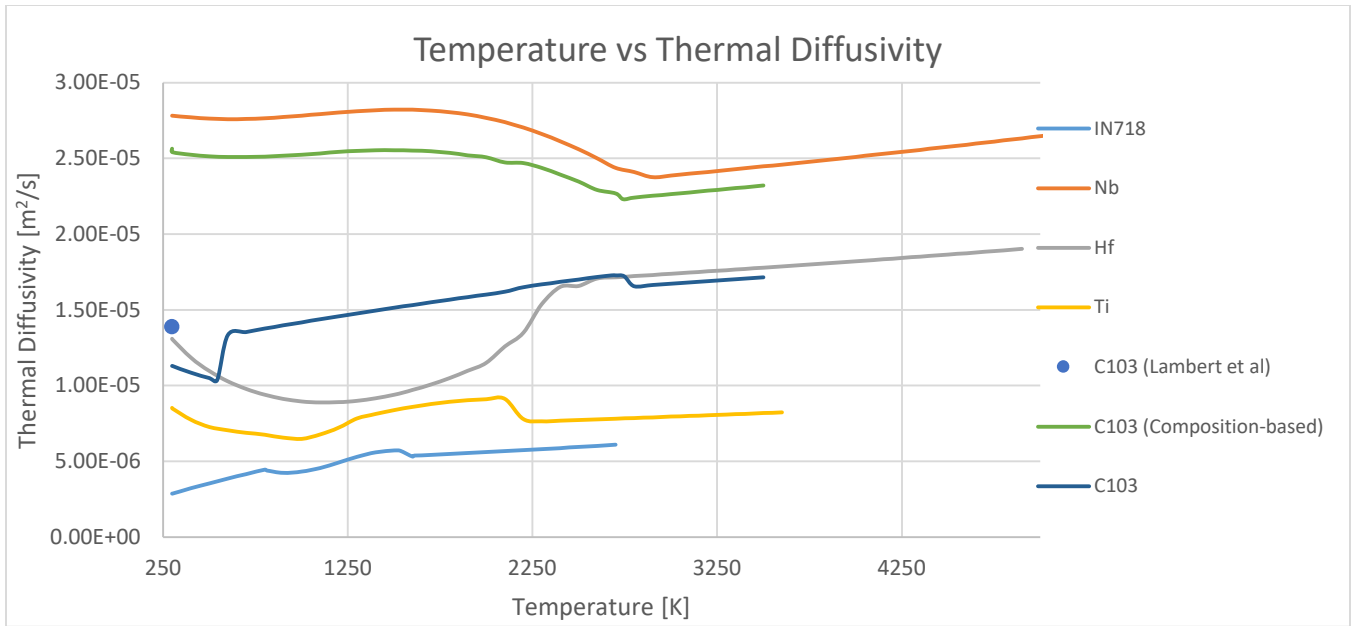


Figure 62: Graph of thermal diffusivity functions and values for IN718, C103, Nb, Hf and Ti.

#### 4.3.2 Simulation of C103 Based on Projected Thermophysical Data

For the simulation of the melt pool for C103, the properties listed in Table 23 were used within ANSYS Fluent model to simulate the response of the material during processing. However, the laser absorptivity, convective heat transfer coefficient, and emissivity coefficients from the virtual IN718 simulation were retained. Due to the lack of information regarding vaporization temperature and latent heat, the evaporative cooling flux was omitted in this simulation. The longitudinal and cross-sectional views for the C103 and IN718 are provided in Figures 63 and 64. A clear difference between the melt pool geometries of both materials was evident with the C103 having a shallower depth and shorter length of the pool. The bead width measurements, even if proven inaccurate for IN718, were shown to be equivalent for both materials when the melt pool depth had sufficient penetration. Both materials exhibited the same velocity profiles in the longitudinal view, though the melt pool of C103 occupies a smaller area having a backward melt pool convective loop in the rear. The velocity vectors from the cross-sectional view for appear to show smaller vectors for the C103 alloy. Additionally, the melt pool profile from top surface to the powder-bulk interface for C103 has a more gradual narrowing, whereas the melt pool of IN718 immediately narrows. This difference could be rooted in the higher thermal diffusivity of C103.

The measurements for melt pool depth and bead width are listed in Table 24. Figure 65 also provides a scatter plot for the melt pool depth between C103 and the experimental averages and simulation results of IN718. One noticeable observation of Figure 65 is that the differences between the simulated melt pool depths of IN718 and C103 appear to be closer at lower energy density. Another observation from this figure is that depth of penetration for the C103 appears to be shifted when compared to IN718 at higher surface energy densities. At energy densities above 3.5 J/mm<sup>2</sup>, the difference between the IN718 and C103 appears to be constant at 25 μm.

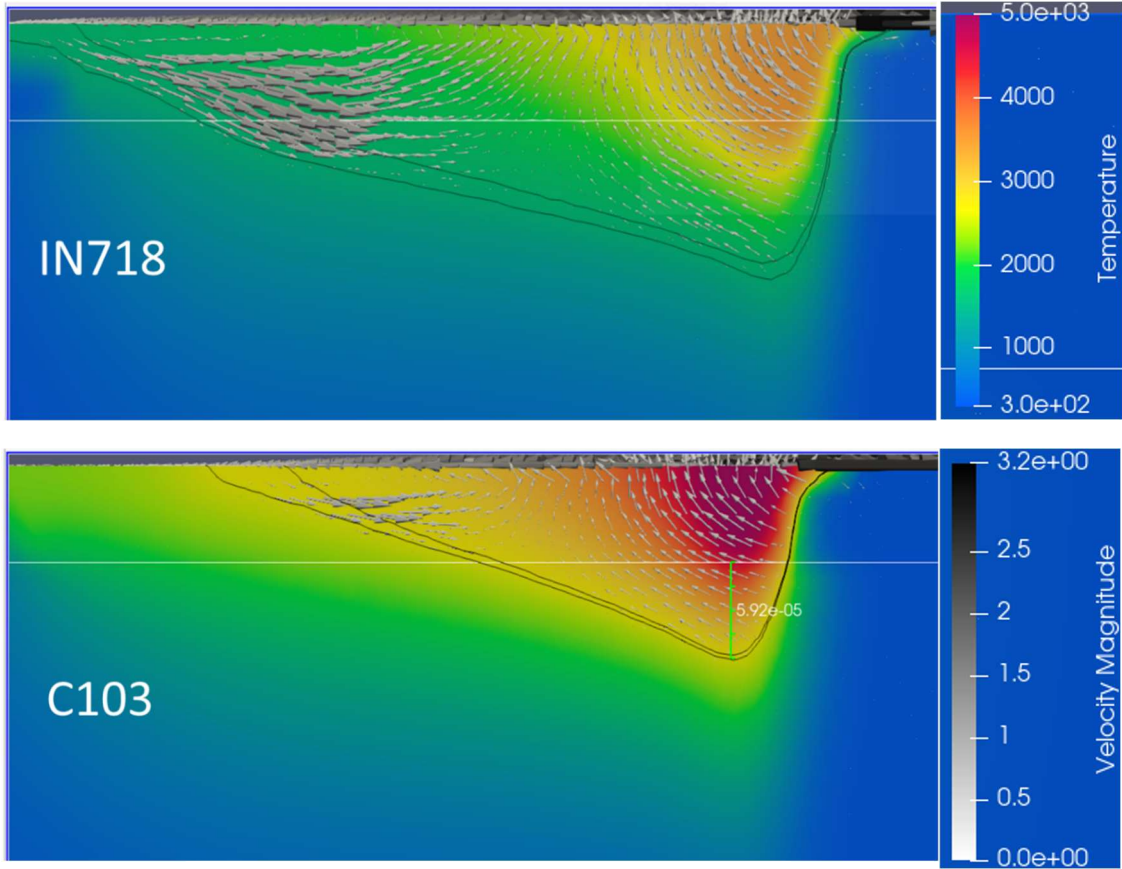


Figure 63: Longitudinal view of simulation results for C103 and IN718 at  $450\mu s$ .

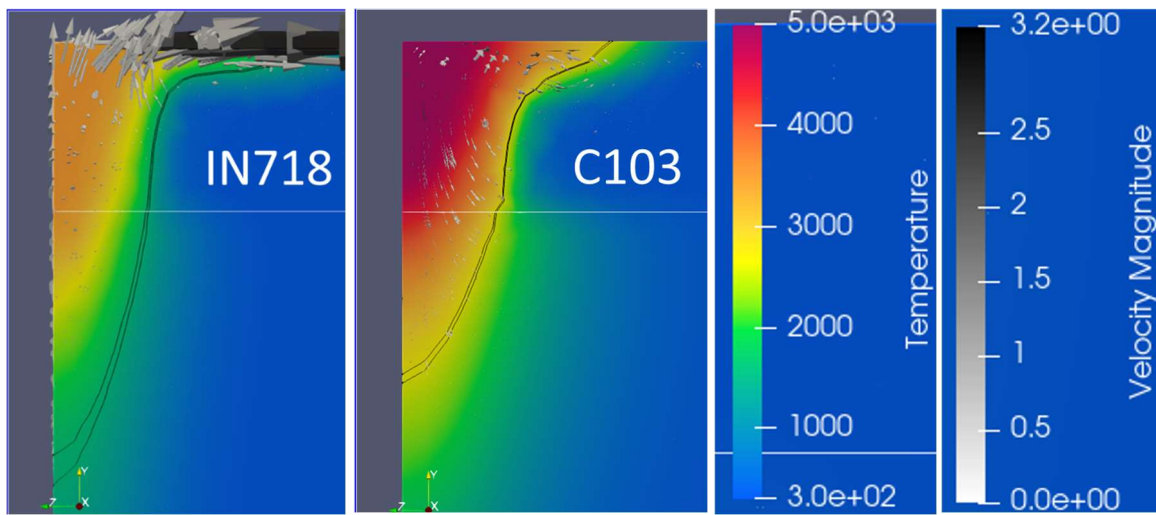


Figure 64: Cross-sectional view of simulation results for C103 and IN718 at  $450\mu s$ .

Table 24: C103 simulation results, sorted by surface energy density.

Line Number	Laser Power (W)	Scan Speed (mm/s)	Surface Energy Density [J/mm <sup>2</sup> ]	Melt Pool Depth (μm)	Bead Width (μm)
7	225	1160	2.42	30	50
4	225	960	2.93	30	50
8	285	1160	3.07	47	64
1	225	760	3.7	50	74
5	285	960	3.71	57	78
9	345	1160	3.72	61	76
6	345	960	4.49	72	86
2	285	760	4.69	70	88
3	345	760	5.67	84	96

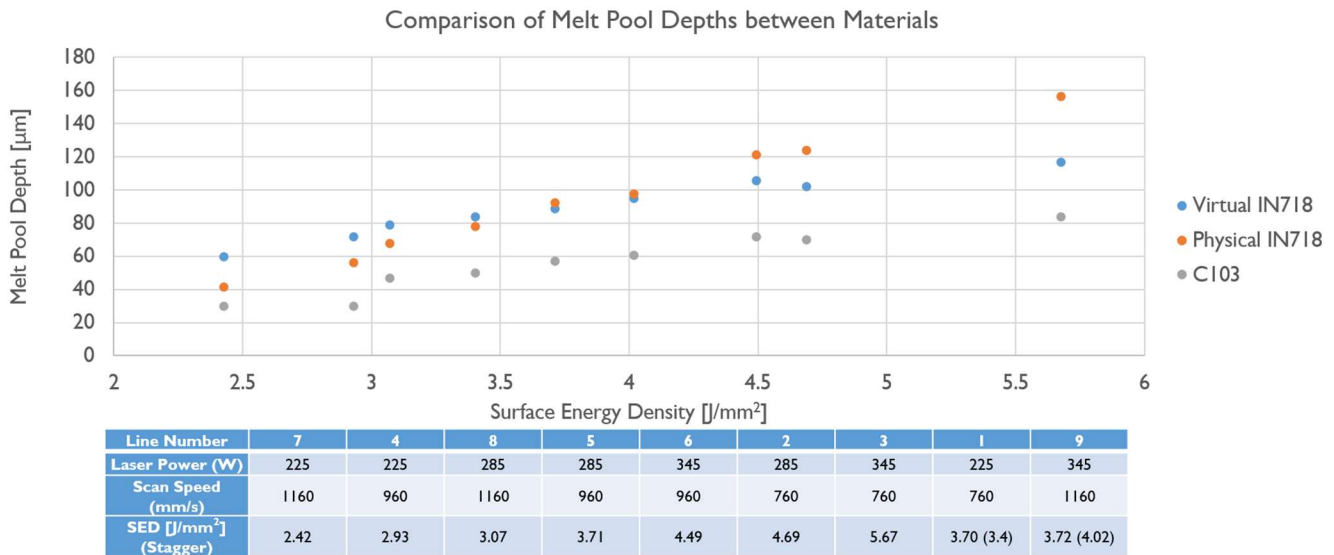


Figure 65: Comparison between melt pool depth measurements for IN718 and C103.

### 4.3.3 Discussion on the Database and C103 Melt Pool Geometry

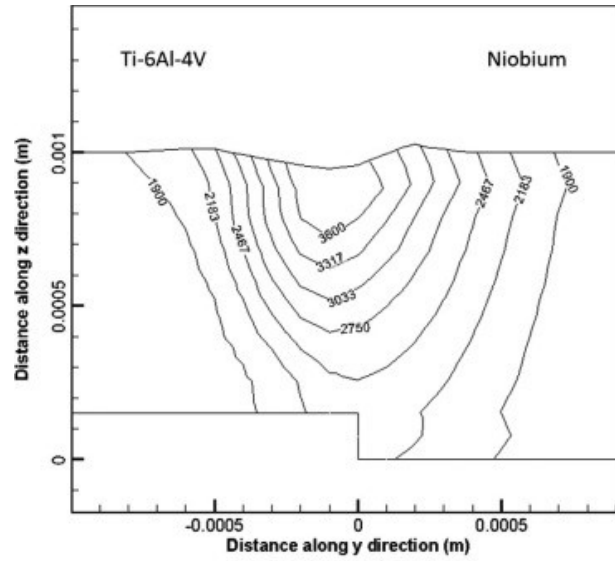
Because the C103 properties were based on limited data and assumptions using its elemental components, more sophisticated methods of obtaining temperature-dependent material properties were briefly sought. The equations and constants listed in Tabled 19 to 24 were compiled into a spreadsheet with the format inspired by Akbari et al. Their project involved creating MeltPoolNet, a machine learning algorithm to predict viable parameters to avoid common defects, such as keyhole porosity and lack of fusion, which were goals akin to this study. Akbari et al provides the machine learning algorithm training data by compiling literature results on additive manufacturing (AM) research and noting features, such as primary process parameters, thermophysical properties, absorption coefficient, hatch spacing and layer thickness [68]. This study diverges from the approach of Akbari et al by focusing on the temperature

dependency of the thermophysical properties as inputs for physics-based simulations. Akbari et al does list thermophysical properties but their database does not include temperature dependence. It is hoped that in the future the database constructed in this study could be utilized by machine learning models to deduce gaps in the literature for material properties for novel materials.

Finding and constructing the algorithms that have the means to achieve such goals are unfortunately out of the scope for this study, but there were some leads. Besides Akbari et al, Verpoort et al provides a potential useful approach termed imputation, which is the process involving substitution of missing data entries [69]. Kauwe et al used machine learning to predict temperature dependency of specific heat [70]. However, one must also be cognizant that machine learning, in general, requires a certain threshold of data to, both, train and test such models. For example, Akbari et al used regression models, such as random Gaussian Process and Neural Networks with a sample size of more than 1700 among 24 alloys. The database created for this study only contained properties for IN718 and elemental components of C103. If the database must be used for these algorithms, it needs to be populated for properties of the components of IN718, as well as common AM materials, such Ti-6Al-4V and 316L.

Regarding the simulation of C103, the deficiency with modeling bead width prevented the use of the melt-pool-depth-to-bead-width ratio for identifying primary process parameters that could result in lack of fusion or keyhole porosity. If the ratio was available, Dilip et al suggest parameters that could penetrate two to three times the powder layer thickness for ratios of between 0.37 and 0.6 [71]. This suggestion was used to examine the current results, despite lacking information for melt-pool-depth-to-bead-width. Unfortunately, all the parameters used for the C103 simulations provided insufficient depth to ensure properly fused layers. Based on the energy density values, a new set of primary process parameters should be tested to find the desired depth range. These new parameter combinations must yield higher surface energy densities. However, it should also be noted that the laser absorption used for simulations of the IN718 and C103 were the same. If C103 or pure niobium has a higher reflectivity than IN718, the suggested energy densities must be multiplied accordingly to account for the differences in absorptivity.

To further support the recommendation of using a higher surface energy density for fabrication of C103 parts, a thorough literature review of either the laser powder bed fusion or laser welding of niobium or niobium-based alloy was conducted. Unfortunately, there was scarce literature available for these materials. In the case of pure niobium, the only literature available involved laser welding of niobium with Ti-6Al-4V alloy. Liang et al utilized a pulsed laser for welding Ti-6Al-4V and niobium, and their results are shown in Figure 66 [72]. The isotherms in this figure showed a wider distribution of temperature in the niobium plate. To contextualize this, the melting temperature of niobium is 2741K while the melting temperature for Ti-6Al-4V, according to Jamshidinia et al, is 1923 K [73]. Therefore, based on the temperature distribution in Figure 66, the niobium plate should have a smaller melt pool than the titanium-based alloy. This is further corroborated by Torkamany et al, who applied laser pulses onto niobium and Ti-6Al-4V plates separately [74]. As demonstrated by Figure 67, the niobium melt pool is significantly smaller than the titanium-based alloy.



measure the melt pool image, which was 97  $\mu\text{m}$ . Guo et al, on the other hand, provided several melt pools with their niobium-based alloy, Nb-37Ti-13Cr-2Al-1Si. These are shown in Figure 69 [78]. Although this source did not provide the thermophysical properties of the alloy, the melt pools in Figure 69 were also processed through ImageJ. Only the select melt pools that showed penetration were measured and plotted, which are shown in Figure 70. This figure not only includes the depth measurements from, both, virtual and physical experiments of IN718, C103, Nb521, and Nb-37Ti-13Cr-2Al-1Si, but also Ti-6Al-4V from Dilip et al [71]. Figure 70 includes trendlines of the data to better discern differences between the melt pools of each alloy. Since not all the sources for the niobium-based alloys state the laser beam diameter for their respective experiments, an alternative energy value based on laser power and scan speed must be used. In this case, it would be surface energy density based on the powder layer thickness from Kurzynowski et al [79], whereas, Equation 1 was based on the laser beam radius. The x-axis value in Figure 70 also substitutes  $2r_0$  with  $y_0$ , the powder layer thickness. This calculation is shown below:

$$\text{Surface Energy Density by Powder Layer Thickness} \left[ \frac{J}{\text{mm}^2} \right] = \frac{P}{v * y_0} \quad (22)$$

Table 25: Ti-6Al-4V properties

Ti-6Al-4V		
Property	Temperature Range [K], Reference	Equation/Value
Density [kg/m <sup>3</sup> ]	$T < 1923 \text{ K}$ [74]	$\rho = (-0.154 * (T - 298)) + 4420$
	$T \geq 1923 \text{ K}$ [74]	$\rho = (-0.68 * (M27 - 1973)) + 3920$
Specific Heat Capacity [J/(kg*K)]	$T < 1923 \text{ K}$ [74]	$c_p = 0.18T + 412.179$
	$T \geq 1923 \text{ K}$ [74]	$c_p = 830$
Thermal Conductivity [W/(m*K)]	[47]	$k = -0.797 + 0.0182T - 0.000002T^2$
	[47]	$k = 33.4$
	[47]	$k = 34.6$
Constants		
Viscosity [kg/(m*s)]		0.049 [78]
Heat of Fusion [J/kg]		2.86E+05 [34]
Heat of Vaporization [J/kg]		8.89E+06 [34]
Solidus Temperature [K]		1877 [73]
Liquidus Temperature [K]		1923 [73]
Vaporization Temperature [K]		4473 [34]
Surface Tension at Melting Point [N/m]		1.42 [78]
Marangoni coefficient/Surface Tension Gradient [N/(m*K)]		-2.60E-04 [73]

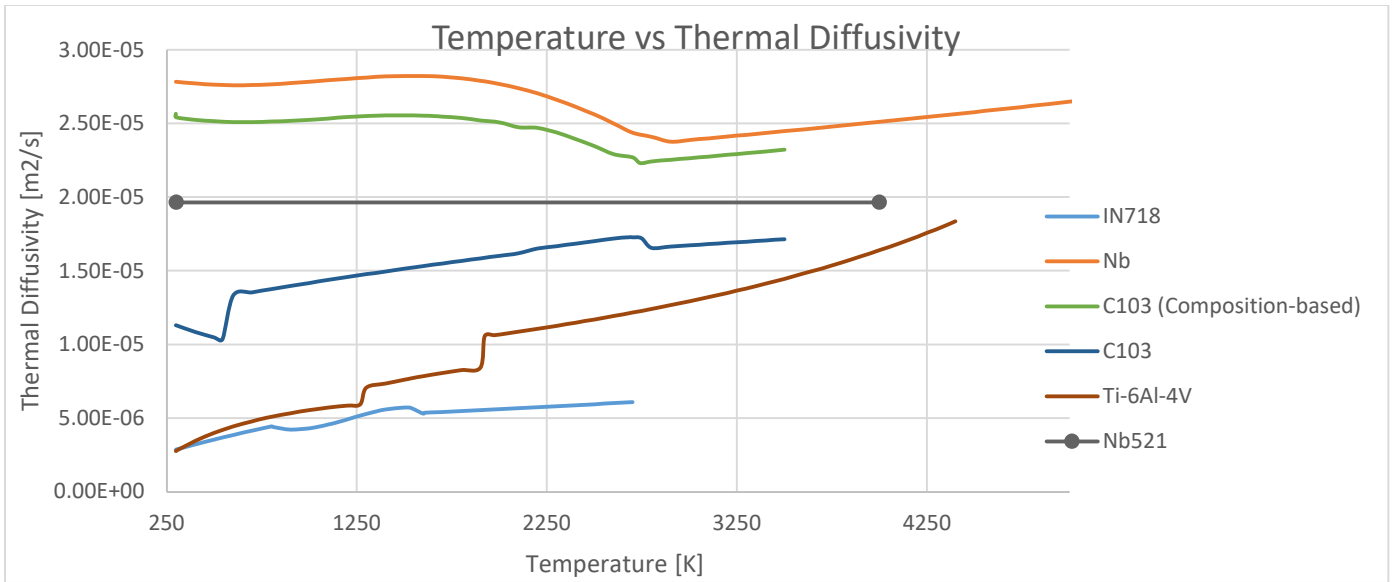


Figure 68: Thermal diffusivity plots of common additive manufacturing alloys and niobium and its alloys

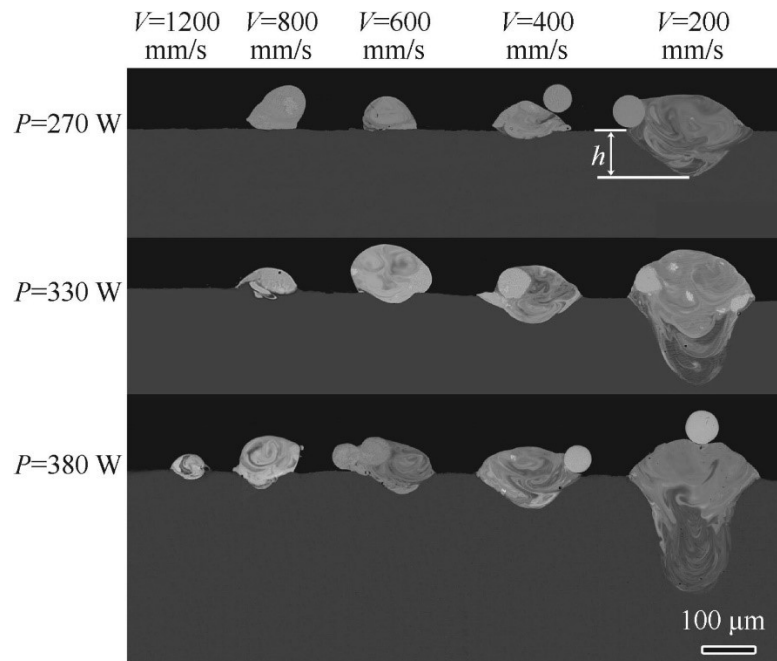


Figure 69: Melt pool geometry for Nb-37Ti-13Cr-2Al-1Si from Guo et al [78].

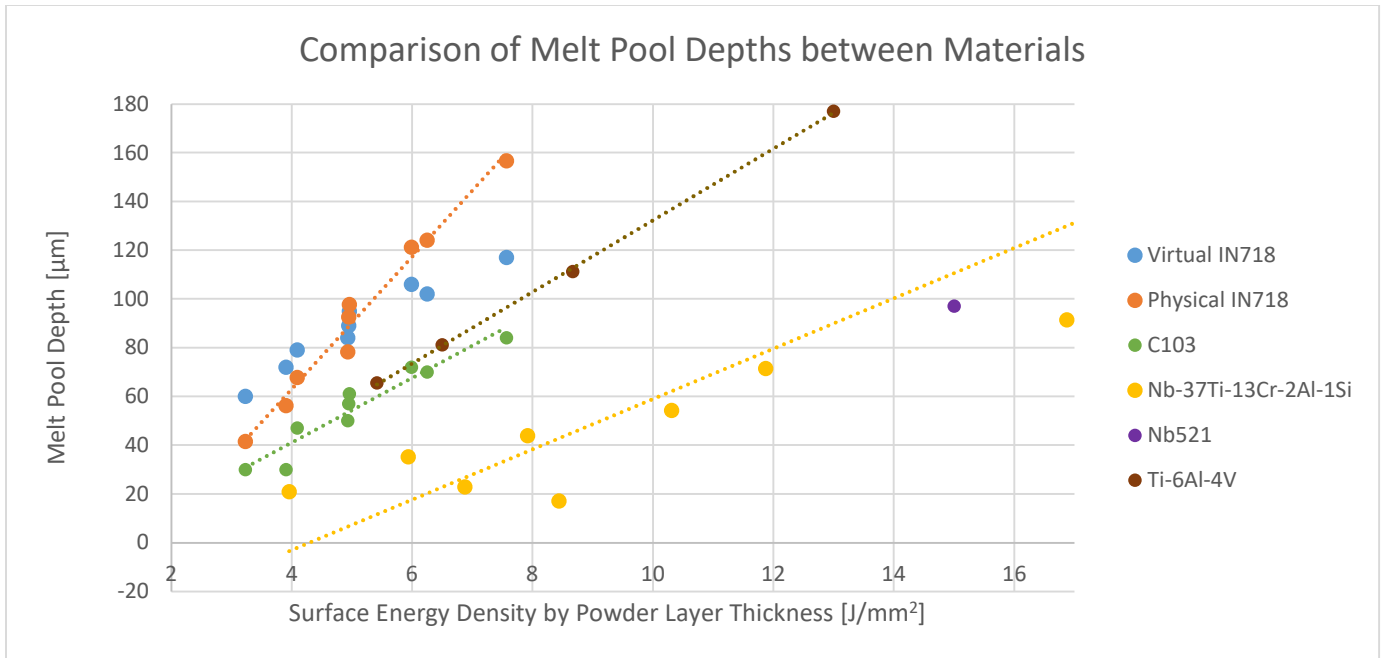


Figure 70: Plot of melt pool depths between different alloys

Based on data from laser welding of Liang et al and Torkamany et al, heat appears to diffuse at a higher rate for niobium resulting into wider distribution of isotherms at the niobium plate than of the titanium-based alloy. This, along with the higher melting temperatures, results in a smaller melt pool than that of Ti-6Al-4V. With the three thermophysical properties of the titanium-based alloy, the thermal diffusivity of Ti-6Al-4V was found to be higher than IN718 but lower than pure-niobium and its alloys, such as C103 and Nb521. The thermal diffusivity comparisons also correlate with the melt pool measurements in Figure 70, where all the niobium-based alloys, Nb521 and Nb-37Ti-13Cr-2Al-1Si, are shown to have shallower melt pools than IN718 at approximately the same surface energy densities. It should also be noted that Nb521 has a higher niobium percentage (92% Nb), while Nb-37Ti-13Cr-2Al-1Si has significantly lower percentage (47% Nb). Therefore, it can be safely assumed that C103 will have a lower melt pool depth than either common additive manufacturing alloys, IN718 and Ti-6Al-4V.

## Chapter 5: Conclusions

Physical experimentation and virtual simulations were conducted to explore and define relationships for melt pool geometries as a function of primary process parameters and powder size distributions for high temperature alloys within the powder bed fusion process. Detailed characterization was conducted on specimens produced during the physical experimentation and was used for validation of the physics-based model. The results of the characterization were analyzed using various statistical methods to define relationships between governing melt pool geometry. In addition, the physics-based

model developed for virtual simulations was utilized to gain insight into the phenomena responsible for governing melt pool geometry. Shown below are conclusions resulting from this work.

- 1) Physical experimentation and virtual simulations confirmed the direct influence of the primary process parameters of laser power and scan speed on melt pool depth with the nickel-based alloy, IN718. Increasing power or decreasing scan speed contributed to an increase in melt pool depth. In addition, physical experiments demonstrated a direct correlation between powder size and melt pool depth; whereas, a larger mean powder diameter generally resulted in increased depth of melting. From the virtual experimentation, it was also observed that a smaller attenuation coefficient resulted in greater melt pool depth. A potential extension of these observations indicates that increasing powder size distribution results in a reduction in the attenuation coefficient and a deeper energy absorption within the powder layer.
- 2) Physical experiments showed greater variability of the melt pool depth with finer powder size distribution with IN718. This observation was based on statistical analysis of the data that included graphical interpretation of boxplots and dot plots, as well as linear regression and analysis of variance. This indicates that coarser powder size could be used to reduce variability in melt pool depth.
- 3) Physical experimentation and virtual simulations did not provide a definitive relationship between primary process parameters and bead width for IN718, which hampered the accurate description of the overall melt pool geometry for this alloy. Virtual experimentation indicated that accurate depiction of bead width required a greater representation of the physical phenomena i.e., vaporization, recoil pressure, and formation of the vapor cavity. If virtual experiments are to be used to define optimal parameters that reduces the likelihood of defects, such as lack of fusion and keyhole porosity, greater fidelity of the physics-based models are required.
- 4) Virtual simulation determined that the niobium-based, refractory alloy, C103, displayed shallower melt pool depth when compared to the nickel-based alloy. A review of the available literature regarding the projected properties of C103 indicated the alloy to have higher thermal conductivity, marginal higher density, and a significantly lower specific heat throughout the temperature range used for evaluation within the model. The combination of these properties indicates the refractory alloy to have a higher thermal diffusivity when compared to IN718. It is anticipated that the higher thermal diffusivity, in conjunction with the higher melting temperatures, of the refractory alloy would result in lower melt pool depth when compared to IN718. This could result in the possibility of greater lack of fusion defects; thus, this material requires higher energy densities to ensure sufficient fusion between layers and to minimize lack of fusion defects. If the hypothesis that higher powder size distribution results in a greater penetration and less variability, which was based on the physical experiments of IN718, larger powder size for C103 could also be used to offset this potential deficiency. This suggestion requires further confirmation with further experiments about the influence of powder size distributions on the additive manufacturing process.

## Bibliography

- [1] S. Liu and Y. C. Shin, “Additive manufacturing of Ti6Al4V alloy: A review,” *Materials & Design*, vol. 164, p. 107552, 2019, doi: <https://doi.org/10.1016/j.matdes.2018.107552>.
- [2] E. Hosseini and V. A. Popovich, “A review of mechanical properties of additively manufactured Inconel 718,” *Additive Manufacturing*, vol. 30, p. 100877, 2019, doi: <https://doi.org/10.1016/j.addma.2019.100877>.
- [3] S. Ivanov, M. Gushchina, A. Artinov, M. Khomutov, and E. Zemlyakov, “Effect of Elevated Temperatures on the Mechanical Properties of a Direct Laser Deposited Ti-6Al-4V,” *Materials*, vol. 14, no. 21, Art. no. 21, Jan. 2021, doi: 10.3390/ma14216432.
- [4] N. R. Philips, M. Carl, and N. J. Cunningham, “New Opportunities in Refractory Alloys,” *Metall Mater Trans A*, vol. 51, no. 7, pp. 3299–3310, Jul. 2020, doi: 10.1007/s11661-020-05803-3.
- [5] Y. Zhang *et al.*, “Microstructures and properties of high-entropy alloys,” *Progress in Materials Science*, vol. 61, pp. 1–93, Apr. 2014, doi: 10.1016/j.pmatsci.2013.10.001.
- [6] S. Zhang, B. Lane, J. Whiting, and K. Chou, “On thermal properties of metallic powder in laser powder bed fusion additive manufacturing,” *Journal of Manufacturing Processes*, vol. 47, pp. 382–392, Nov. 2019, doi: 10.1016/j.jmapro.2019.09.012.
- [7] C. C. Wojcik and W. Chang, “Thermomechanical processing and properties of niobium alloys,” p. 11.
- [8] T. Griemsmann, A. Abel, C. Hoff, J. Hermsdorf, M. Weinmann, and S. Kaierle, “Laser-based powder bed fusion of niobium with different build-up rates,” *Int J Adv Manuf Technol*, vol. 114, no. 1, pp. 305–317, May 2021, doi: 10.1007/s00170-021-06645-y.
- [9] C. A. Terrazas *et al.*, “Fabrication and characterization of high-purity niobium using electron beam melting additive manufacturing technology,” *Int J Adv Manuf Technol*, vol. 84, no. 5, pp. 1115–1126, May 2016, doi: 10.1007/s00170-015-7767-x.
- [10] O. Mireles, O. Rodriguez, Y. Gao, and N. Philips, “Additive Manufacture of Refractory Alloy C103 for Propulsion Applications,” in *AIAA Propulsion and Energy 2020 Forum*, American Institute of Aeronautics and Astronautics, 2020. doi: 10.2514/6.2020-3500.
- [11] V. V. Satya Prasad, R. G. Baligheid, and A. A. Gokhale, “Niobium and Other High Temperature Refractory Metals for Aerospace Applications,” in *Aerospace Materials and Material Technologies : Volume 1: Aerospace Materials*, N. E. Prasad and R. J. H. Wanhill, Eds. Singapore: Springer, 2017, pp. 267–288. doi: 10.1007/978-981-10-2134-3\_12.
- [12] H. Peng, F. Gao, and W. Hu, “DESIGN, MODELING AND CHARACTERIZATION OF TRIPLY PERIODIC MINIMAL SURFACE HEAT EXCHANGERS WITH ADDITIVE MANUFACTURING,” presented at the Solid Freeform Fabrication Symposium, Aug. 2019.

- [13] J. B. Lambert, “Refractory Metals and Alloys,” in *Properties and Selection: Nonferrous Alloys and Special-Purpose Materials*, ASM Handbook Committee, Ed. ASM International, 1990, pp. 557–585. doi: 10.31399/asm.hb.v02.a0001079.
- [14] D. Dorow-Gerspach, A. Kirchner, Th. Loewenhoff, G. Pintsuk, T. Weißgärber, and M. Wirtz, “Additive manufacturing of high density pure tungsten by electron beam melting,” *Nuclear Materials and Energy*, vol. 28, p. 101046, Sep. 2021, doi: 10.1016/j.nme.2021.101046.
- [15] D. Wang, C. Yu, X. Zhou, J. Ma, W. Liu, and Z. Shen, “Dense Pure Tungsten Fabricated by Selective Laser Melting,” *Applied Sciences*, vol. 7, no. 4, Art. no. 4, Apr. 2017, doi: 10.3390/app7040430.
- [16] J. P. Hankwitz, C. Ledford, C. Rock, S. O’Dell, and T. J. Horn, “Electron Beam Melting of Niobium Alloys from Blended Powders,” *Materials*, vol. 14, no. 19, Art. no. 19, Jan. 2021, doi: 10.3390/ma14195536.
- [17] C. Zhao *et al.*, “Critical instability at moving keyhole tip generates porosity in laser melting,” *Science*, vol. 370, no. 6520, pp. 1080–1086, Nov. 2020, doi: 10.1126/science.abd1587.
- [18] M. Garibaldi, “Laser additive manufacturing of soft magnetic cores for rotating electrical machinery: materials development and part design,” PhD Thesis, 2018.
- [19] Q. Guo *et al.*, “In-situ characterization and quantification of melt pool variation under constant input energy density in laser powder bed fusion additive manufacturing process,” *Additive Manufacturing*, vol. 28, pp. 600–609, 2019, doi: <https://doi.org/10.1016/j.addma.2019.04.021>.
- [20] S. Lee, J. Peng, D. Shin, and Y. S. Choi, “Data analytics approach for melt-pool geometries in metal additive manufacturing,” *Science and Technology of Advanced Materials*, vol. 20, no. 1, pp. 972–978, 2019, doi: 10.1080/14686996.2019.1671140.
- [21] B. Cheng, L. Loeber, H. Willeck, U. Hartel, and C. Tuffile, “Computational Investigation of Melt Pool Process Dynamics and Pore Formation in Laser Powder Bed Fusion,” *J. of Materi Eng and Perform*, vol. 28, no. 11, pp. 6565–6578, Nov. 2019, doi: 10.1007/s11665-019-04435-y.
- [22] L. Meng *et al.*, “Machine Learning in Additive Manufacturing: A Review,” *JOM*, vol. 72, no. 6, pp. 2363–2377, Jun. 2020, doi: 10.1007/s11837-020-04155-y.
- [23] M. Komorowski, D. C. Marshall, J. D. Saliccioli, and Y. Crutain, “Exploratory Data Analysis,” in *Secondary Analysis of Electronic Health Records*, MIT Critical Data, Ed. Cham: Springer International Publishing, 2016, pp. 185–203. doi: 10.1007/978-3-319-43742-2\_15.
- [24] S. Midway, *Chapter 7 Understanding ANOVA in R | Data Analysis in R*. Accessed: Jul. 19, 2022. [Online]. Available: [https://bookdown.org/steve\\_midway/DAR/understanding-anova-in-r.html](https://bookdown.org/steve_midway/DAR/understanding-anova-in-r.html)
- [25] “Box plot — ggboxplot.” <https://rpkgs.datanovia.com/ggpubr/reference/ggboxplot.html> (accessed Jul. 19, 2022).

- [26] “Dot plot — ggdotplot.” <https://rpkgs.datanovia.com/ggpubr/reference/ggdotplot.html> (accessed Jul. 19, 2022).
- [27] “Correlation matrix : A quick start guide to analyze, format and visualize a correlation matrix using R software - Easy Guides - Wiki - STHDA.” <http://www.sthda.com/english/wiki/correlation-matrix-a-quick-start-guide-to-analyze-format-and-visualize-a-correlation-matrix-using-r-software> (accessed Jul. 19, 2022).
- [28] T. Wei and V. Simko, *An Introduction to corrplot*. 2021. Accessed: Jul. 19, 2022. [Online]. Available: <https://cran.r-project.org/web/packages/corrplot/vignettes/corrplot-intro.html>
- [29] R. W. McVey, R. M. Melnychuk, J. A. Todd, and R. P. Martukanitz, “Absorption of laser irradiation in a porous powder layer,” *Journal of Laser Applications*, vol. 19, no. 4, pp. 214–224, Nov. 2007, doi: 10.2351/1.2756854.
- [30] ANSYS Fluent Theory Guide. 2021.
- [31] M. Bayat, W. Dong, J. Thorborg, A. C. To, and J. H. Hattel, “A review of multi-scale and multi-physics simulations of metal additive manufacturing processes with focus on modeling strategies,” *Additive Manufacturing*, vol. 47, p. 102278, 2021, doi: <https://doi.org/10.1016/j.addma.2021.102278>.
- [32] F. Lia, J. Park, J. Tressler, and R. Martukanitz, “Partitioning of laser energy during directed energy deposition,” *Additive Manufacturing*, vol. 18, pp. 31–39, Dec. 2017, doi: 10.1016/j.addma.2017.08.012.
- [33] L. Cao and X. Yuan, “Study on the Numerical Simulation of the SLM Molten Pool Dynamic Behavior of a Nickel-Based Superalloy on the Workpiece Scale,” *Materials (Basel)*, vol. 12, no. 14, p. E2272, Jul. 2019, doi: 10.3390/ma12142272.
- [34] A. Queva, G. Guillemot, C. Moriconi, C. Metton, and M. Bellet, “Numerical study of the impact of vaporisation on melt pool dynamics in Laser Powder Bed Fusion - Application to IN718 and Ti–6Al–4V,” *Additive Manufacturing*, vol. 35, p. 101249, 2020, doi: <https://doi.org/10.1016/j.addma.2020.101249>.
- [35] A. Temmler, N. Pirch, J. Luo, J. H. Schleifenbaum, and C. L. Häfner, “Numerical and experimental investigation on formation of surface structures in laser remelting for additive-manufactured Inconel 718,” *Surface and Coatings Technology*, vol. 403, p. 126370, Dec. 2020, doi: 10.1016/j.surfcoat.2020.126370.
- [36] T.-N. Le, Y.-L. Lo, and Z.-H. Lin, “Numerical simulation and experimental validation of melting and solidification process in selective laser melting of IN718 alloy,” *Additive Manufacturing*, vol. 36, p. 101519, 2020, doi: <https://doi.org/10.1016/j.addma.2020.101519>.
- [37] K. C. Mills, “Ni - IN 718,” in *Recommended Values of Thermophysical Properties for Selected Commercial Alloys*, K. C. Mills, Ed. Woodhead Publishing, 2002, pp. 181–190. doi: 10.1533/9781845690144.181.
- [38] G. Pottlacher, H. Hosaeus, E. Kaschnitz, and A. Seifert, “Thermophysical properties of solid and liquid Inconel 718 Alloy\*,” *Scandinavian Journal of Metallurgy*, vol. 31, no. 3, pp. 161–168, 2002, doi: 10.1034/j.1600-0692.2002.310301.x.

- [39] A. S. Agazhanov, D. A. Samoshkin, and Y. M. Kozlovskii, “Thermophysical properties of Inconel 718 alloy,” *J. Phys.: Conf. Ser.*, vol. 1382, no. 1, p. 012175, Nov. 2019, doi: 10.1088/1742-6596/1382/1/012175.
- [40] R. N. Abdullaev, R. A. Khairulin, S. V. Stankus, and Yu. M. Kozlovskii, “Density and volumetric expansion of the Inconel 718 alloy in solid and liquid states,” *Thermophys. Aeromech.*, vol. 26, no. 5, pp. 785–788, Sep. 2019, doi: 10.1134/S0869864319050160.
- [41] C. R. Brooks, M. Cash, and A. Garcia, “The heat capacity of inconel 718 from 313 to 1053 K,” *Journal of Nuclear Materials*, vol. 78, no. 2, pp. 419–421, Dec. 1978, doi: 10.1016/0022-3115(78)90463-4.
- [42] M. W. Chase, “NIST-JANAF Thermochemical Tables, Fourth Edition,” *J. Phys. Chem. Ref. Data, Monograph 9*, pp. 1–1951, 1998.
- [43] D. Basak, R. A. Overfelt, and D. Wang, “Measurement of Specific Heat Capacity and Electrical Resistivity of Industrial Alloys Using Pulse Heating Techniques,” *International Journal of Thermophysics*, vol. 24, no. 6, pp. 1721–1733, Nov. 2003, doi: 10.1023/B:IJOT.0000004101.88449.86.
- [44] G. Tanda and M. Misale, “Measurement of Total Hemispherical Emittance and Specific Heat of Aluminum and Inconel 718 by a Calorimetric Technique,” *Journal of Heat Transfer*, vol. 128, no. 3, pp. 302–306, Jun. 2005, doi: 10.1115/1.2150840.
- [45] Y. S. Lee and W. Zhang, “Modeling of heat transfer, fluid flow and solidification microstructure of nickel-base superalloy fabricated by laser powder bed fusion,” *Additive Manufacturing*, vol. 12, pp. 178–188, Oct. 2016, doi: 10.1016/j.addma.2016.05.003.
- [46] R. E. Pawel and R. K. Williams, “Survey of physical property data for several alloys. [Nitronic 33; copper C10400; copper C17510],” Oak Ridge National Lab., TN (USA), ORNL/TM-9616, Aug. 1985. doi: 10.2172/5337885.
- [47] J. J. Valencia and P. N. Quested, “Thermophysical Properties,” Dec. 2008, doi: 10.31399/asm.hb.v15.a0005240.
- [48] K. C. Mills, “Recommended Values of Thermophysical Properties for Selected Commercial Alloys”, [Online]. Available: <https://app.knovel.com/hotlink/toc/id:kpRVTPSCA1/recommended-values-thermophysical/recommended-values-thermophysical>
- [49] M. Hedreen, “Simulation of Additive Manufacturing Process Physics and Properties in Powder Bed Electron-Beam Melting of Ti-6Al-4V,” Thesis, 2020. Accessed: Jul. 11, 2022. [Online]. Available: <https://digital.lib.washington.edu:443/researchworks/handle/1773/45526>
- [50] D. L. McElroy, R. K. Williams, J. P. Moore, R. S. Graves, and F. J. Weaver, “The Physical Properties of Inconel Alloy 718 from 300 to 1000 K,” in *Thermal Conductivity 15*, V. V. Mirkovich, Ed. Boston, MA: Springer US, 1978, pp. 149–151. doi: 10.1007/978-1-4615-9083-5\_18.
- [51] N. Raghavan, “Understanding Process-Structure Relationship For Site-Specific Microstructure Control in Electron Beam Powder Bed Additive Manufacturing Process

- Using Numerical Modeling,” *Doctoral Dissertations*, Dec. 2017, [Online]. Available: [https://trace.tennessee.edu/utk\\_graddiss/4852](https://trace.tennessee.edu/utk_graddiss/4852)
- [52] A. Rai, M. Markl, and C. Körner, “A coupled Cellular Automaton–Lattice Boltzmann model for grain structure simulation during additive manufacturing,” *Computational Materials Science*, vol. 124, pp. 37–48, Nov. 2016, doi: 10.1016/j.commatsci.2016.07.005.
- [53] S. J. Wolff *et al.*, “Experimentally validated predictions of thermal history and microhardness in laser-deposited Inconel 718 on carbon steel,” *Additive Manufacturing*, vol. 27, pp. 540–551, May 2019, doi: 10.1016/j.addma.2019.03.019.
- [54] S. E. Brika, M. Letenneur, C. A. Dion, and V. Brailovski, “Influence of particle morphology and size distribution on the powder flowability and laser powder bed fusion manufacturability of Ti-6Al-4V alloy,” *Additive Manufacturing*, vol. 31, p. 100929, Jan. 2020, doi: 10.1016/j.addma.2019.100929.
- [55] A. M. Rausch, M. Markl, and C. Körner, “Predictive simulation of process windows for powder bed fusion additive manufacturing: Influence of the powder size distribution,” *Computers & Mathematics with Applications*, vol. 78, no. 7, pp. 2351–2359, Oct. 2019, doi: 10.1016/j.camwa.2018.06.029.
- [56] M. A. Spurek, L. Haferkamp, C. Weiss, A. B. Spierings, J. H. Schleifenbaum, and K. Wegener, “Influence of the particle size distribution of monomodal 316L powder on its flowability and processability in powder bed fusion,” *Prog Addit Manuf*, Dec. 2021, doi: 10.1007/s40964-021-00240-z.
- [57] S. Pal *et al.*, “The effects of locations on the build tray on the quality of specimens in powder bed additive manufacturing,” *Int J Adv Manuf Technol*, vol. 112, no. 3, pp. 1159–1170, Jan. 2021, doi: 10.1007/s00170-020-06563-5.
- [58] T.-N. Le, Y.-L. Lo, and Z.-H. Lin, “Numerical simulation and experimental validation of melting and solidification process in selective laser melting of IN718 alloy,” *Additive Manufacturing*, vol. 36, p. 101519, 2020, doi: <https://doi.org/10.1016/j.addma.2020.101519>.
- [59] D. Zhang, P. Zhang, Z. Liu, Z. Feng, C. Wang, and Y. Guo, “Thermofluid field of molten pool and its effects during selective laser melting (SLM) of Inconel 718 alloy,” *Additive Manufacturing*, vol. 21, pp. 567–578, May 2018, doi: 10.1016/j.addma.2018.03.031.
- [60] H. L. Wei, J. Mazumder, and T. DebRoy, “Evolution of solidification texture during additive manufacturing,” *Sci Rep*, vol. 5, no. 1, Art. no. 1, Nov. 2015, doi: 10.1038/srep16446.
- [61] T. Ishikawa and P.-F. Paradis, “Thermophysical properties of molten refractory metals measured by an electrostatic levitator,” *Journal of Elec Materi*, vol. 34, no. 12, pp. 1526–1532, Dec. 2005, doi: 10.1007/s11664-005-0160-z.
- [62] M. W. Chase, “NIST-JANAF Thermochemical Tables, Fourth Edition,” *J. Phys. Chem. Ref. Data, Monograph 9*, pp. 1–1951, 1998.
- [63] K. C. Mills, B. J. Monaghan, and B. J. Keene, “Thermal conductivities of molten metals: Part 1 Pure metals,” *International Materials Reviews*, vol. 41, no. 6, pp. 209–242, Jan. 1996, doi: 10.1179/imr.1996.41.6.209.

- [64] S. V. Onufriev, V. A. Petukhov, V. R. Pesochin, and V. D. Tarasov, "The thermophysical properties of hafnium in the temperature range from 293 to 2000 K," *High Temp*, vol. 46, no. 2, pp. 203–211, Apr. 2008, doi: 10.1134/s10740-008-2008-8.
- [65] Y. Zhang, J. R. G. Evans, and S. Yang, "Corrected Values for Boiling Points and Enthalpies of Vaporization of Elements in Handbooks," *J. Chem. Eng. Data*, vol. 56, no. 2, pp. 328–337, Feb. 2011, doi: 10.1021/je1011086.
- [66] V. N. Korobenko and A. I. Savvatimskii, "Temperature Dependence of the Density and Electrical Resistivity of Liquid Zirconium up to 4100 K," *High Temperature*, vol. 39, no. 4, pp. 525–531, Jul. 2001, doi: 10.1023/A:1017932122529.
- [67] J. W. Arblaster, "The Thermodynamic Properties of Niobium," *J. Phase Equilib. Diffus.*, vol. 38, no. 5, pp. 707–722, Oct. 2017, doi: 10.1007/s11669-017-0557-4.
- [68] P. Akbari *et al.*, "MeltpoolNet: Melt pool Characteristic Prediction in Metal Additive Manufacturing Using Machine Learning." arXiv, Jan. 25, 2022. Accessed: May 17, 2022. [Online]. Available: <http://arxiv.org/abs/2201.11662>
- [69] P. C. Verpoort, P. MacDonald, and G. J. Conduit, "Materials data validation and imputation with an artificial neural network," *Computational Materials Science*, vol. 147, pp. 176–185, May 2018, doi: 10.1016/j.commatsci.2018.02.002.
- [70] S. K. Kauwe, J. Graser, A. Vazquez, and T. D. Sparks, "Machine Learning Prediction of Heat Capacity for Solid Inorganics," *Integrating Materials and Manufacturing Innovation*, vol. 7, no. 2, pp. 43–51, Jun. 2018, doi: 10.1007/s40192-018-0108-9.
- [71] J. J. S. Dilip *et al.*, "Influence of processing parameters on the evolution of melt pool, porosity, and microstructures in Ti-6Al-4V alloy parts fabricated by selective laser melting," *Prog Addit Manuf*, vol. 2, no. 3, pp. 157–167, Sep. 2017, doi: 10.1007/s40964-017-0030-2.
- [72] R. Liang and Y. Luo, "Study on weld pool behaviors and ripple formation in dissimilar welding under pulsed laser," *Optics & Laser Technology*, vol. 93, pp. 1–8, Aug. 2017, doi: 10.1016/j.optlastec.2017.01.029.
- [73] M. Jamshidinia, F. Kong, and R. Kovacevic, "Numerical Modeling of Heat Distribution in the Electron Beam Melting® of Ti-6Al-4V," *Journal of Manufacturing Science and Engineering*, vol. 135, no. 6, Nov. 2013, doi: 10.1115/1.4025746.
- [74] M. J. Torkamany, F. Malek Ghaini, R. Poursalehi, and A. F. H. Kaplan, "Combination of laser keyhole and conduction welding: Dissimilar laser welding of niobium and Ti-6Al-4V," *Optics and Lasers in Engineering*, vol. 79, pp. 9–15, Apr. 2016, doi: 10.1016/j.optlaseng.2015.11.001.
- [75] K. C. Mills, "Ti: Ti-6 Al-4 V (IMI 318)," in *Recommended Values of Thermophysical Properties for Selected Commercial Alloys*, K. C. Mills, Ed. Woodhead Publishing, 2002, pp. 211–217. doi: 10.1533/9781845690144.211.
- [76] M. S. Rahman, P. J. Schilling, P. D. Herrington, and U. K. Chakravarty, "Thermal Analysis of Electron Beam Additive Manufacturing Using Ti-6Al-4V Powder-Bed," presented at the ASME 2017 International Mechanical Engineering Congress and Exposition, Jan. 2018. doi: 10.1115/IMECE2017-71663.

- [77] J. Chen *et al.*, “Laser powder bed fusion of a Nb-based refractory alloy: Microstructure and tensile properties,” *Materials Science and Engineering: A*, vol. 843, p. 143153, May 2022, doi: 10.1016/j.msea.2022.143153.
- [78] Y. Guo, L. Jia, B. Kong, N. Wang, and H. Zhang, “Single track and single layer formation in selective laser melting of niobium solid solution alloy,” *Chinese Journal of Aeronautics*, vol. 31, no. 4, pp. 860–866, Apr. 2018, doi: 10.1016/j.cja.2017.08.019.
- [79] T. Kurzynowski, W. Stopyra, K. Gruber, G. Ziółkowski, B. Kuźnicka, and E. Chlebus, “Effect of Scanning and Support Strategies on Relative Density of SLM-ed H13 Steel in Relation to Specimen Size,” *Materials*, vol. 12, no. 2, Art. no. 2, Jan. 2019, doi: 10.3390/ma12020239.